

Real-Time Biosensing and Energy Harvesting on Human Body

Thesis by
Hyunjun Cho

In Partial Fulfillment of the Requirements for
the degree of
Doctor of Philosophy in Electrical Engineering

The logo for the California Institute of Technology (Caltech), featuring the word "Caltech" in a bold, orange, sans-serif font.

CALIFORNIA INSTITUTE OF TECHNOLOGY
Pasadena, California

2020
Defended June 14th, 2019

© 2019

Hyunjun Cho
ORCID: 0000-0002-8963-5525

ACKNOWLEDGEMENTS

I would first like to thank my advisor, Professor Hyuck Choo. Dr. Choo gave me an opportunity to do science and research. He opened and broadened my research perspectives.

I would also like to express my thanks and appreciation to the committee members, Professor Morteza Gharib, Professor Axel Scherer, and P. P. Vaidyanathan.

I would like to thank Samsung Scholarship. I have had the good fortune to receive Samsung Scholarship from Samsung Display Co., Ltd. for my Ph.D. studies for five years.

I would also like to thank my former and current lab mates, Dr. Jeong Oen Lee, Prof. Daejong Yang, Dr. Radwanul Hasan Siddique, Dr. Shailabh Kumar, Dr. Blaise Ndjamen, Dr. Young-Ji Kim, Haeri Park, and Vinayak Narasimhan. They gave me great inspiration as researchers and as good friends.

Our collaborators gave us great help. Dr. Kevin Ferreri in City of Hope provided advice on insulin sensing works and collected human islet secretion samples. Prof. Christian Rembe and his lab members in TU-Clausthal in Germany helped up for laser Doppler vibrometer (LDV) measurements. Prof. Edgar Sánchez-Sinencio and Dr. Kyoohyun Noh in Texas A&M University, TX helped with energy harvesting circuit design. Dr. Tomohiro Ishikawa in Tohoku University, Japan also helped on building energy harvesting circuits. Prof. Jongho Lee in Gwangju Institute of Science and Technology (GIST), Korea gave me valuable advices on energy harvesting project.

Lastly, I would like to thank my family members. My parents and brother provided unconditional supports and love. My son, Jaeyoon, and my daughter, Jane, have always been the driving force in my life and study. And above all, I want to express my thanks to my other half, Sunyoung. She always motivates me with endless love as a friend, as a supporter, as a teacher, and as a wife.

ABSTRACT

This thesis covers two technologies that can be applied to the human body for real-time applicable usages: biosensors and energy harvesters. The first part of the thesis describes optical biosensing techniques based on surface-enhanced Raman spectroscopy (SERS). Our large-scale spatially uniform Raman enhancing substrates allow low-level bio molecule detection due to their strong plasmonic enhancement of the 3D Au-NP clusters. This method also enables low-level insulin sensing as well as insulin concentration analysis in islet secretion. These results can lead to developing simple and easy biosensing methods allowing real-time biosensing applications including convenient monitoring of health, early disease detection, and diabetes-related clinical measurements.

The second part of the thesis suggests an energy harvesting method using vocal vibrations. The vocal folds produce mechanical vibrations that can serve as an energy source with consistent amplitude and frequency. The vibration hotspots exist at various locations on the human upper body. The energy harvesting system consisting of piezoelectric devices and energy harvesting circuits generates 3.99 mW of electrical power. The amount of energy generated from vocal vibrations is sufficient to charge a Li-Po battery which can drive an LCD display or charge Bluetooth headphones. This method demonstrating a relatively high power generation and convenience of practical use can provide a real-time complementary charging technique for wearable electronics like wireless headphones and smart glasses as well as medical implantable devices such as deep brain stimulators, cochlear implants and pacemakers.

PUBLISHED CONTENT AND CONTRIBUTIONS

Hyunjun Cho, Ashwin Balakrishna, Yuan Ma, Jeong Oen Lee, Hyuck Choo (2016). “Efficient power generation from vocal folds vibrations for medical electronic implants.” In: *2016 IEEE 29th International Conference on Micro Electro Mechanical Systems (MEMS)*, pp. 363–366. DOI: 10.1109/MEMSYS.2016.7421636, URL: <https://ieeexplore.ieee.org/document/7421636>.

H.C. participated in the conception of the project, carried out experiments, prepared the data, and participated in the writing of the manuscript.

Daejong Yang, Jeong Oen Lee, Hyunjun Cho, Sukmo Koo, Sagar R. Vaidyanathan, Kelly Woo, Hyuck Choo (2016). “3 Dimensionally Stacked Surface Enhanced Raman Scattering (SERS) Substrates with pico-Molar Sensitivity: Experimental and Simulation Studies.” In: *2016 Progress in Electromagnetic Research Symposium (PIERS)*, pp. 3936. DOI: 10.1109/PIERS.2016.7735481, URL: <https://ieeexplore.ieee.org/abstract/document/7735481>.

H.C. participated in the conception of the project, prepared the data, and participated in the writing of the manuscript.

Kelly Woo, Daejong Yang, Hyunjun Cho, Hyuck Choo (2016). “ZnO-nanowire morphology optimization for glucose-SERS sensing.” In: *2016 Progress in Electromagnetic Research Symposium (PIERS)*, pp. 3943. DOI: 10.1109/PIERS.2016.7735484, URL: <https://ieeexplore.ieee.org/abstract/document/7735484>.

H.C. participated in the conception of the project, prepared the data, and participated in the writing of the manuscript.

Hyunjun Cho, Kyoo Hyun Noh, Tomohiro Ishikawa, Daejong Yang, Edgar Sánchez-Sinencio, Hyuck Choo (2017). “Powering portable electronics using vocal fold vibrations.” In: *2017 IEEE 30th International Conference on Micro Electro Mechanical Systems (MEMS)*, pp. 217-220. DOI: 10.1109/MEMSYS.2017.7863379, URL: <https://ieeexplore.ieee.org/abstract/document/7863379>.

H.C. participated in the conception of the project, solved structures, carried out experiments, prepared the data, and participated in the writing of the manuscript.

Hyuck Choo, Hyunjun Cho (2017). “Systems, devices, and methods for electric power generation from vocal folds vibrations.” In: *US Patent Application*, Pub No.: US 2017/0084815A1.

H.C. participated in the conception of the project, analyzed the crystal structures, and prepared the data.

Daejong Yang, Hyunjun Cho, Sukmo Koo, Sagar R Vaidyanathan, Kelly Woo, Youngzoon Yoon, Hyuck Choo (2017). “Simple, large-scale fabrication of uniform Raman-enhancing substrate with enhancement saturation.” In: *ACS applied materials & interfaces*, vol. 9, no. 22, pp. 19092-19101. DOI: 10.1021/acsami.7b03239, URL: <https://pubs.acs.org/doi/abs/10.1021/acsami.7b03239>.

H.C. participated in the conception of the project, solved and analyzed the structures, prepared the data, and participated in the writing of the manuscript.

Robert Kowarsch, Jürgen Janzen, Christian Rembe, Hyunjun Cho, Hyuck Choo (2017). “Scanning confocal vibrometer microscope for vibration analysis of energy-harvesting MEMS in wearables.” In: *tm-Technisches Messen*, vol. 84, no. s1, pp. 131-137. DOI: 10.1515/teme-2017-0042, URL: <https://www.degruyter.com/view/j/teme.2017.84.issue-s1/teme-2017-0042/teme-2017-0042.xml>.

H.C. participated in the conception of the project, carried out experiments, prepared the data, and participated in the writing of the manuscript.

Hyunjun Cho, Shailabh Kumar, Daejong Yang, Sagar Vaidyanathan, Kelly Woo, Ian Garcia, Hao J Shue, Youngzoon Yoon, Kevin Ferreri, Hyuck Choo (2018). “Surface-enhanced Raman spectroscopy-based label-free insulin detection at physiological concentrations for analysis of islet performance.” In: *ACS Sensors*, vol. 3, no. 1, pp. 65-71. DOI: 10.1021/acssensors.7b00864, URL: <https://pubs.acs.org/doi/abs/10.1021/acssensors.7b00864>.

H.C. participated in the conception of the project, carried out experiments, prepared the data, and participated in the writing of the manuscript.

Daejong Yang, Sajjad Afroosheh, Jeong Oen Lee, Hyunjun Cho, Shailabh Kumar, Radwanul H Siddique, Vinayak Narasimhan, Young-Zoon Yoon, Alexey T Zayak, Hyuck Choo (2018). “Glucose sensing using surface-enhanced Raman-mode constraining.” In: *Analytical Chemistry*, vol. 90, no. 24, pp. 14269-14278. DOI: 10.1021/acs.analchem.8b03420, URL: <https://pubs.acs.org/doi/abs/10.1021/acs.analchem.8b03420>.

H.C. participated in the conception of the project, prepared the data, and participated in the writing of the manuscript.

Daejong Yang, Hyunjun Cho, Youngzoon Yoon, Hyuck Choo (2018). “Substrate for sensing, a method of fabricating the substrate, and analyzing apparatus including the substrate.” In: *US Patent Application*, Pub No.: US 2018/0340830A1.

H.C. participated in the conception of the project, analyzed structures, prepared the data, and carried out experiments.

TABLE OF CONTENTS

Acknowledgements	iii
Abstract	iv
Published Content and Contributions.....	v
Table of Contents.....	vii
List of Illustrations.....	ix
List of Tables	xvii
Chapter I: Thesis Overview.....	1
1.1 Introduction	3
1.2 Surface-Enhanced Raman Spectroscopy-Based Label-Free Biosensor	3
1.3 Powering Wearable / Implantable Devices Using Vocal Vibrations.....	5
Part I: Surface-Enhanced Raman Spectroscopy-Based Label-Free Biosensors	
Chapter II: Spatially Uniform Raman-Enhancing Substrate with Enhancement Saturation	12
2.1 Biosensing Technology for Hormone Detection.....	13
2.2 Surface-Enhanced Raman Spectroscopy-Based Biosensing	20
2.3 Fabrication of Raman Enhancing Substrates.....	21
2.4 Characterization of Raman Enhancing Substrates	21
2.5 Quantitative Bio Molecule Measurements Using 3D-Stacked Gold-Nanoparticle Substrates	21
2.6 Conclusions	24
Chapter III: Surface-Enhanced Raman Spectroscopy-Based Label-Free Insulin Detection.....	29
3.1 Label-Free Insulin Sensing Technology.....	30
3.2 SERS-Based Quantitative Measurements for Low-Level Insulin Detection.....	35
3.3 Accurate Insulin-Level Detection of Human Pancreatic Islet Secretion	40
3.4 Conclusions	57
Part II: Vocal Vibrations-Driven Energy Harvesters	
Chapter IV: Characterization of Vocal Vibrations as Power Sources	40
4.1 Energy Harvesting for Wearable Electronics and Biomedical Implants	41
4.2 Basic Characterization of Vocal Vibrations	43
4.3 Vibration Hotspots Mapping Around Human Upper Body.....	50
4.4 Conclusions	57
Chapter V: Power Generation Using Vocal Vibrations	40
5.1 Piezoelectric Energy Harvester and Energy Harvesting Array.....	41

5.2 Energy Harvesting Circuit and System.....	43
5.3 Power Generation Results Using Vocal Vibrations	50
5.4 Conclusions	50
Chapter VI: Practical Energy Harvesting from Human Vocal Folds.....	40
6.1 Energy Harvesting for Broadband Applications	41
6.2 Characterization of Broadband Applicable Piezoelectric Beams	43
6.3 Energy Harvesting from Top of the Human Head	50
6.4 Conclusions	50

LIST OF ILLUSTRATIONS

<i>Number</i>	<i>Page</i>
1.1 Various applications of fast, easy, and quantitative insulin sensing techniques including inexpensive lab research, real-time monitoring with implants or wearable devices, and islet cell transplantation. Photos of Diabetes Daily, LifeMed Media, and Johns Hopkins Medicine.	2
1.2 Vocal vibrations for harvesting energy for wearable electronics and biomedical implants. Vibration hotspots around the human upper body are noted (red area).....	4
2.1 A schematic of the sequential fabrication process for (a) Au NP film coated devices and (b) 3D stacked Au NP clusters supported by ZnO nanowire devices.....	11
2.2 Schematic of sequential hydrothermal synthesis for ZnO nanowires and liquid phase deposition (LPD) for Au nanoparticles.	11
2.3 SEM and EDS data of Au NP film substrates. (a) SEM images of the top view of Au NP film coated devices by Au synthesis repetitions. (b) EDS data of Au NP substrate from each Au NP LPD repetition.....	14
2.4 SEM and EDS data of 3D Au NP cluster substrates. (a) SEM images of the top view of Au NP clusters which were grown by repeating the Au synthesis process, supported by ZnO nanowire devices. (b) EDS data of 3D Au NP substrate from each Au NP LPD repetition.....	15
2.5 Atomic % changes in Au, Si, and Zn based on EDS data from (a) 2D Au NP substrates and (b) 3D Au NP substrates as a function of Au NP LPD repetition.	16
2.6 SEM images of cross-sectional view of (a) 2D Au NP substrate, (b) ZnO nanowire synthesized substrate, and (c) 3D Au NP substrate after Au NP LDP process.....	16
2.7 SEM images of top views of (a) 2D Au NP structure and (b) 3D Au NP structure.	17
2.8 Raman spectra measurement setup (Renishaw's inVia). 785 nm IR laser is used for irradiation on the device.	19

2.9	SERS spectra of 1 mM BT solution of (a) 2D Au NP substrate and (b) 3D Au NP substrate. Raman peaks at wavenumber of 999, 1022, 1072 and 1574 cm^{-1} detected by (c) 2D Au NP substrate and (d) 3D Au NP substrate. All measurements were done with various repetition of synthesis.....	19
2.10	SERS measurements of benzenethiol solutions. (a) SERS spectra of 1 mM, 1 μM , 1 nM, and 1 pM benzenethiol solution. (b) SERS peaks at 999, 1022, 1072, and 1574 cm^{-1} with various concentrations of benzenethiol solution.....	22
2.11	Spatial uniformity of Au NP substrates. (a) 2D Raman mapping and (b) statistical distribution of Raman intensity measured at 1072 cm^{-1} on a $10 \times 10 \mu\text{m}^2$ 2D NP-8 substrate incubated in 1-mM benzenethiol solution; (c) 2D Raman mapping and (d) statistical distribution of Raman intensity measured on a 3D NP-8 substrate with same condition. (e) Photo of 3D-stacked Au NP synthesized on 4-inch wafer; (f) 2D mapping and (g) statistical distribution of 1 mM benzenethiol incubated 3D stacked Au NP synthesized on 4-inch wafer.	23
2.12	SERS spectra measurements by various incident angles of light. (a) Measurement set-up; (b) SEM images of tilted devices with 0 to 80 degrees; (c) SERS spectra of 1mM benzenethiol incubated 3D stacked Au NP substrate with various incidence angles and (d) relationship between SERS intensity and incidence angle.....	24
2.13	Quantitative SERS measurements using 3D Au NP substrates with adenine solutions. (a) Reference SERS spectra of 10 μM , 1 μM , 100 nM, and 10nM adenine solution using 3D Au NP-8 substrate; (b) the experimentally measured relationship between concentration of adenine solution and SERS intensity; (c) concentration readouts for adenine solutions using 3D Au NP-8 substrate.....	26
3.1	Raman peaks corresponding to the amino acids of insulin. (a) Amino acid composition of insulin (Hilderink et al., 2013). (b) Measured Raman spectra from human insulin and bovine insulin.....	34
3.2	$5 \times 5 \text{ mm}^2$ SERS chip incubated inside the PDMS chamber with 200 μL of insulin solution.	36
3.3	SEM images of 3D Au NP substrate coated with insulin. (a) Cross-sectional SEM image showing the vertical pillar-like 3D	

	arrangement of the Au-NP clusters on the ZnO synthesized substrate. SEM images (top view) of a substrate (b) before and (c) after insulin incubation.....	36
3.4	Raman spectra of (a) human insulin powder and (b) SERS substrate incubated in 1 mM insulin solution.	37
3.5	Quantitative measurements of insulin solutions. (a) SERS spectra of 100 pM, 500 pM, 1 nM, 5 nM, 10 nM, 50 nM human insulin solutions highlighting the target peak at 1002 cm ⁻¹ . (b) Experimentally measured relationship between the insulin concentration and SERS intensity; the inset shows a linear relationship between the Raman intensity and concentration from 100 pM to 10 nM.	39
3.6	Evaluation of insulin coated SERS substrates. (a) 2D Raman-intensity mapping of a SERS chip after incubating in a 10 nM insulin solution. The RSD of the Raman signal over the 1×1 mm ² area was found to be 4.3%, demonstrating excellent spatial uniformity. (b) Histogram showing the narrow distribution of Raman intensity over the mapped region. (c) Graph showing the mean and standard deviation of Raman signals collected from the sample as a function of the scan size used for areal averaging. (d) A SERS spectrum captured from a 3D Au-NP SERS chip coated with a drop of 100-pM human insulin solution followed by rapid on-chip evaporation.....	40
3.7	Representational SERS spectra obtained from (a) Low glucose buffer (b) High glucose buffer (c) Islet secretions in low glucose buffer with ELISA measured insulin concentration of approximately 138 pM. (d) Islet secretions in high glucose buffer with ELISA measured insulin concentration of approximately 513 pM.....	45
3.8	Label-free sensor to assess the functionality of human islet secretion. (a) Illustration of using a 3D Au-NP SERS chip for analysis of pancreatic islet secretions. Secretions from islets were obtained under low and high glucose conditions. (b) SERS signal intensities measured on various islet secretions (the vertical axis) correlated with the concentrations of insulin in the samples obtained using the ELISA method (the horizontal axis).	46
4.1	Examples of publicly released wearable electronic devices. (a) Apple Watch. Courtesy of Apple Inc. (b) Google Glasses.	

Courtesy of Google Inc. These devices still have batteries inside the packages (insets).....	54
4.2 Various kinds of biomedical implants which require electricity including neurostimulators, cardiovascular implants, ophthalmic implants, orthopedic implants, and dental implants.....	54
4.3 Vocal vibrations to harvest energy into wearable devices and biomedical implants.....	56
4.4 Structure of the larynx. (Anatomy of the Larynx, Elena Rizzo Riera, 2008, Trialsight Medical Media). (a) Interior view and (b) exterior view of the larynx.....	56
4.5 Characterization of vocal fold vibrations. (a) Average frequency range of vocal fold vibrations from male and female participants when they make /a/ sounds and /m/ sounds. (b) Amplitudes measured from accelerometers as the target male and female participants changed their vibrations frequencies.....	58
4.6 Transient output of the acceleration from the accelerometer during humming (a) and reading (b). Normalized frequency responses of the accelerations (along z-axis to the skin) obtained above during humming (c) and reading (d).	60
4.7 Three-axis measurement results using MEMS accelerometers placed on the human larynx while a man was humming (a) and reading (b), and a woman was humming (c) and reading (d). The vibrations along the z-axis is obviously dominant one among three-axis measurement results.	61
4.8 Building a 3D human head model for finite element simulation. 3D rendered image from CT scanned images with mouth closed (a) and open (b). Segmented and smoothed 3D head model with mouth closed (c) and open (d).....	63
4.9 Colormaps of stress at frequencies of 100, 200 and 300 Hz on the head model with mouth open (above) and mouth closed (below).	66
4.10 Pictures of the vibration hotspots identification around the head. Accelerometer measurements (a) and laser Doppler vibrometer (LDV) measurement (b).	67
4.11 Colormap of the vibration hotspots around the head and neck using accelerometers (a) and LDV measurements (b).....	67
5.1 Schematic of piezoelectric cantilever beam. The beam length (L) and thickness (T) determine the resonance frequency of the beam	75

5.2	Mode shapes of cantilever beam when $n = 1, 2 \dots 6$ in a_n .	77
5.3	Expected resonance frequency and generated power of the beam using simulation method. (a) Resonance frequencies obtained from simulations with varying both lengths and thicknesses of the beam. The white line indicates the 260 Hz of resonance frequency. (b) Generated voltage and resonance frequency expectations as the beam length increases, when the thickness and the beam width were fixed. When the beam length is 28 mm and the resonance frequency is 260 Hz, 1.0 V will be generated.	78
5.4	Fabricated energy harvesting cantilever beam (a) and its frequency analysis (b). Both simulation result and measurement data are shown in (b).	79
5.5	Structure of the energy harvesting package. (a) 3D-printed package for unit energy harvesting device. (b) Clamping packaging structure containing 10 energy harvesters. The 10-energy harvesting array consists of 10 energy harvesters packaged in a unit structure, then the whole structure is rigidly clamped in the 3D-printed clamping structure and screws. (c) Assembled 10-stacked energy harvesting array fixed on the larynx. The bottom surface of the clamping structure has a curvature, so that it can fit to the outer diameter of the neck	81
5.6	Synchronization effect found in the clamping package structure. (a) Metronome experiment. (b) Cantilevers in the clamping package first move out of phase, and eventually couple in phase	82
5.7	Transient signals from four energy harvesters. When the humming started, the phase difference and amplitude difference were large (Phase b-1), but the waves started to synchronize together after 50 milliseconds (Phase b-2), then eventually settled in near complete synchronization (Phase b-3)	83
5.8	Energy harvesting circuit in the energy harvesting system. (a) Energy harvesting system diagram. (b) Schematic of the energy harvesting system including the 4-stacked energy harvesting array and the LC resonant double rectifier. (c) LTSpice schematic of the piezoelectric device and the LC resonant voltage double rectifier	85
5.9	Comparison of the simply stacked package and the clamped package using 2- and 4- stacked arrays. (a) Photo images of the simply stacked package and clamped package using 4 devices.	

- (b) Transient measurements using each package without AC/DC conversion. The simply stacked one shows larger phase and amplitude differences. (c) DC output voltage measurements using AC/DC converter. The clamped packaged devices generated about twice more output voltage than voltage that the simply stacked package generated 86
- 5.10 DC voltage measurement using clamping packaged EH array and LC resonant rectifier. (a) Load optimization for 10-stacked EH array. (b) DC output voltage measurements and simulation results using different number of stacked piezoelectric devices 88
- 5.11 Charging a Li-Po battery using the energy harvesting array. (a) DC voltage generation using a vibration generator with 10-stacked EH array to charge a Li-Po battery for a long time. (b) Charging voltage to charge 3.7 V-100 mAh LiPo battery for six hours 89
- 5.12 Full wave rectifier as AC/DC converter in the energy harvesting system. (a) Schematic of the full wave rectifier as AC/DC converter which consists of two active diodes, two passive diodes, and a switched inductor; the left image is the corresponding circuit board. (b) Detailed schematic including the elements of full wave rectifier, connections between the elements, and the connectors 91
- 5.13 Power generation using the fabricated full wave rectifier. (a) Layout design of the printed circuit board (PCB) and the fabricated PCB where the proposed full wave rectifier with a switched inductor was implemented. (b) Load test with active full wave rectifier and passive full wave rectifier. The black line and blue line with triangle symbols are voltage and power measurements from with the active full wave rectifier, and the other black line and blue line with triangle symbols are voltage and power measurements using the passive full wave rectifier. The maximum attained power was found to be at 4 k Ω load. (c) An array of 10 energy harvesting units generated 3.99 mW with a 4 k Ω load 93
- 5.14 15-mAh Li-Ion battery charging using a 10-stacked energy harvesting array. (a) The first three seconds of battery charging using vocal the vibrations and vibration generator. (b) Cumulative charging with the vibration generator. The voltage at the battery reached 3.76 V after 12 hours of charging. (c & d)

The battery charged for 10 minutes with vocal vibrations was sufficient to operate the 10-LED array and the 2×16 LCD backlight unit	94
5.15 Wearable energy harvesting device demonstration. (a) Vibration distribution measured by accelerometers in the upper body including the chest area. (b) Wearable energy harvesting from the jaw area. (c) Wearable energy harvesting package using the chest area. (d) Bow-tie shaped energy harvesting package using the neck area	96
5.16 Bow tie shaped energy harvester using a 4-energy harvesting array. The battery and circuits were placed inside the shirt collar to charge the Bluetooth headphones	97
5.17 Summary of the literature survey on biomechanical energy harvesting devices in terms of output power vs frequency. The results are divided in two colors: blue requiring negligible physical movements and green requiring intensive physical movements. Results acquired in this work are marked and compared with previous literatures	99
6.1 Determining the parameters of the serpentine and spiral beams. (a) Basic configuration of serpentine beam and spiral beam used for the energy harvesting structure. (b) Calculated spiral length by changing initial radius and number of turns of the spiral at a given outer dimension (12×12 mm ²).	105
6.2 Frequency response of serpentine beam from simulation. This beam has 6 bents and the beam width is 1.5 mm.....	106
6.3 Calculated resonance frequencies at 1st to 6th mode with (a) the initial radius changed (number of turns fixed) and (b) different numbers of turns (initial radius fixed).....	107
6.4 Laser cutting process to pattern the serpentine and spiral beams. (a) laser cutting setup including laser head, stage, and suction tool. Laser cutting edge of the piezoelectric material using (a) CO ₂ laser and (b) ultra-short pulse laser	108
6.5 Fabricated serpentine beam and spiral beams. Spiral beams were made in five different shapes by varying the inner radius and the number of turns	109
6.6 Laser Doppler vibrometer setup for modal analysis of piezoelectric beams. (a) Schematic of the of scanning confocal vibrometer microscope. (b) Photo of the whole measurement setup	110

6.7	Modal analyses of the serpentine beam using simulation and LDV measurements	110
6.8	Modal analyses of the spiral beam using simulation and LDV measurement	111
6.9	Frequency analyses of spiral beams by changing initial radius (a) and number of turns (b). The resonance frequencies at 1st - 3rd modal orders are summarized in (c) and (d).....	112
6.10	Frequency analysis of serpentine beam.....	114
6.11	Optimum load test by measuring output power with each load from spiral beam (a) and serpentine beam (b)	114
6.12	Time- and frequency-domain transient output signal from spiral beam ($n = 6$, $a = 1.5$ mm) while humming and reading	115
6.13	DC output voltages from 4-stacked spiral beams and serpentine beams when the participant read a book. The voltage double rectifier was used to convert AC to DC signal	115
6.14	Human head model for measurement of artificial vocal vibrations. (a) The human head model includes vocal folds and airways to allow air flow throughout the head. (b) Frequency modulated air flow was produced using the fast switching solenoid valve and the controller board	117
6.15	Vibration mapping from real human head (a), scalp of the head model (b), and skull of the head model (c)	118
6.16	Titanium (Ti) casing to firmly stack two spiral beams. (a) Photo images of the stacked spiral beams and Ti casing. (b) Frequency analyses of the top and bottom device before and after packaging	119
6.17	Power generation at the top of the head using the two-stacked spiral beams. (a) Synchronization of two-stacked energy harvesters. Transient signals when humming starts (b) and 50 msec after humming starts (c). (d) AC transient output signal from 2-stacked energy harvesting package using spiral beams. (e) AC transient output signal after LC resonant full wave rectifier	120
6.18	Concept image of energy harvesting package to be implanted on the skull of human head.....	121

LIST OF TABLES

<i>Number</i>	<i>Page</i>
4.1 The material properties used in the head model simulation.	66
4.2 Power requirements to operate various biomedical electronic implants.	70
5.1 Solutions for α_n in Equation 5.2.	77
5.2 Power generation using wearable energy harvesting devices	98
6.1 The 1st, 2nd and 3rd mode shapes of the rectangular, serpentine, and spiral beams.	107
6.2 Mode shapes (modal order is 1 to 8) of spiral beams with a different initial radius of spiral when number of turns is fixed at 5 turns.	108
6.3 Area of vibration hotspot (> 75%, > 50% of the center point) at the location of top of the head.	119

Chapter 1

THESIS OVERVIEW

1.1. Introduction

Smart wearable electronics such as smart watches and smart glasses have been commercially released and received huge public attention. Also, implantable healthcare devices including deep brain stimulation, cochlear implants, and pacemakers have been used to relieve pains or disorders for patients. Recently, more wearable electronics and implantable devices are being introduced to the public. This thesis deals with two kinds of technologies related to the actions of human body: surface-enhanced Raman spectroscopy (SERS)-based biosensing and vocal vibrations-based energy harvesting. These two techniques can lead to real-time biomonitoring system and complementary energy source for wearables or implants.

SERS-based biosensors use Raman-enhancing substrates consisting of 3D stacked gold-nanoparticles. The label-free biomolecule sensing method demonstrates quantitative measurements as a function of concentration of benzenethiol, adenine, and insulin.

Vocal vibrations-driven energy harvesters utilize vocal vibrations produced from vocal folds in the larynx. This method can provide reliable energy sources for wearable electronics or medical electronic implants on the human upper body.

1.2. Surface-Enhanced Raman Spectroscopy-Based Label-Free Biosensors

The growing prevalence of diabetes in the global population has made detection of insulin *in vitro* and *in vivo* an extremely important problem in diabetes therapy and research. A label-free sensing platform that could provide a fast, easy, and quantitative way to quantify insulin can be applied to treat diabetic patients, prevent life-threatening hypoglycemic episodes, save unnecessary lab expenses, and accelerate diabetes research and drug discovery (Figure 1.1).

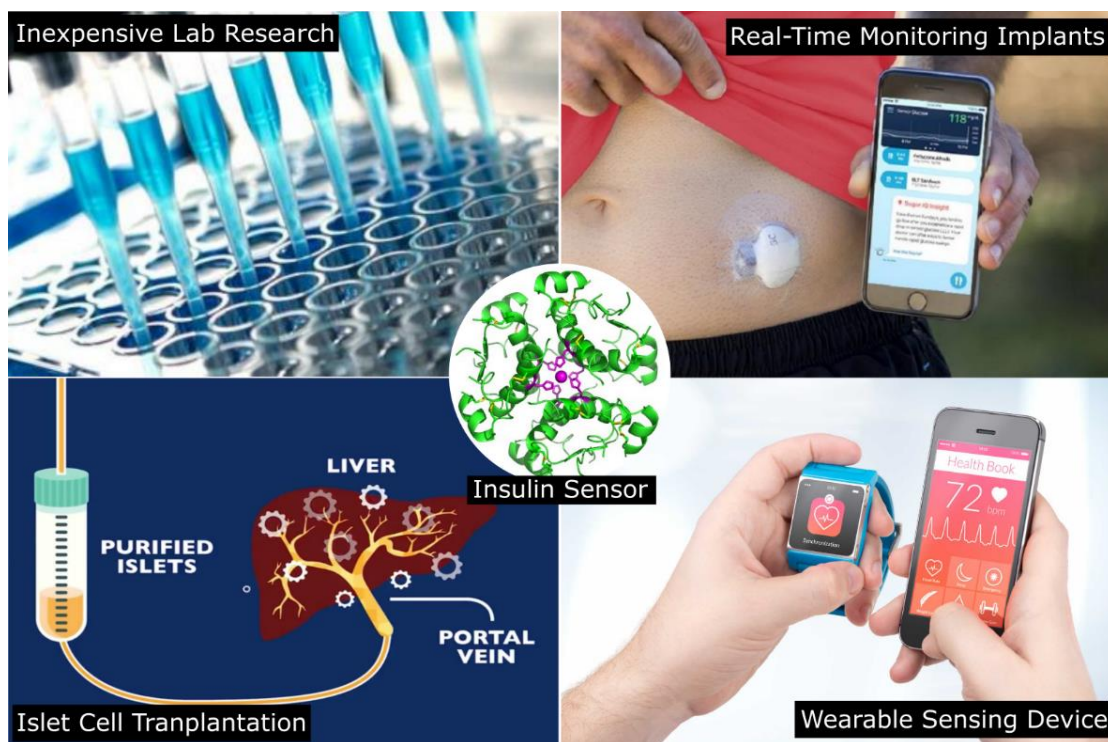


Figure 1.1: Various applications of fast, easy, and quantitative insulin sensing techniques including inexpensive lab research, real-time monitoring with implants or wearable devices, and islet cell transplantation. Photos of Diabetes Daily, LifeMed Media, and Johns Hopkins Medicine.

Spatially Uniform Raman-Enhancing Substrate with Enhancement Saturation

As a potential way to address this need, we have utilized a gold nanoparticle (Au-NP)-coated zinc oxide (ZnO) nanowire substrate and quantified insulin directly adsorbed to the surface using surface-enhanced Raman spectroscopy (SERS).

In Chapter 2, the fabrication process to make Raman-enhancing substrates with 3D-stacked Au-NP is described. The structure of this substrate is analyzed to explain how the Raman-enhancing substrate works, then we applied this substrate to SERS measurements of benzenethiol (BT). For quantitative measurements of biomolecule, adenine with various concentrations (10 nM to 10 μ M) was used to obtain the relationship between concentration and Raman intensity.

Surface-Enhanced Raman Spectroscopy-Based Label-Free Insulin Detection

Low-level insulin sensing and quantitative analyses of various concentrations of human insulin are shown in Chapter 3. Due to strong binding interaction between disulfide bonds in insulin molecule and the gold atoms on the substrate, strong plasmonic enhancement is achieved.

Raman intensity from various concentration levels of insulin was measured, then linear relationship between Raman intensity and concentration of insulin was found. We also carried out Raman measurements using human pancreatic islet secretion and the Raman intensity at 1002 cm^{-2} was identifiable. The linear fit obtained from insulin levels based on SERS measurements of islet secretions shows the same slope as one from insulin quantitative measurements.

1.3. Vocal Vibrations-Driven Energy Harvesters

A variety of wearable electronics have been commercially released and different kinds of biomedical implants have been applied to treat certain diseases (insets of Figure 1.2). However, they typically require battery packs that need to be charged or replaced periodically. If there is a reliable energy source in the human body, it could broaden the flexibility in designs of wearable electronics and solve reliability issues regarding batteries in biomedical implants.

We suggest vocal vibrations from human vocal folds as energy source to harvest energy for wearable or implantable devices around the human upper body. We characterize the vocal vibrations to generate consistent power, then demonstrate energy harvesting devices using vocal vibrations (Figure 1.2).

Characterization of Vocal Vibrations as Power Sources

In order to verify the vocal vibrations as promising energy sources, frequency analyses and vibration hotspots mapping are carried out through both simulation methods and experimental measurements (Chapter 4).

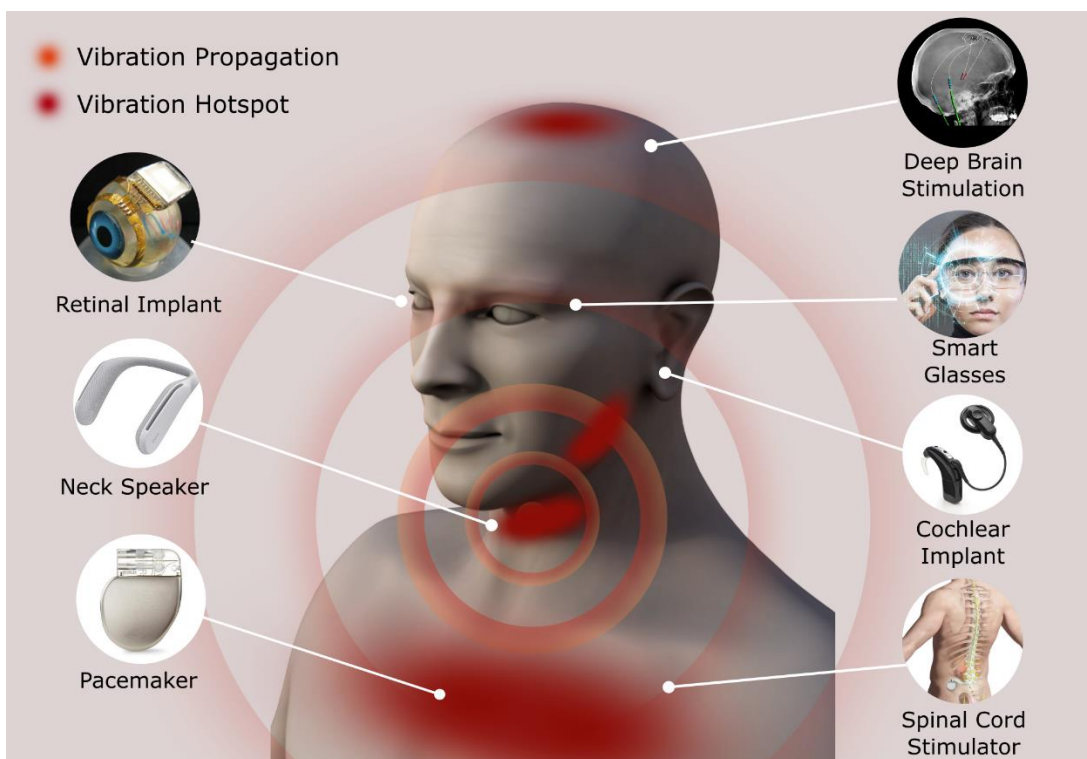


Figure 1.2: Vocal vibrations for harvesting energy for wearable electronics and biomedical implants. Vibration hotspots around the human upper body are noted (red area).

Power Generation Using Vocal Vibrations

Energy harvesting systems to collect electrical energy from vocal vibrations is described in Chapter 5. To utilize vocal vibrations efficiently, we developed an energy harvesting system consisting of piezoelectric energy harvesting devices, energy harvesting circuits, and battery. 3.99 mW of electrical power can be achieved at the larynx using a 10-stacked energy harvesting array and LC resonant full-wave rectifier. Also, energy harvesting at various locations around the upper body were demonstrated.

Practical Energy Harvesting from Human Vocal Folds

For real-time energy harvesting for practical applications, the energy harvesting method needs to generate enough power using common phonation such as speaking or reading. The amplitudes are spread over a broadband according to the frequency responses from reading, which requires broadband applicable energy harvesting devices. Newly designed structures

such as serpentine beams and spiral beams are verified for efficient energy harvesting while reading a book.

The top of the head is a vibration hotspot which is a relatively large area adjacent to the brain. Both areas on the scalp and on the skull can be applicable as vibration sources based on the acceleration measurements on the realistic human head model. These approaches to practical use of vocal vibrations as energy sources are discussed in Chapter 6.

Part I

Surface-Enhanced Raman Spectroscopy- Based Label-Free Biosensors

*Chapter 2*SPATIALLY UNIFORM RAMAN-ENHANCING SUBSTRATE WITH
ENHANCEMENT SATURATION

In this chapter, we describe the general concept of surface-enhanced Raman spectroscopy (SERS) and various structures for SERS that have been studied. Also, we investigate vertically perforated three-dimensional (3D) Au-nanoparticle stacks for surface-enhanced Raman spectroscopy (SERS). The 3D stacked Au structure is demonstrated through two straightforward fabrication processes: hydrothermal synthesis of ZnO nanowires standing perpendicular to silicon wafers, and conformal liquid-phase deposition of Au nanoparticles optimally repeated on tops and sides of the nanowires. During nanoparticle deposition, nanowires gradually dissolve away, leaving only their hollow vestiges or perforations. The experimental measurements reveal that these nanoscale perforations serve as “plasmonic-gap optimizers” that strongly enhance particle-to-particle interactions and as “light-breathing holes” that allow the excitation light to reach deeper into the 3D stacks. This saturates the Raman enhancement everywhere at 1-pM sensitivity and substantially improves the wafer-scale uniformity by 100%, when compared with nanoparticle layers deposited without using nanowires. Understanding and implementing the enhancing mechanisms of our approach will lead to significantly enhanced, practical SERS substrates with excellent spatial uniformity for quantitative chemical sensing.

Part of the work that appears in this chapter was published and is included here with the permission of the publisher as shown below.

"Reprinted (adapted) with permission from Daejong Yang, Hyunjun Cho, Sukmo Koo, Sagar R. Vaidyanathan, Kelly Woo, Youngzoon Yoon, and Hyuck Choo, *ACS Applied Materials & Interfaces* **2017** 9 (22), 19092-19101. DOI: 10.1021/acsami.7b03239. Copyright 2017 American Chemical Society."

2.1. Sensing Technology for Biomedical Application of Hormone Detection

Hormones are chemical messengers that control a wide variety of functions in the human body. Maintaining adequate hormone levels is extremely important for human health and disruption to these levels can result in life-debilitating conditions such as diabetes. Simple and easy measurements of hormonal secretions *ex vivo* or *in vivo* are essential for implementing next generation biosensors, allowing convenient monitoring of health and early disease detection.

Various sensing methods have been previously explored for hormone detection including radioimmunoassays (Andersen et al., 1993), mass-spectrometry (Zhang et al., 2012), photoluminescence (Cha et al., 2011), electrochemical methods (Xu et al., 2013), electrophoresis-dependent immunoassays (Roper et al., 2003; Guillo and Roper, 2008), surface plasmon-resonance (SPR)-based competitive binding assays (Gobi et al., 2007), and fluorescence resonance energy transfer (FRET) (Want et al., 2014). The optical detection techniques such as SPR, photoluminescence, and FRET suffer from poor sensitivity and cannot detect insulin at physiologically observed picomolar concentrations (Cha et al., 2011; Gobi et al., 2007, Wang et al., 2014). Electrochemical impedance spectroscopy and immunoassays have reported more sensitive insulin-specific detection, however these methods have primarily relied on labels such as antibodies for detection (Andersen et al., 1993; Xu et al., 2013; Luo et al., 2013). These labels are not only expensive, but have also been shown to disrupt the natural behavior of live cells and are potentially toxic, making them incompatible with live cells (Schnell, 2012; Blasi et al., 2016).

For applications such as hormone sensing during pancreatic islet transplantation, the islet cells must remain as close to their natural state as possible during the pre-surgical screening process, therefore a label-free sensing method capable of performing ultrasensitive, molecule-specific detection of insulin is desired. Surface-enhanced Raman spectroscopy (SERS) is an ideal approach for optical label-free sensing because it identifies targeted

molecules based on their unique vibrational and rotational signatures (Fleischmann et al., 1974; Albrecht et al., 1977; Nie et al., 1997; Kneipp et al., 1997; Bantz et al., 2011).

2.2. Surface-Enhanced Raman Spectroscopy

Surface-enhanced Raman spectroscopy (SERS) has a great potential for chemical and biological sensing due to its high sensitivity and selectivity obtained with relatively simple optical measurements (Nie et al., 1997). Because of these advantages, SERS has been widely researched since M. Fleischmann, et al. (1974) first observed the SERS effect, and researchers have continuously attempted to develop commercial products (White et al., 2014).

The mechanisms of SERS enhancement are still a subject under study, yet they are predicted to originate from electromagnetic enhancement generated by noble substrate metals and chemical effects between analytes and noble metal atoms (Campion et al., 1998; Kambhampati et al., 1998; Alonso-Gonzalez et al., 2012; Schlucker et al., 2014). The electromagnetic effect is believed to be dominant enhancement mechanism for SERS, and it is generated when the surface plasmons of noble metals are excited under laser irradiation (Alonso-Gonzalez et al., 2012; Tong et al., 2011). These excited plasmons greatly enhance the Raman scattering. Chemical enhancement, on the other hand, is attributed to electrochemical interactions between analyte molecules and the substrate-metal atoms (Kambhampati et al., 1998; Sun et al., 2008; Zayak et al., 2011).

In order to make SERS more useful for practical applications, it is essential to develop better understanding of the enhancing mechanisms of the SERS structures and simpler substrate-fabrication process for commercialization. SERS structures had typically been 2 dimensional (2D) structures made by either patterning metal films or coating the substrate with metal nanoparticles (NPs) (Braun et al., 2007; Fang et al., 2008). And, recently, more elaborate 3-dimensional (3D) structures have been actively researched (Wang et al., 2014; Chirumamilla et al., 2014). 3D substrates have advantages over traditional 2D substrates: larger effective hot-spot surface area and more adsorption of target molecules, both of which can dramatically enhance Raman signals (Tang et al., 2012; Liu et al., 2014; Dai et

al., 2014; Bai et al., 2015; Fu et al., 2014; Zhou et al., 2014). To make high performance 3D SERS substrates, researchers have not only utilized various shapes of 3D nanostructures such as stacked nanoparticles, pyramid and vertically grown nanowires, but also applied well known 2D-techniques to control surface roughness and sizes of metal nanostructures (Zhang et al., 2007; Fraire et al., 2013). For commercial applications, patterned metal films or metal-NP-coated substrates are typically utilized.

More recently, novel nanowire-based 3D substrates are becoming popular because of the development of simpler fabrication methods (Zhao et al., 2009; He et al., 2014). Various types of one-dimensional (1D) nanomaterials such as ZnO (Tang et al., 2012; Liu et al., 2014), TiO₂ (Dai et al., 2014), Si (Bai et al., 2015), Cu₂O (Fu et al., 2014), and NiO (Zhou et al., 2014) have been demonstrated as base structures for SERS substrates that lead to allow flexibility regarding to nanoscale sizes and shapes of the 3D SERS substrates. Among these nanomaterials, ZnO can be synthesized using a simple and low-cost method such as vapor-solid growth or hydrothermal synthesis. Additionally, the shape and size of the nanowires can be adjusted to some degree (Jang et al., 2009; Willander et al., 2009; Guo et al., 2005; Li et al., 2009).

2.3. Fabrication of Raman Enhancing Substrates

Evaporation and sputtering are common techniques that are used to coat noble metals on the surface of nanostructures (Tang et al., 2012; Liu et al., 2014). However, these direct deposition methods have limitations, because it is difficult to control the final shape and the roughness of the metal. In addition, if these directional deposition methods are used, it is difficult to uniformly coat vertically standing nanostructures with the metal from the top to the bottom.

There is another factor as important as SERS intensity which is spatial uniformity for practical applications. Even though fabrication of uniform substrate is essential for quantitative measurement, most of SERS researches have focused on high sensitivity. It is very hard to realize high sensitivity and high uniformity simultaneously due to difficulty in controlling position and shape of small nanostructures on the entire substrate. Some

researchers have fabricated uniform SERS substrates, however they could not overcome non-uniformity and inaccurate position of each nanostructures (Zhang et al., 2014; Tang et al., 2013; Pazos-Perez et al., 2010).

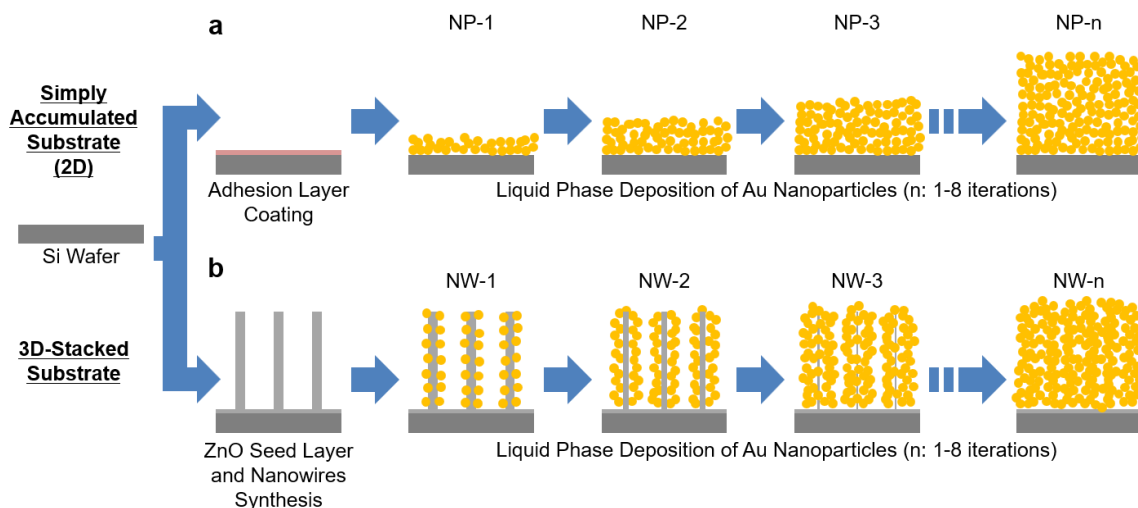


Figure 2.1: A schematic of the sequential fabrication process for (a) Au NP film coated devices and (b) 3D stacked Au NP clusters supported by ZnO nanowire devices.

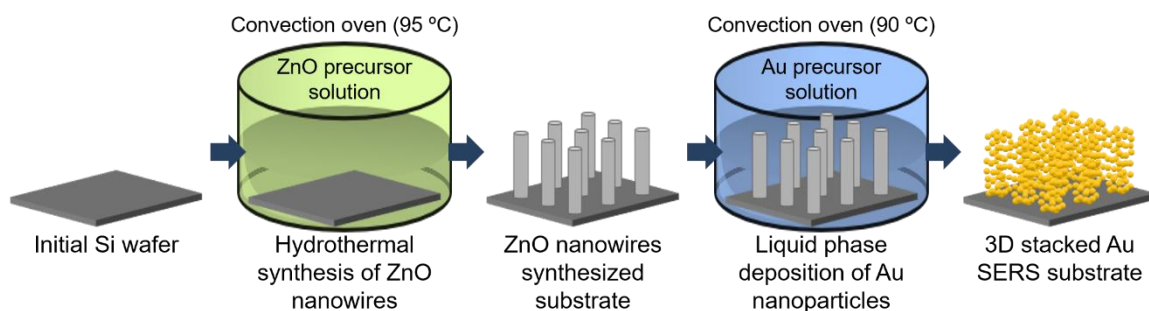


Figure 2.2: Schematic of sequential hydrothermal synthesis for ZnO nanowires and liquid phase deposition (LPD) for Au nanoparticles.

We fabricated SERS substrates which are ready to use for practical application. This means that we considered not only high sensitivity and high uniformity, but also an economical and simple fabrication process. The fabrication method consists of two successive wet

chemical reactions which are hydrothermal synthesis of ZnO nanowires (Law et al., 2005) and liquid phase deposition (LPD) of Au NPs (Acosta et al., 2012). These methods were conducted in mild temperature and atmospheric pressure thus they do not require expansive setup. ZnO nanowires were perpendicularly synthesized and acted as framework for Au NP deposition. Au NPs were efficiently stacked during the LPD process and the nanowires were gradually dissolved away, leaving only their hollow vestiges. The well controlled Au NPs and ZnO vestiges led to high sensitivity, and the effectively stacked Au NPs contributed to high spatial uniformity.

The fabrication process of both 2D Au NP film and 3D Au NP cluster structures are shown in Figure 2.1. For 2D Au NP structure, Au NP-coated Si substrates were fabricated using the LPD method. A bare Si substrate was immersed in 3-aminopropyltriethoxysilane (APTES, $\text{H}_2\text{N}(\text{CH}_2)_3\text{Si}(\text{OC}_2\text{H}_5)_3$, Sigma Aldrich, $\geq 99\%$) for 15 minutes to ensure the adhesion of the synthesized Au NPs to the Si substrate. APTES functionalized the Si surface with amine groups so that they are chemically bonded to citrates groups in the Au-NP precursor solution (Castillo et al., 2011). This helps the gold NPs to remain adhered to the silicon surface. The substrate was then placed in the Au NP precursor solution for 1 hour at 90°C in a convection oven (Jeio Tech's OF-01E-120). The precursor solution was prepared from 1 mM sodium tetrachloroaurate (III) dihydrate ($\text{NaAuCl}_4 \cdot 2\text{H}_2\text{O}$, Sigma Aldrich, $\geq 99\%$) and 200 μM sodium citrate dihydrate ($\text{HOC}(\text{COONa})(\text{CH}_2\text{COONa})_2 \cdot 2\text{H}_2\text{O}$, Sigma Aldrich, $\geq 99\%$) in DI water. Then, 0.1 M sodium hydroxide (NaOH, Sigma Aldrich, $\geq 98\%$) aqueous solution was added until the resulting pH of the solution was 9. This LPD process is repeated between 1 and 8 times for a thick Au NP film (NP-1, NP-2, ..., and NP-8). The higher the number of repetitions, the thicker the Au NP film. The substrates are washed with DI water and ethanol ($\text{CH}_3\text{CH}_2\text{OH}$, Sigma Aldrich, 200 proof) so that excess salt and carbon compounds are washed away (Figure 2.1a).

During the Au-NP synthesis process, Cl^- ions are displaced from NaAuCl_4 by hydrolysis, and replaced by the OH^- ions. The sodium citrate then initiates the reduction of Au anions (Moreau et al., 2005; Lim et al., 2011; Haruta, 2004). Moreover, citrate anions prevent the

coagulation of Au anions, which can maintain the diameter of Au NPs around 10 to 20 nm. Figure 2.3a shows an SEM image of the top view of the Au NP film coated devices. Au NPs with 10 to 20 nm diameter were intermittently synthesized during the first LPD process. As we increased the number of repetitions for the Au NP synthesis process, the number of particles also increased, and additionally, the particles also tended to agglomerate. Even through NPs agglomerated, the diameter of single NPs stayed between 10 and 20 nm. The height of the NP film is approximately 0.5-1 μm , but some regions are still not covered with gold NPs. The EDS data of the devices in Figure 2.3b agree with what we observe in the SEM images. The percentage of Au atoms increased with the increasing number of synthesis repetitions, and the percentage of Si atoms appeared lower because Au NPs covered Si substrates and blocked the Si signal out (Figure 2.5a).

To fabricate 3D Au NP clusters, nanowires were used as basic framework. The sequential fabrication process including hydrothermal synthesis for ZnO nanowires and liquid phase deposition (LPD) for Au nanoparticles is described in Figure 2.2. ZnO nanowires were synthesized using the hydrothermal method because it was a simple way to synthesize nano-sized vertical structures. ZnO seed solution consisting of 5 mM zinc acetate dihydrate ($\text{Zn}(\text{CH}_3\text{COO})_2 \cdot 2\text{H}_2\text{O}$, Sigma Aldrich, $\geq 98\%$) in ethanol was coated onto a bare Si substrate, and then annealed on a hot plate at 350 $^\circ\text{C}$ for 20 minutes to ensure the adhesion of the seed to the silicon (Greene et al., 2005). The substrate was then placed inside the ZnO precursor solution, which consists of 25 mM zinc nitrate hexahydrate ($\text{Zn}(\text{NO}_3)_2 \cdot 6\text{H}_2\text{O}$, Sigma Aldrich, 98%), 25 mM HMTA (hexamethylenetetramine, $\text{C}_6\text{H}_{12}\text{N}_4$, Sigma Aldrich, $\geq 99\%$) and 5 mM PEI (polyethyleneimine, $(\text{C}_2\text{H}_5\text{N})_n$, Sigma Aldrich, average Mw ~ 800) in DI water for 2.5 hours at 95 $^\circ\text{C}$ in a convection oven. The substrate was then taken out of the solution and rinsed with DI water, and annealed on a hot plate at 350 $^\circ\text{C}$ for 20 minutes. In order to synthesize the Au NP on the ZnO nanowires, the silicon substrates with the ZnO nanowires were placed into the Au NP precursor solution. The solution was heated for 1 hour at 90 $^\circ\text{C}$ and the process was repeated between 1 and 8 times to create a dense Au NP film (NW-1, NW-2, ... and NW-8). Then the substrates were washed with DI water and ethanol.

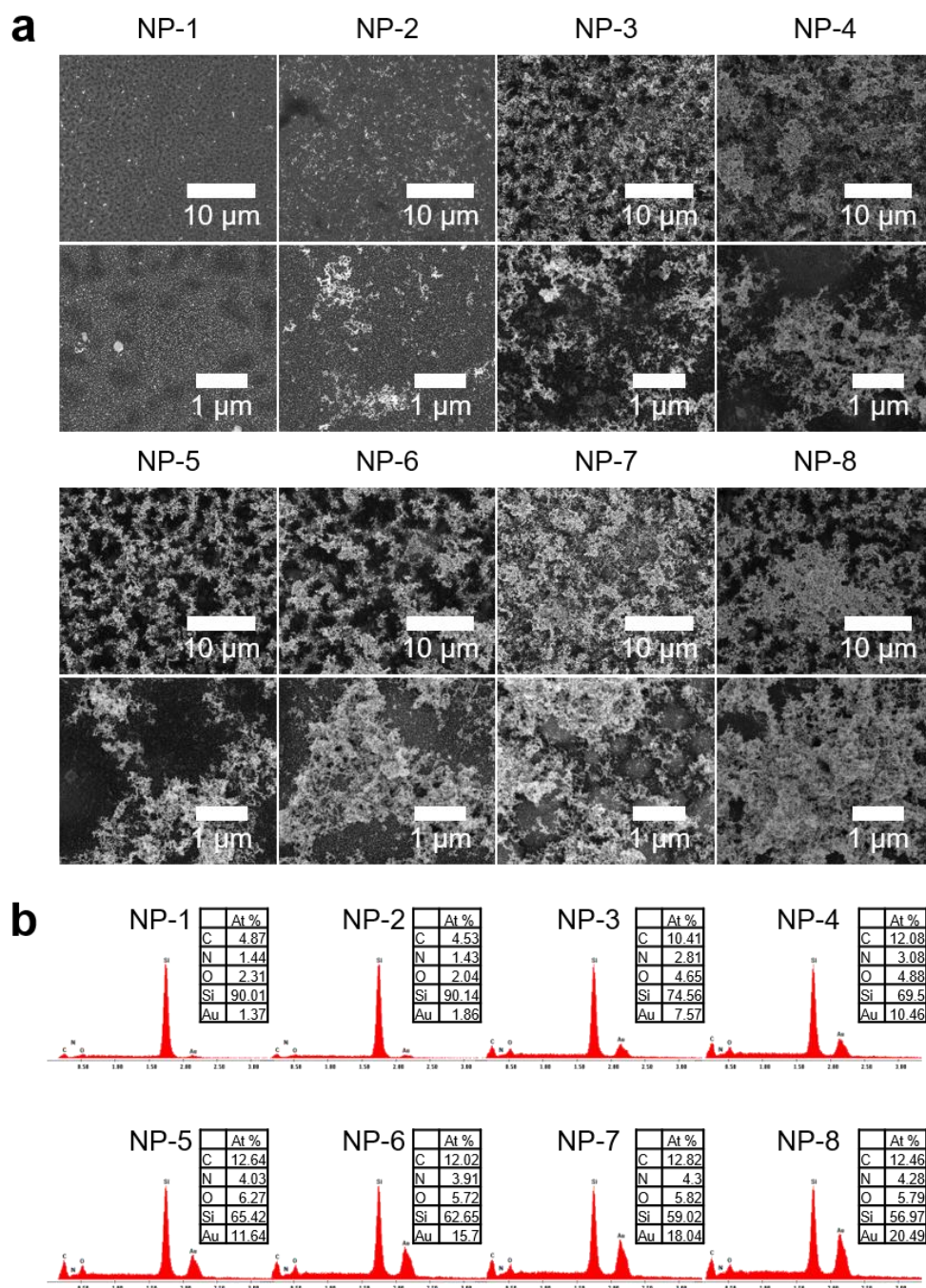


Figure 2.3: SEM and EDS data of Au NP film substrates. (a) SEM images of the top view of Au NP film coated devices by Au synthesis repetitions. (b) EDS data of Au NP substrate from each Au NP LPD repetition.

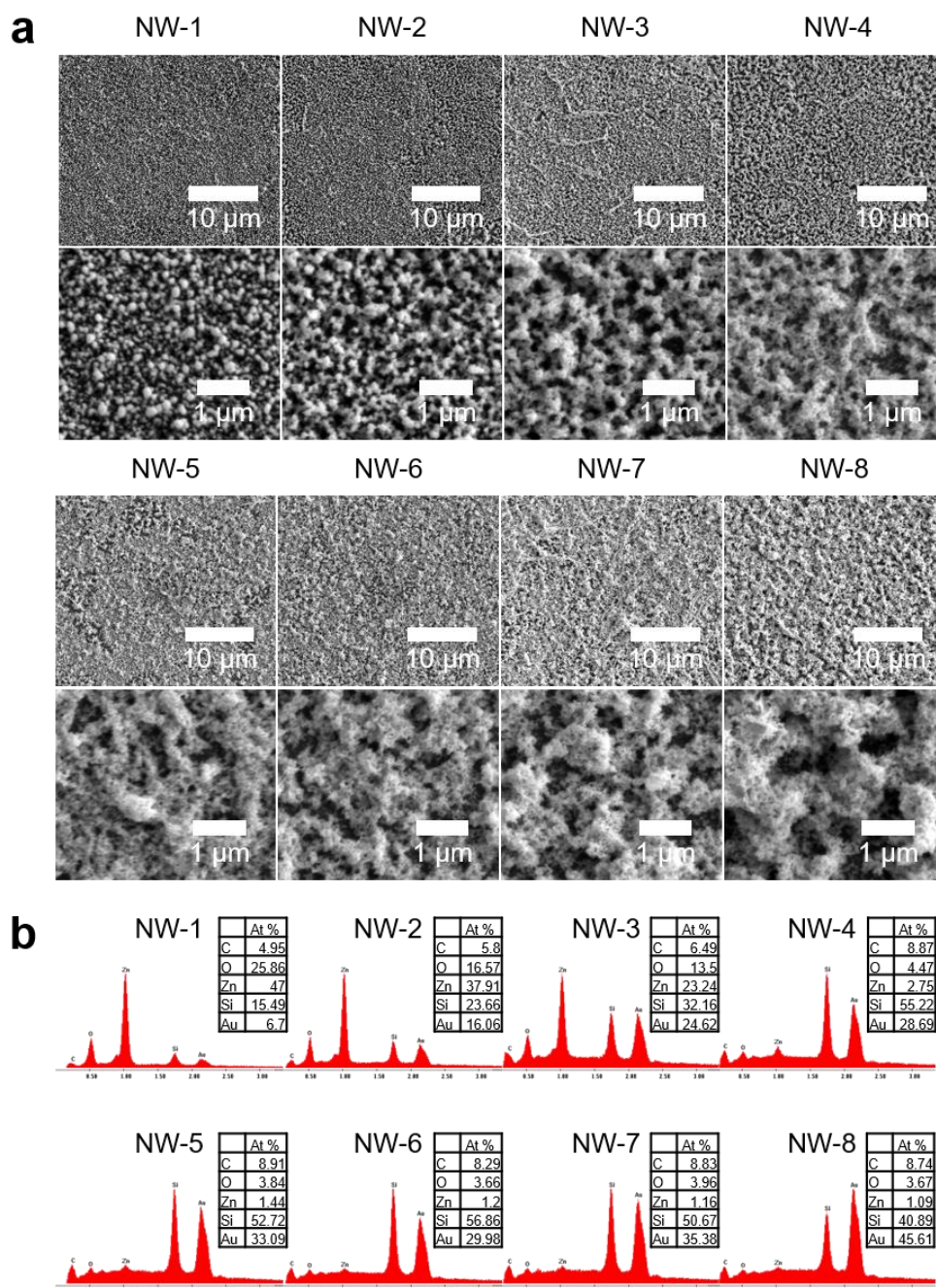


Figure 2.4: SEM and EDS data of 3D Au NP cluster substrates. (a) SEM images of the top view of Au NP clusters which were grown by repeating the Au synthesis process, supported by ZnO nanowire devices. (b) EDS data of 3D Au NP substrate from each Au NP LPD repetition.

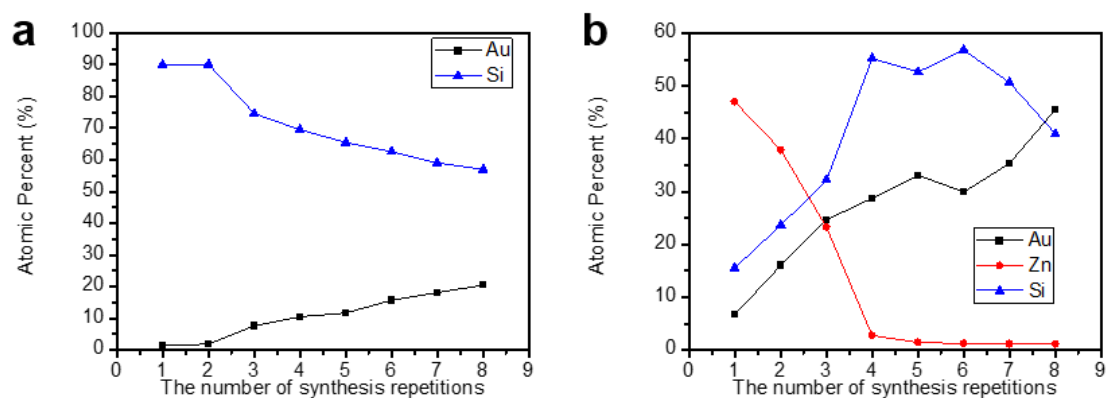


Figure 2.5: Atomic % changes in Au, Si, and Zn based on EDS data from (a) 2D Au NP substrates and (b) 3D Au NP substrates as a function of Au NP LPD repetition.

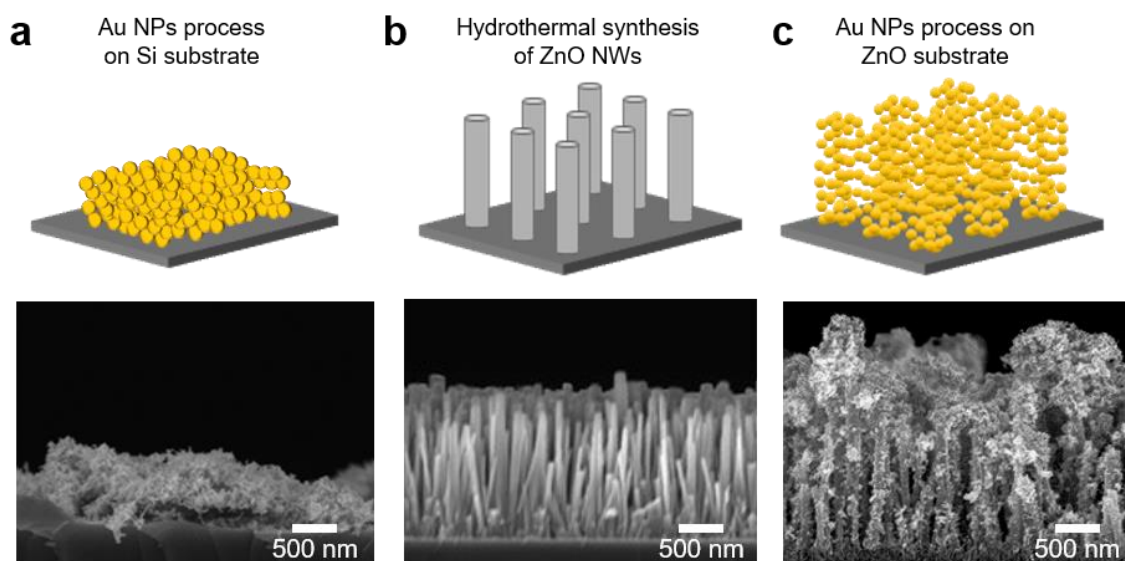


Figure 2.6: SEM images of cross-sectional view of (a) 2D Au NP substrate, (b) ZnO nanowire synthesized substrate, and (c) 3D Au NP substrate after Au NP LDP process.

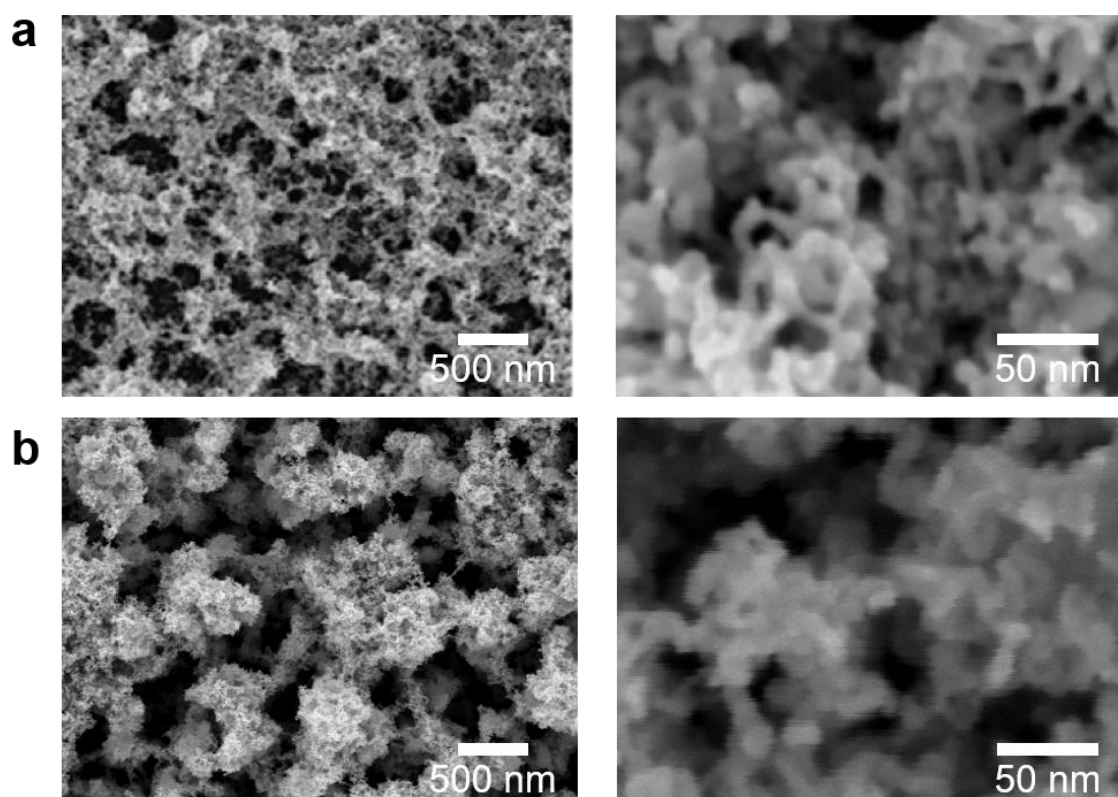


Figure 2.7: SEM images of top views of (a) 2D Au NP structure and (b) 3D Au NP structure.

As shown in the SEM images of cross-sectional view of ZnO nanowires in Figure 2.6b, the diameter and height of ZnO nanowires were approximately 50 nm and 1 μm , respectively. After the synthesis of ZnO nanowires, Au NPs were coated on the ZnO nanowires. Au NPs were synthesized using the same method that was used to fabricate the 2D Au NP film devices. Due to strong adsorption between metal oxide and citrate anions, Au NPs securely adhered to the surface of ZnO nanowires without the help of ATPES. Figure 2.4a shows an SEM image of top view of the Au NP coated ZnO nanowire devices. For devices that had 1 or 2 synthesis iterations (NW-1 and NW-2), the shape of the ZnO nanowires were observed and Au NPs were coated on the surface of ZnO nanowires. Because the synthesis reaction occurred in the liquid, the Au NPs were conformally coated on the top surface as well as the side walls of the nanowires. As the number of synthesis repetitions increased, we observed that the ZnO nanowires started to dissolve away and Au-NP clusters started

to increase in size. In order to avoid the etching of ZnO nanowires, we initially adjusted the initial pH level of the Au NP precursor solution to 9, which is near the isoelectric point of ZnO (Zang et al., 2007), yet the pH level dropped to around 5.5 after the synthesis process, and the ZnO nanowires had gradually been etched during the synthesis iterations. This result is supported by the EDS data in Figure 2.4b and Figure 2.5b. The proportion of Zn atoms to the Au atoms decreased as the number of repetitions increased. The proportion of Si atoms relatively increased from 1 to 4 repetitions of Au NP synthesis due to the erosion of the ZnO nanowires. However, the proportion of Si atoms started to decrease after the sixth synthesis process because Au NPs more densely covered the Si substrates. As shown in the high-resolution SEM images of the cross-sectional view (Figure 2.6c) and the top view (Figure 2.7b) of the NW-8 sample, the diameter of single NP was 10 to 20 nm, which was similar to the size of the Au NPs on the 2D Au NP film devices (Figure 2.7a). Even if the ZnO nanowires in NW-8 sample completely etched away, the height of Au NP films were thicker films in the NP-8 sample because the ZnO nanowires served as a skeletal frame for vertical deposition.

2.4. Characterization of Raman Enhancing Substrates

We verified the role of ZnO nanowires and Au NPs by the experimental method. To evaluate the SERS performance of the devices, SERS spectra of 1 mM benzenethiol (BT, C_6H_5SH , Sigma Aldrich, $\geq 98\%$) solution was measured. All substrates (eight Au NP-coated Si substrates and eight Au NP-coated on ZnO nanowire on Si substrates) were incubated in a 1 mM BT in ethanol solution for 5 hours. The samples are then taken out of the BT solution, and rinsed with ethanol and blow-dried using nitrogen gas. Measurements were taken using a Raman microscope (Renishaw's inVia, United Kingdom) with 20 \times magnitude objective lens with 1.25- μm spot size and 0.07 mW of 785 nm infrared (IR) laser for 100 s (Figure 2.8).

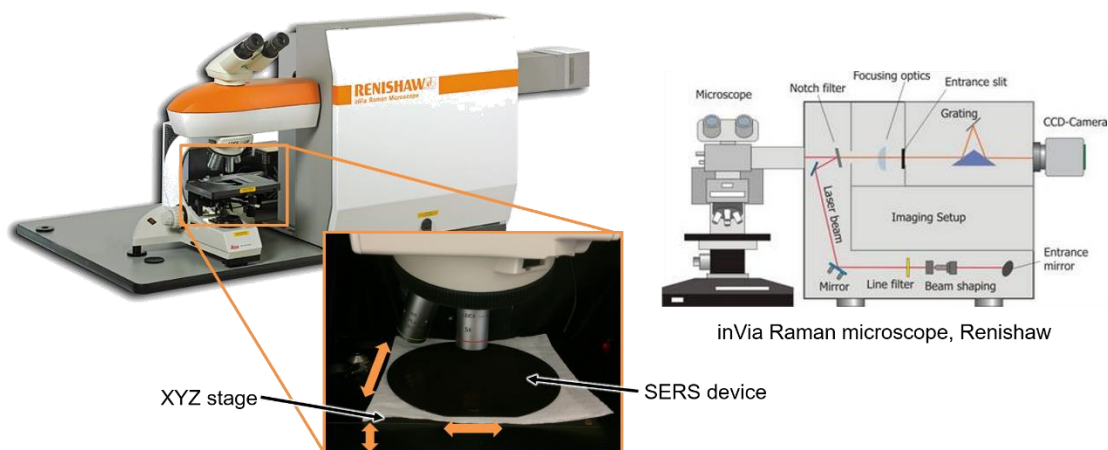


Figure 2.8: Raman spectra measurement setup (Renishaw's inVia). 785 nm IR laser is used for irradiation on the device.

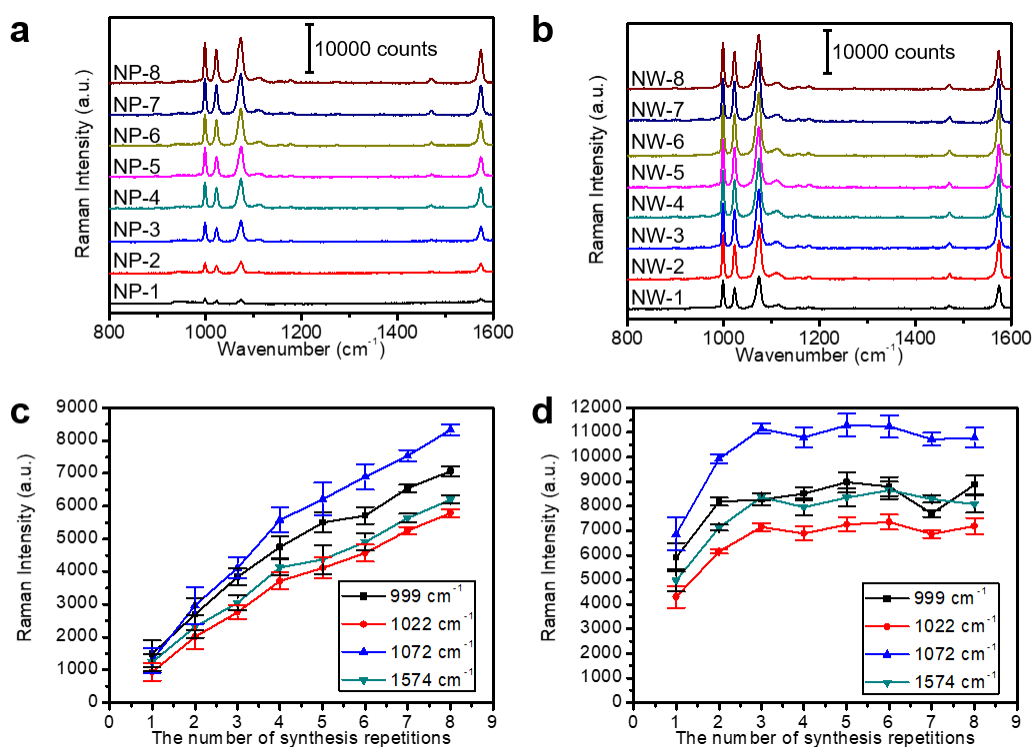


Figure 2.9: SERS spectra of 1 mM BT solution of (a) 2D Au NP substrate and (b) 3D Au NP substrate. Raman peaks at wavenumbers 999, 1022, 1072 and 1574 cm^{-1} detected by (c) 2D Au NP substrate and (d) 3D Au NP substrate. All measurements were done with various repetitions of the synthesis.

As shown in Figure 2.9a, the clear Raman peaks were observed at wavenumbers 999 (in-plane ring-breathing mode), 1022 (in-plane C-H bending mode), 1072 (C-S stretching mode) and 1574 cm^{-1} (C-C stretching mode) (Joo et al., 1987). The Raman intensities increased as the number of synthesis repetitions increased (Figure 2.9c) due to increase in the NPs' surface area and density as well as the geometrical interplay between NPs that increases electromagnetic enhancement. According to our study, SERS intensity continued to increase theoretically and experimentally up to the 8-synthesis iteration.

Even though these Au NP film devices showed good SERS results, the enhancement level was not sufficient for accurate measurements of low concentration analytes. Moreover, eight or more repetitions of the Au NP synthesis process can be time-consuming and inefficient. It is well-known that nanoscale roughness strongly enhances the SERS signal due to a highly intensified electric field (Zhang et al., 2007). In addition, the surface roughness also increases the Raman signal due to large reaction areas between Au NPs and analyte molecules (Hong and Li, 2013).

Figure 2.9b shows the SERS spectra of the Au NP-coated ZnO nanowire devices with a 1 mM BT solution. Four clear peaks at the wavenumbers 999, 1022, 1072 and 1574 cm^{-1} were also detected, and one can observe the systematic increase in Raman intensity with the number of Au NP synthesis repetitions. The Raman intensity of a flat-film device coated with Au NPs once (NW-1) shows a similar signal as a Si sample without nanowires coated 6 times with 2D Au NPs (NP-6). Due to the efficient vertical stacking of the Au-NPs that results in the larger surface area and more particle-to-particle interactions, the Raman intensities continuously increased as the number of the NP-synthesis iterations increased. Additionally, the enhancement was saturated after five iterations as shown in Figure 2.9d.

The enhancement factor (EF) of the device was calculated using the following relation:

$$EF = \frac{I_{SERS}}{I_{bulk}} \times \frac{N_{bulk}}{N_{ads}} \quad (2.1)$$

where I_{SERS} is the intensity of the SERS spectrum of benzenethiol (BT) obtained from Au NP cluster and I_{Bulk} is the intensity the Raman spectrum of BT solution measured in the cuvette. The intensities at 1072 cm^{-1} were used to calculate the EF value. N_{bulk} is the molecule number of the BT in the laser focal volume. The laser focal volume can be determined by the focal area and focal depth of the laser spot and is calculated to be $1314\text{ }\mu\text{m}^3$. Thus, the N_{bulk} of 1 mM BT solution in the focal spot is calculated to be 7.91×10^8 . N_{ads} is the number of molecules adsorbed on the SERS substrate within the laser spot, defined as the following expression:

$$N_{ads} = N_d \cdot A_{spot} \cdot \alpha \quad (2.2)$$

where N_d is the packing density of BT ($6.8 \times 10^{14}\text{ cm}^{-2}$), A_{spot} is the area of the focal spot of the laser ($1.23\text{ }\mu\text{m}^2$), and α is the ratio between the surface of nanoparticle cluster and a flat surface of the same horizontal dimensions. The nanoparticle cluster height is approx. $1\text{ }\mu\text{m}$ and the diameter of the AuNPs are about 20 nm , so 50 layers of nanoparticles are theoretically stacked. Considering the spherical shape of nanoparticles, the connection area between nanoparticles, laser penetration depth and the porosity of the nanoparticle cluster, α is calculated. Therefore, N_{ads} is calculated to be about 5.56×10^6 . The intensity of the electric field was exponentially decreased as laser light traveling toward the bottom layer and this screening effect was considered for EF calculation. The EF values of the overall 3D Au NP substrate can be estimated to be 8.73×10^8 . The substrate is a composition of connected nanoparticles and properly separated nanoparticles. The high electromagnetic enhancement generates gaps between nanoparticles. The EF values at the gaps were calculated to be 9.31×10^9 .

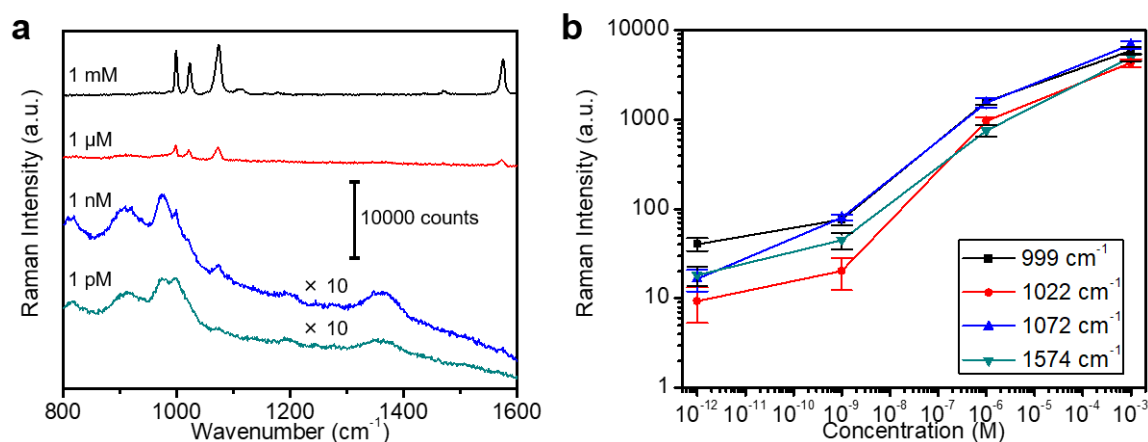


Figure 2.10: SERS measurements of benzenethiol solutions. (A) SERS spectra of 1 mM, 1 μM , 1 nM, and 1 pM benzenethiol solution. (B) SERS peaks at 999, 1022, 1072, and 1574 cm^{-1} with various concentrations of benzenethiol solution.

To evaluate the sensitivity of the Au NP coated device with quantitative measurements, 3D stacked substrates coated with 5 repetitions of Au NPs were incubated in 1 μM , 1 nM and 1 pM BT solutions for 5 hours. As shown in Figure 2.10a, four clear SERS peaks were observed from 1 μM , 1 nM, 1 pM, and 1 mM of BT solution. Intensities of the four Raman peaks decreased as the concentration of the BT solution was reduced (Figure 2.10b). The 3D stacked Au NP substrates effectively absorb the excitation light and generate stronger Raman enhancement, which allows the detection of picomolar concentrated BT.

The 3D stacked substrate showed excellent spatial uniformity as well. The use of a newly designed mechanical stirrer, which improved temperature and chemical concentration uniformity in the precursor solution, combined with repetitions of the Au synthesis resulted in a uniform AuNP layer over the entire substrate thick enough to saturate SERS emissions. As shown in Figure 2.11e, the substrate surface looks uniformly black. By conducting iterations of Au synthesis process, we were able to achieve saturated signal in entire substrate.

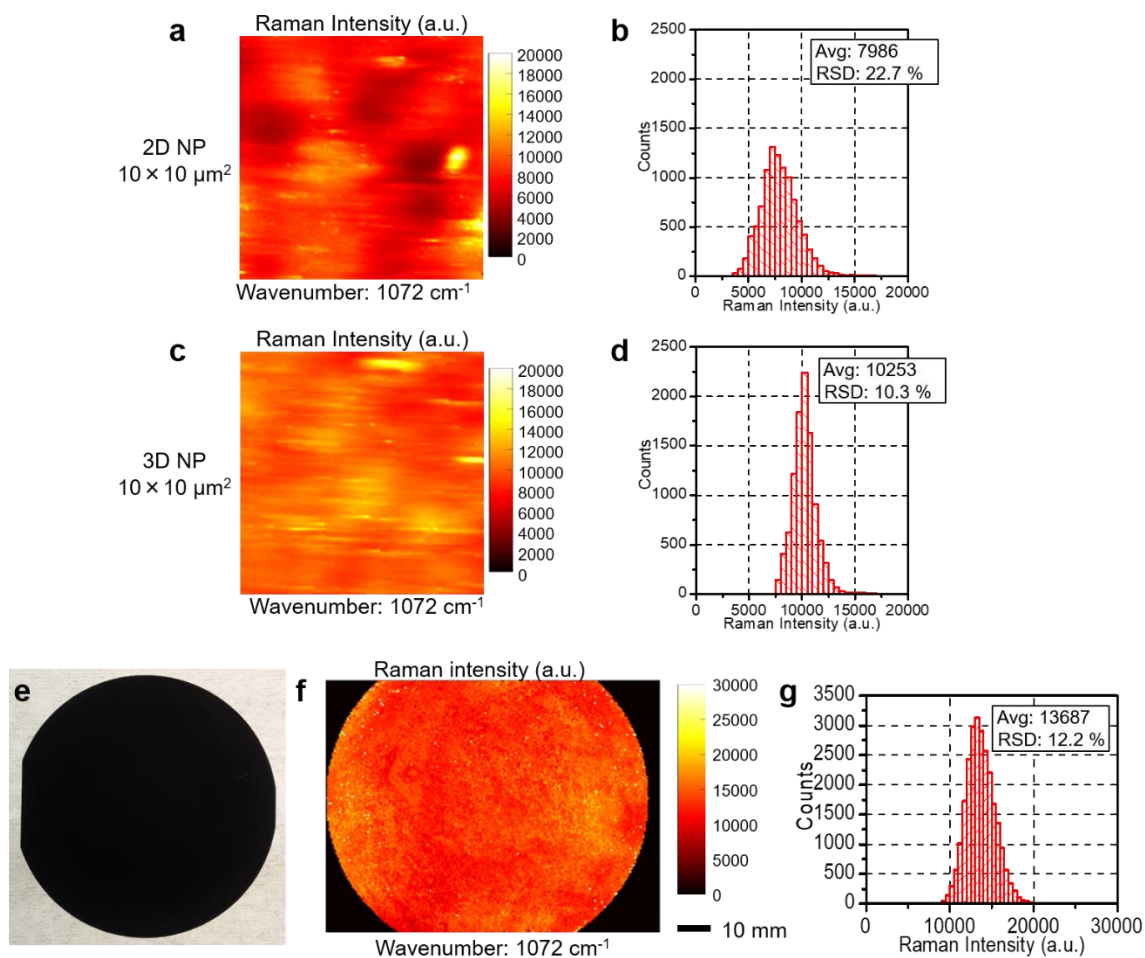


Figure 2.11: Spatial uniformity of Au NP substrates. (a) 2D Raman mapping and (b) statistical distribution of Raman intensity measured at 1072 cm⁻¹ on a 10 × 10 μm² 2D NP-8 substrate incubated in 1-mM benzenethiol solution; (c) 2D Raman mapping and (d) statistical distribution of Raman intensity measured on a 3D NP-8 substrate with same condition. (e) Photo of 3D-stacked Au NP synthesized on 4-inch wafer; (f) 2D mapping and (g) statistical distribution of 1 mM benzenethiol incubated 3D stacked Au NP synthesized on 4-inch wafer.

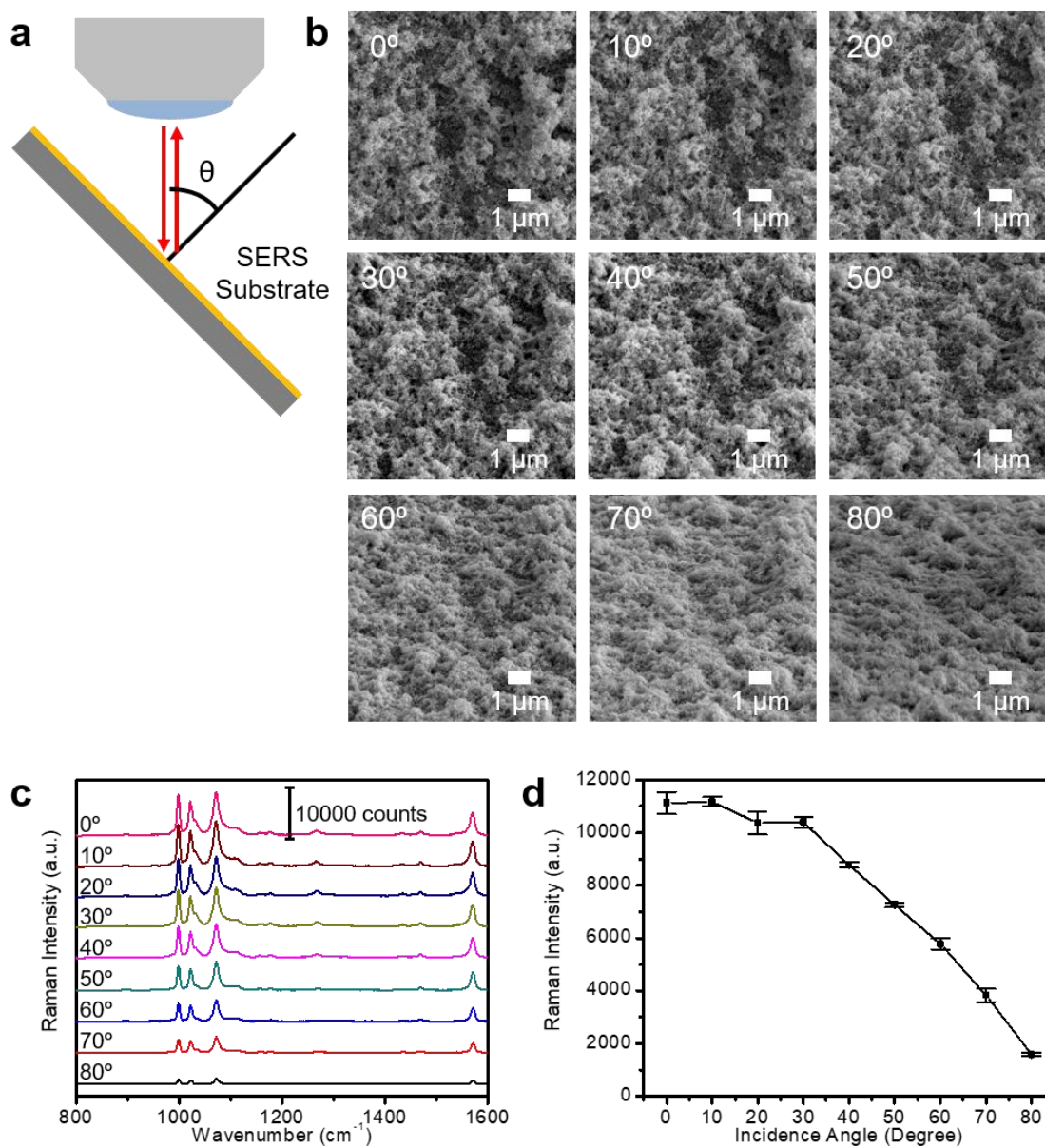


Figure 2.12: SERS spectra measurements by various incident angles of light. (a) Measurement set-up; (b) SEM images of tilted devices with 0 to 80 degrees; (c) SERS spectra of 1mM benzenethiol incubated 3D stacked Au NP substrate with various incidence angles and (d) relationship between SERS intensity and incidence angle.

The uniformity of the SERS intensity within an area of $10 \times 10 \mu\text{m}^2$ from 3D Au NP substrate showed a RSD around 10% (Figure 2.11c, d), which is more than twice as good as the flat 2D Au NP substrates (RSD > 20%) (Figure 2.11a, b). The large-scale spatial uniformity of the SERS intensity across the 4-in. wafer was excellent and had a relative standard deviation (RSD) below 13% (Figure 2.11f, g). The wafer-scale uniformity and strong enhancement were achieved using precursor-based fabrication processes that can be easily applied to large scale productions without significant setup investment. These desirable properties can provide high usability for practical applications such as quantitative monitoring of biological molecules.

We measured Raman intensities of BT as a function of incidence angles between 0 and 80 degrees (Figure 2.12a). Figure 2.12b shows the SEM images of the substrate with various angles. The intensities remained almost the same within 30 degrees of the incidence angle. In addition, the peak was observed even at 80 degrees of incidence angle as shown in Figure 2.12c, d. The rough surface reduces angle dependence of light reflection and the substrate provides thick layer regardless of the incident angle. This low angle dependence can also be very useful for practical applications that require quantitative measurements.

2.5. Quantitative Bio Molecule Measurements Using 3D Au NP Substrates

To demonstrate accurate quantitative bio molecule measurement, we measured Raman intensities of various concentrations (10 nM - 10 μM) of adenine solutions. Adenine is one of the nucleobases in the nucleic acid of DNA. The SERS substrate was diced into $2 \times 2 \text{ mm}^2$ chips for testing, and the SERS spectra were measured using 20 \times magnitude objective lens with 1.25- μm spot size and 0.07 mW of 785 nm laser for 100 s. We used a new chip for every measurement. For calibration measurements, we incubated four chips in 10-nM, 100-nM, 1- μM , and 10- μM adenine solutions for 5 h and measured the corresponding Raman spectra.

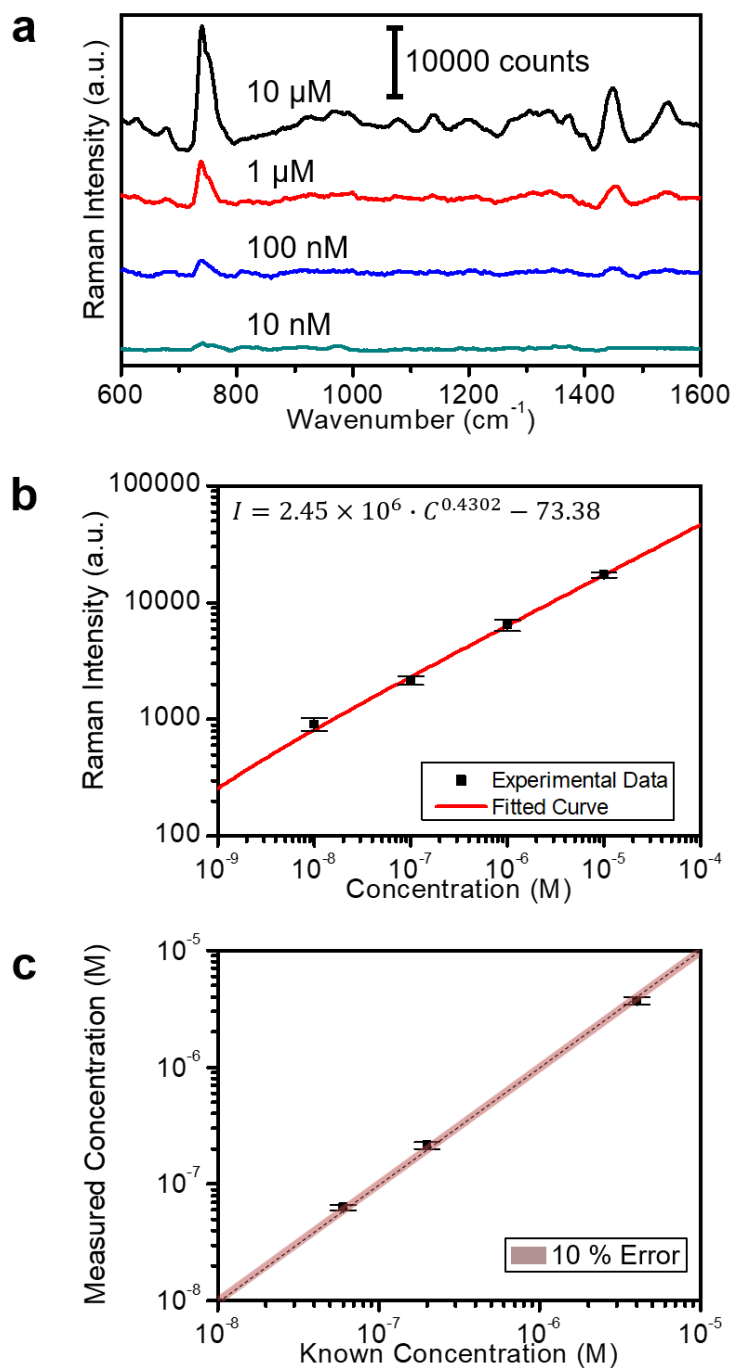


Figure 2.13: Quantitative SERS measurements using 3D Au NP substrates with adenine solutions. (a) Reference SERS spectra of 10 μ M, 1 μ M, 100 nM, and 10 nM adenine solution using 3D Au NP-8 substrate; (b) the experimentally measured relationship between concentration of adenine solution and SERS intensity; (c) concentration readouts for adenine solutions using 3D Au NP-8 substrate.

As shown in Figure 2.13a, clear Raman peaks were observed at the wavenumber 735 cm^{-1} and the peak intensities were proportional to the concentration of the adenine solution. The relationship between concentration and intensity was obtained as $I = 2.45 \times 10^6 \cdot C^{0.4302} - 73.38$, where I and C are the Raman intensity and the molar concentration of the solution, respectively (Figure 2.13b). In order to verify accuracy of our approach, we prepared 60-nM, 200-nM and 4- μM adenine solutions separately and incubated another set of $2 \times 2\text{ mm}^2$ chips in three different adenine concentrations and measured their SERS spectra under the same measurement conditions. Our method produced the concentration of 63.1 nM, 213.3 nM and 3.71 μM , respectively, matching well with the given concentration with 10 % accuracy (Figure 2.13c).

2.6. Conclusions

Using the hydrothermal synthesis method and LPD method, we have fabricated 3D Au NP clusters on ZnO nanowires and demonstrated their use as high performance stacked 3D SERS substrates. The volume and surface area of Au NP clusters were controlled by increasing the number of repetitions of the Au NP synthesis process. Additionally, ZnO nanowires act as a template for efficient fabrication of 3D structures. Due to the nanowire generated light-passing perforations and 3D stacks made of properly sized nanoparticles and interparticle gaps, the Raman-enhancing performance of the substrate is highly independent of the final geometry of the nanoparticle clusters and shows high enhancement and uniformity across the wafer, which is confirmed by experimental measurements.

The devices clearly detected SERS peaks in BT solution, and can measure as low as 1pM of BT concentration. The enhancement factor for this investigation was calculated to be approximately 9.31×10^9 . Also, the 3D Au NP substrate measured the concentration of a 60-nM adenine solution within 10%. This relatively simple approach can be widely adapted by most wet laboratories and is also suitable for large-scale productions, suggesting a promising way to implement commercial SERS substrates for biological and chemical sensing applications.

References

- Yang, D.; Cho, H.; Koo, S.; Vaidyanathan, S. R.; Woo, K.; Yoon, Y.; Choo, H. Simple, large-scale fabrication of uniform Raman-enhancing substrate with enhancement saturation. *ACS Appl. Mater. Interfaces*. 2017, 9 (22), 19092-19101.
- Andersen, L. Dinesen, B. Jørgensen, P. Poulsen, F. Røder, M. Enzyme immunoassay for intact human insulin in serum or plasma. *Clin. Chem.* 1993, 39, 578-582.
- Zhang, X.; Zhu, S.; Deng, C.; Zhang, X. An aptamer based onplate microarray for high-throughput insulin detection by MALDI-TOF MS. *Chem. Commun.* 2012, 48, 2689-2691.
- Cha, T.-G.; Baker, B. A.; Sauffer, M. D.; Salgado, J.; Jaroch, D.; Rickus, J. L.; Porterfield, D. M.; Choi, J. H. Optical nanosensor architecture for cell-signaling molecules using DNA aptamer-coated carbon nanotubes. *ACS Nano* 2011, 5, 4236-4244.
- Xu, M.; Luo, X.; Davis, J. J. The label free picomolar detection of insulin in blood serum. *Biosens. Bioelectron.* 2013, 39, 21-25.
- Roper, M. G.; Shackman, J. G.; Dahlgren, G. M.; Kennedy, R. T. Microfluidic chip for continuous monitoring of hormone secretion from live cells using an electrophoresis-based immunoassay. *Anal. Chem.* 2003, 75, 4711-4717.
- Guillo, C.; Roper, M. G. Two-color electrophoretic immunoassay for simultaneous measurement of insulin and glucagon content in islets of Langerhans. *Electrophoresis* 2008, 29, 410-416.
- Gobi, K. V.; Iwasaka, H.; Miura, N. Self-assembled PEG monolayer based SPR immunosensor for label-free detection of insulin. *Biosens. Bioelectron.* 2007, 22, 1382-1389.
- Wang, Y.; Gao, D.; Zhang, P.; Gong, P.; Chen, C.; Gao, G.; Cai, L. A near infrared fluorescence resonance energy transfer based aptamer biosensor for insulin detection in human plasma. *Chem. Commun.* 2014, 50, 811-813.
- Luo, X.; Xu, M.; Freeman, C.; James, T.; Davis, J. J. Ultrasensitive label free electrical detection of insulin in neat blood serum. *Anal. Chem.* 2013, 85, 4129-4134.
- Schnell, U.; Dijk, F.; Sjollem, K. A.; Giepmans, B. N. Immunolabeling artifacts and the need for live-cell imaging. *Nat. Methods* 2012, 9, 152-158.
- Blasi, T.; Hennig, H.; Summers, H. D.; Theis, F. J.; Cerveira, J.; Patterson, J. O.; Davies, D.; Filby, A.; Carpenter, A. E.; Rees, P. Labelfree cell cycle analysis for high-throughput imaging flow cytometry. *Nat. Commun.* 2016, 7, 10256.
- Fleischmann, M.; Hendra, P. J.; McQuillan, A. J. Raman spectra of pyridine adsorbed at a silver electrode. *Chem. Phys. Lett.* 1974, 26, 163-166.
- Albrecht, M. G.; Creighton, J. A. Anomalously intense Raman spectra of pyridine at a silver electrode. *J. Am. Chem. Soc.* 1977, 99, 5215-5217.
- Nie, S. M.; Emery, S. R. Probing single molecules and single nanoparticles by surface-enhanced Raman scattering. *Science* 1997, 275, 1102-1106.
- Kneipp, K.; Wang, Y.; Kneipp, H.; Perelman, L. T.; Itzkan, I.; Dasari, R. R.; Feld, M. S. Single molecule detection using surfaceenhanced Raman scattering (SERS). *Phys. Rev. Lett.* 1997, 78, 1667.

- Bantz, K. C.; Meyer, A. F.; Wittenberg, N. J.; Im, H.; Kurtulus, O.; Lee, S. H.; Lindquist, N. C.; Oh, S.-H.; Haynes, C. L. Recent progress in SERS biosensing. *Phys. Chem. Chem. Phys.* 2011, 13, 11551–11567.
- White, P. L.; Hibbitts, S. J.; Perry, M. D.; Green, J.; Stirling, E.; Woodford, L.; McNay, G.; Stevenson, R.; Barnes, R. A. Evaluation of a Commercially Developed Semiautomated PCR-Surface-Enhanced Raman Scattering Assay for Diagnosis of Invasive Fungal Disease. *J. Clin. Microbiol.* 2014, 52, 3536–3543.
- Campion, A.; Kambhampati, P. Surface-enhanced Raman scattering. *Chem. Soc. Rev.* 1998, 27, 241–250.
- Kambhampati, P.; Child, C. M.; Foster, M. C.; Campion, A. On the Chemical Mechanism of Surface Enhanced Raman Scattering: Experiment and Theory. *J. Chem. Phys.* 1998, 108, 5013–5026.
- Alonso-Gonzalez, P.; Albella, P.; Schnell, M.; Chen, J.; Huth, F.; Garcia-Etxarri, A.; Casanova, F.; Golmar, F.; Arzubiaga, L.; Hueso, L. E.; Aizpurua, J.; Hillenbrand, R. Resolving the electromagnetic mechanism of surface-enhanced light scattering at single hot spots. *Nat. Commun.* 2012, 3, 7.
- Schlucker, S. Surface-Enhanced Raman Spectroscopy: Concepts and Chemical Applications. *Angew. Chem.* 2014, 53, 4756–4795.
- Tong, L. M.; Zhu, T.; Liu, Z. F. Approaching the Electromagnetic Mechanism of Surface-Enhanced Raman Scattering: from Self-Assembled Arrays to Individual Gold Nanoparticles. *Chem. Soc. Rev.* 2011, 40, 1296–1304.
- Sun, M. T.; Wan, B. S.; Liu, Y. J.; Jia, Y.; Xu, H. X. Chemical Mechanism of Surface-Enhanced Resonance Raman Scattering via Charge Transfer in Pyridine-Ag-2 Complex. *J. Raman Spectrosc.* 2008, 39, 402–408.
- Zayak, A. T.; Hu, Y. S.; Choo, H.; Bokor, J.; Cabrini, S.; Schuck, P. J.; Neaton, J. B. Chemical Raman Enhancement of Organic Adsorbates on Metal Surfaces. *Phys. Rev. Lett.* 2011, 106, 083003.
- Braun, G.; Lee, S. J.; Dante, M.; Nguyen, T. Q.; Moskovits, M.; Reich, N. Surface-Enhanced Raman Spectroscopy for DNA Detection by Nanoparticle Assembly onto Smooth Metal Films. *J. Am. Chem. Soc.* 2007, 129, 6378–6379.
- Fang, J. X.; Yi, Y.; Ding, B. J.; Song, X. P. A Route to Increase the Enhancement Factor of Surface Enhanced Raman Scattering (SERS) via a High Density Ag Flower-Like Pattern. *Appl. Phys. Lett.* 2008, 92, 131115.
- Wang, J. H.; Zhou, W. M.; Zhang, J.; Yang, M. J.; Ji, C. T.; Shao, X. X.; Shi, L. Y. High-fidelity replica molding for large-area PMMA 3D nanostructures with high performance surface-enhanced Raman scattering and hydrophobicity. *Microelectron. Eng.* 2014, 115, 2–5.
- Chirumamilla, M.; Toma, A.; Gopalakrishnan, A.; Das, G.; Zaccaria, R. P.; Krahne, R.; Rondanina, E.; Leoncini, M.; Liberale, C.; De Angelis, F.; Di Fabrizio, E. 3D Nanostar Dimers with a Sub-10-nm Gap for Single-/Few- Molecule Surface-Enhanced Raman Scattering. *Adv. Mater.* 2014, 26, 2353–2358.
- Tang, H. B.; Meng, G. W.; Huang, Q.; Zhang, Z.; Huang, Z. L.; Zhu, C. H. Arrays of Cone-Shaped ZnO Nanorods Decorated with Ag Nanoparticles as 3D Surface-Enhanced Raman Scattering Substrates for Rapid Detection of Trace Polychlorinated Biphenyls. *Adv. Funct. Mater.* 2012, 22, 218–224.

- Liu, Y.; Zhang, X. H.; Su, J.; Li, H. X.; Zhang, Q.; Gao, Y. H. Ag nanoparticles@ZnO nanowire composite arrays: an absorption enhanced UV photodetector. *Opt. Express* 2014, 22, 30148-30155.
- Dai, Z. G.; Wang, G. M.; Xiao, X. H.; Wu, W.; Li, W. Q.; Ying, J. J.; Zheng, J. F.; Mei, F.; Fu, L.; Wang, J.; Jiang, C. Z. Obviously Angular, Cuboid-Shaped TiO₂ Nanowire Arrays Decorated with Ag Nanoparticle as Ultrasensitive 3D Surface-Enhanced Raman Scattering Substrates. *J. Phys. Chem. C* 2014, 118, 22711-22718.
- Bai, F.; Li, M. C.; Fu, P. F.; Li, R. K.; Gu, T. S.; Huang, R.; Chen, Z.; Jiang, B.; Li, Y. F. Silicon nanowire arrays coated with electroless Ag for increased surface-enhanced Raman scattering. *Apl Materials* 2015, 3, 6.
- Fu, S. Y.; Hsu, Y. K.; Chen, M. H.; Chuang, C. J.; Chen, Y. C.; Lin, Y. G. Silver-decorated hierarchical cuprous oxide micro/nanospheres as highly effective surface-enhanced Raman scattering substrates. *Opt. Express* 2014, 22, 14617-14624.
- Zhou, Q. T.; Meng, G. W.; Huang, Q.; Zhu, C. H.; Tang, H. B.; Qian, Y. W.; Chen, B.; Chen, B. S. Ag-nanoparticles-decorated NiO-nanoflakes grafted Ni-nanorod arrays stuck out of porous AAO as effective SERS substrates. *Phys. Chem. Chem. Phys.* 2014, 16, 3686-3692.
- Zhang, W. H.; Cui, X. D.; Yeo, B. S.; Schmid, T.; Hafner, C.; Zenobi, R. Nanoscale roughness on metal surfaces can increase tip-enhanced Raman scattering by an order of magnitude. *Nano Lett.* 2007, 7, 1401-1405.
- Fraire, J. C.; Perez, L. A.; Coronado, E. A. Cluster Size Effects in the Surface-Enhanced Raman Scattering Response of Ag and Au Nanoparticle Aggregates: Experimental and Theoretical Insight. *J. Phys. Chem. C* 2013, 117, 23090-23107.
- Zhao, X. M.; Zhang, B. H.; Ai, K. L.; Zhang, G.; Cao, L. Y.; Liu, X. J.; Sun, H. M.; Wang, H. S.; Lu, L. H. Monitoring catalytic degradation of dye molecules on silver-coated ZnO nanowire arrays by surface-enhanced Raman spectroscopy. *J. Mater. Chem.* 2009, 19, 5547-5553.
- He, X.; Wang, H.; Zhang, Q.; Li, Z. B.; Wang, X. C. Exotic 3D Hierarchical ZnO-Ag Hybrids as Recyclable Surface-Enhanced Raman Scattering Substrates for Multifold Organic Pollutant Detection. *Eur. J. Inorg. Chem.*, 2014, 2432-2439.
- Jang, J. M.; Kim, S. D.; Choi, H. M.; Kim, J. Y.; Jung, W. G. Morphology change of self-assembled ZnO 3D nanostructures with different pH in the simple hydrothermal process. *Mater. Chem. Phys.* 2009, 113, 389-394.
- Willander, M.; Yang, L. L.; Wadeasa, A.; Ali, S. U.; Asif, M. H.; Zhao, Q. X.; Nur, O. Zinc oxide nanowires: controlled low temperature growth and some electrochemical and optical nano-devices. *J. Mater. Chem.* 2009, 19, 1006-1018.
- Guo, M.; Diao, P.; Cai, S. M. Hydrothermal growth of well-aligned ZnO nanorod arrays: Dependence of morphology and alignment ordering upon preparing conditions. *J. Solid State Chem.* 2005, 178, 1864-1873.
- Li, J. Y.; Zhang, Q.; Peng, H. Y.; Everitt, H. O.; Qin, L. C.; Liu, J. Diameter-Controlled Vapor-Solid Epitaxial Growth and Properties of Aligned ZnO Nanowire Arrays. *J. Phys. Chem. C* 2009, 113, 3950-3954.
- Zhang, P.; Yang, S.; Wang, L.; Zhao, J.; Zhu, Z.; Liu, B.; Zhong, J.; Sun, X. Large-scale uniform Au nanodisk arrays fabricated via x-ray interference lithography for reproducible and sensitive SERS substrate. *Nanotechnology* 2014, 25.

- Tang, X.; Cai, W.; Yang, L.; Liu, J. Highly uniform and optical visualization of SERS substrate for pesticide analysis based on Au nanoparticles grafted on dendritic alpha-Fe₂O₃. *Nanoscale* 2013, 5, 11193-11199.
- Pazos-Perez, N.; Ni, W.; Schweikart, A.; Alvarez-Puebla, R. A.; Fery, A.; Liz-Marzan, L. M. Highly uniform SERS substrates formed by wrinkle-confined drying of gold colloids. *Chem. Sci.* 2010, 1, 174-178.
- Law, M.; Greene, L. E.; Johnson, J. C.; Saykally, R.; Yang, P. D. Nanowire dye-sensitized solar cells. *Nat. Mater.* 2005, 4, 455-459.
- Acosta, B.; Smolentseva, E.; Beloshapkin, S.; Rangel, R.; Estrada, M.; Fuentes, S.; Simakov, A. Gold supported on ceria nanoparticles and nanotubes. *Appl. Catal. A: Gen.* 2012, 449, 96-104.
- Castillo, F.; Perez, E.; de la Rosa, E. Adsorption of gold nanoparticles on silicon substrate and their application in Surface Enhancement Raman Scattering. *Rev. Mex. Fis.* 2011, 57, 61-65.
- Moreau, F.; Bond, G. C.; Taylor, A. O. Gold on titania catalysts for the oxidation of carbon monoxide: control of pH during preparation with various gold contents. *J. Catal.* 2005, 231, 105-114.
- Lim, M. A.; Lee, Y. W.; Han, S. W.; Park, I. Novel fabrication method of diverse one-dimensional Pt/ZnO hybrid nanostructures and its sensor application. *Nanotechnology* 2011, 22, 8.
- Haruta, M. Nanoparticulate gold catalysts for low-temperature CO oxidation. *J. New Mat. Electrochem. Syst.* 2004, 7, 163-172.
- Greene, L. E.; Law, M.; Tan, D. H.; Montano, M.; Goldberger, J.; Somorjai, G.; Yang, P. D. General route to vertical ZnO nanowire arrays using textured ZnO seeds. *Nano Lett.* 2005, 5, 1231-1236.
- Zang, J.; Li, C. M.; Cui, X.; Wang, J.; Sun, X.; Dong, H.; Sun, C. Q. Tailoring zinc oxide nanowires for high performance amperometric glucose sensor. *Electroanalysis* 2007, 19, 1008-1014.
- Joo, T. H.; Kim, M. S.; Kim, K. Surface-enhanced Raman-scattering of benzenethiol in silver sol. *J. Raman Spectrosc.* 1987, 18, 57-60.
- Hong, S. M.; Li, X. Optimal Size of Gold Nanoparticles for Surface-Enhanced Raman Spectroscopy under Different Conditions. *J. Nanomater.* 2013, 9.

*Chapter 3***SURFACE-ENHANCED RAMAN SPECTROSCOPY-BASED LABEL-FREE
INSULIN DETECTION**

Label-free optical detection of insulin would allow in vitro assessment of pancreatic cell functions in their natural state and expedite diabetes-related clinical research, however no existing method has met these criteria at physiological concentrations. Herein, surface-enhanced Raman sensing of insulin was demonstrated on a spatially uniform 3D gold nanoparticle sensors, without the use of labels such as antibodies or aptamers. Following a 785 nm laser excitation, the sensor exhibited a dynamic range of 100 pM to 50 nM, covering the reported concentration range of insulin observed in pancreatic cell secretions. Plasmonic hotspots of the densely stacked, 3D gold nanoparticle pillars as well as strong interaction between sulphide linkages of the insulin molecules and the gold nanoparticles produced highly sensitive and reliable insulin measurements down to 100 pM, with an estimated detection limit of 35 pM. The sensitivity of this approach is approximately four orders of magnitude greater than previously reported results using label-free optical approaches and may open new opportunities for insulin sensing in research and clinical applications.

Part of the work that appears in this chapter was published and is included here with the permission of the publisher as shown below.

"Reprinted (adapted) with permission from Hyunjun Cho, Shailabh Kumar, Daejong Yang, Sagar Vaidyanathan, Kelly Woo, Ian Garcia, Hao J. Shue, Youngzoon Yoon, Kevin Ferreri, and Hyuck Choo, *ACS Sensors* **2018** 3 (1), 65-71. DOI: 10.1021/acssensors.7b00864. Copyright 2018 American Chemical Society."

3.1. SERS-Based Insulin Measurements

One of the most prevalent diseases resulting from hormonal dysfunction is diabetes, which arises from a disruption in the release of insulin in the body (Seltzer et al., 1967; Weyer et al., 1999). Insulin is a peptide hormone secreted by beta cells in the pancreas and controls the blood-glucose level. The concentration of insulin secreted from beta cells in plasma has been reported to vary between 100 pM (fasting) and 2 nM (about 1 hour after glucose intake) in non-diabetic individuals (Yalow and Berson, 1960; Melmed et al., 2011). In diabetic individuals, functional damage to the beta cells reduces or inhibits their ability to release insulin. One of the leading methodologies for treatment of type-1 diabetes is pancreatic islet transplantation, where healthy islets harvested from deceased donors are transplanted into diabetic patients (Shapiro et al., 2000; Barton et al., 2012). Since the number of donors is limited, methodologies that can improve the efficiency and success of the transplantation process are urgently needed. Before transplantation, these islets are screened for their viability and functional response to changing glucose concentration in order to reduce the chances of transplant failure (Nano et al., 2005; Sweet et al., 2008; Papas et al., 2009). Sensors capable of detecting secretion of insulin from beta cells in a cost-effective, label-free manner with minimal stress to the cells can serve vital roles in clinical quality assessments of islets. External monitoring of insulin concentration can also help in disease diagnosis and management, as well as prevent potentially fatal insulin overdoses or hypoglycemia in diabetic patients (Mork et al., 2011).

Even though Surface-enhanced Raman spectroscopy (SERS) among various sensing methods can be an ideal approach for optical label-free sensing for applications like pancreatic islet transplantation, using SERS for hormone detection appears relatively unexplored due to minimal experimental success: previously reported SERS-based quantitative insulin sensors were limited due to weakly-enhancing substrates made of randomly dispersed nanoparticles resulting in micromolar detection sensitivity, approximately 2 to 4 orders of magnitude larger than physiological insulin levels (Drachev et al., 2005; Keskin et al., 2011; Matteini et al., 2015). In this study, we report rapid and

highly sensitive SERS-based insulin sensing at clinically relevant concentrations using a non-resonant SERS substrate with strong signal enhancement and wafer-scale uniformity.

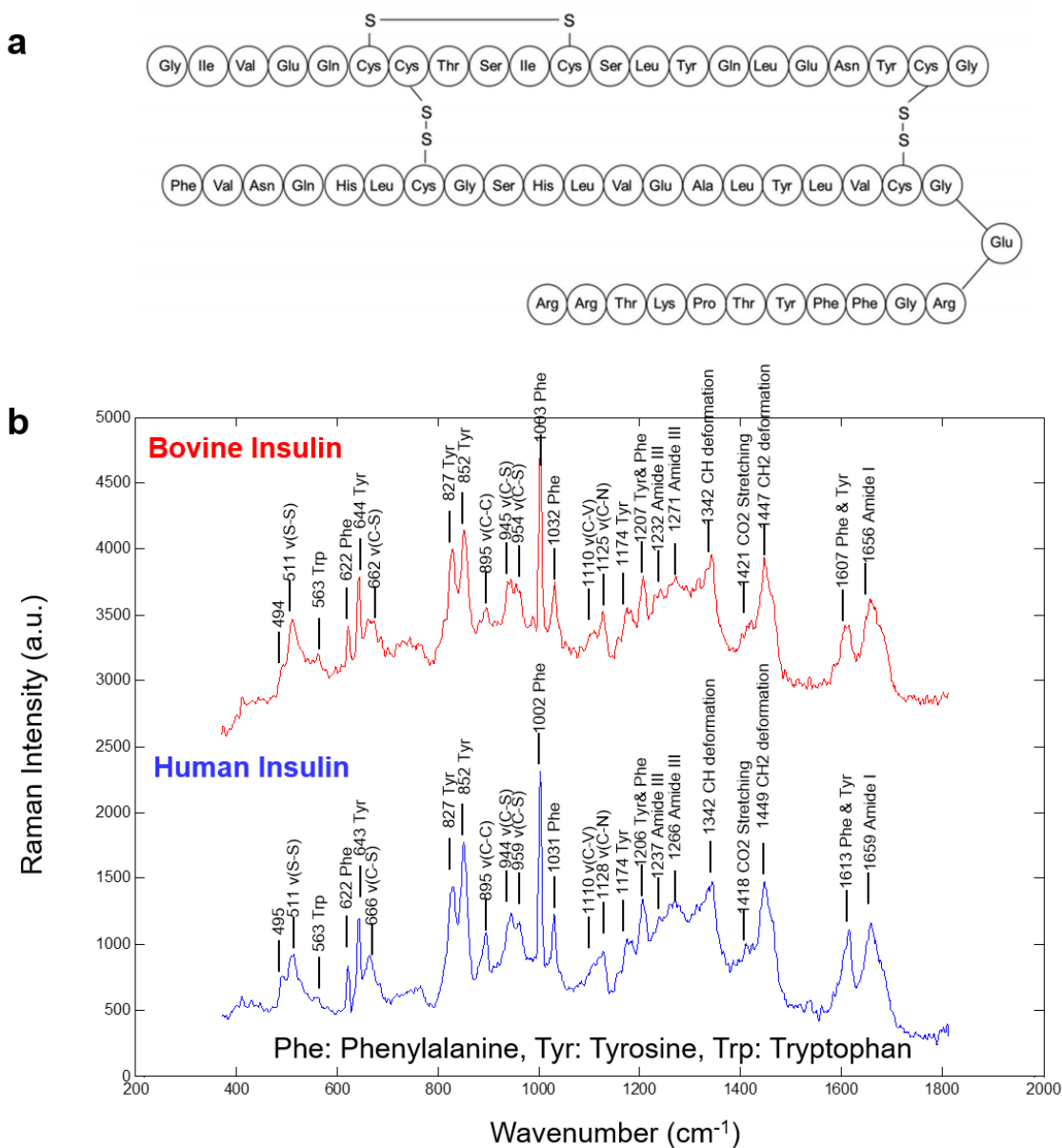


Figure 3.1: Raman peaks corresponding to the amino acids of insulin. (a) Amino acid composition of insulin (Hilderink et al., 2013). (b) Measured Raman spectra from human insulin and bovine insulin.

For the insulin measurements, purified human recombinant insulin was obtained from Sigma-Aldrich Corp. (St. Louis, MO, USA). Insulin from bovine pancreas (Sigma-Aldrich) was also used. Prior to SERS measurements, Raman spectra from these types of insulin were analyzed. The powder form of insulin was placed on the microscope slide, then covered by a quartz cover slip (Esco Optics). Raman spectra of insulin were obtained using a Renishaw inVia Raman Microscope with 20× magnification objective lens and 785 nm infrared (IR) laser. The laser power was 0.93 mW at the sample and the integration time was 100 seconds.

The measured spectra of human and bovine insulin are shown in Figure 3.1b. Amino acids and bonds, which contribute to making the Raman peaks such as phenylalanine, tyrosine, tryptophan, are noted with reference to the literature (Yu et al., 1972). The amino acid composition of insulin is shown in Figure 3.1a (Hilderink et al., 2013). Insulin is composed of two peptide chains: A chain and B chain. These two chains are linked together by two disulfide bonds. In human insulin, the A chain consists of 21 amino acids and the B chain of 30 amino acids. The strongest peak is found at 1002 cm^{-1} corresponding to the ring-breathing mode of aromatic phenylalanine.

The SERS sensors were batch-fabricated using a simple two-step process that produced 3-dimensional (3D) gold-nanoparticle (Au NP) clusters packed densely in a vertical, pillar-like arrangement as introduced in chapter 2 (Figure 2.1b; Figure 2.2). We fabricated 4-inch scale 3D-stacked gold-nanoparticle (Au NP) substrates with five iterations of NP synthesis on ZnO synthesized Si substrates (Au NW-5) which showed saturated a SERS spectrum with 1 mM BT solution (Figure 2.9d).

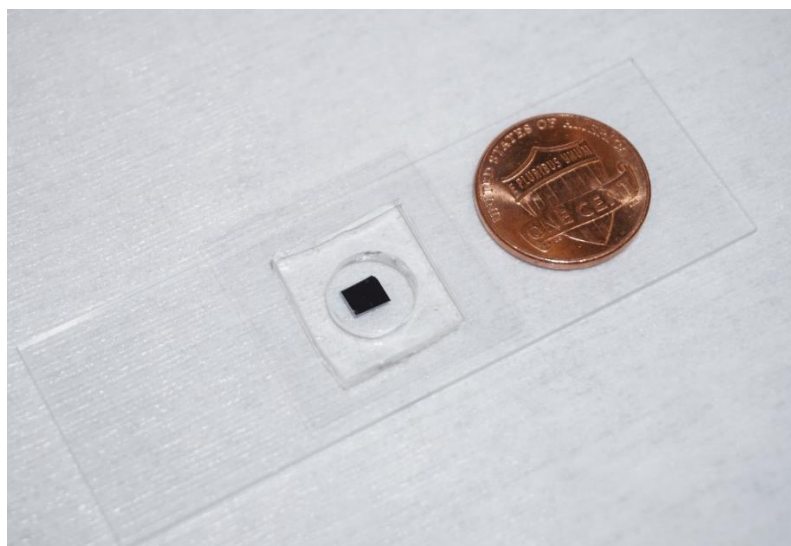


Figure 3.2: $5 \times 5 \text{ mm}^2$ SERS chip incubated inside the PDMS chamber with $200 \mu\text{L}$ of insulin solution.

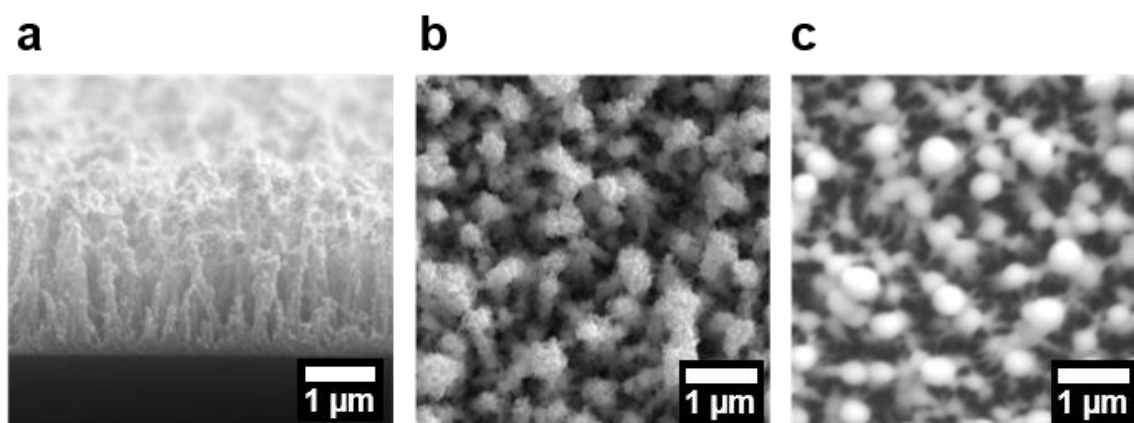


Figure 3.3: SEM images of 3D Au NP substrate coated with insulin. (a) Cross-sectional SEM image showing the vertical pillar-like 3D arrangement of the Au NP clusters on the ZnO synthesized substrate. SEM images (top view) of a substrate (b) before and (c) after insulin incubation.

Insulin solution with 1 mM of human insulin was prepared in phosphate-buffered saline (PBS), pH 7.4. The silicon wafer with 3D Au-NP clusters was cleaved into $5 \times 5 \text{ mm}^2$ sensing chips and placed inside polydimethylsiloxane (PDMS) chambers with an inner volume of $200 \mu\text{L}$ (Figure 3.2). The insulin was added to the chambers without stirring and

the PDMS chambers were covered with quartz cover slips. The samples were left undisturbed for 12 hours at room temperature for diffusion-dependent transport and binding of insulin to the highly dense 3D stacked Au NP pillars. Following this incubation, the samples were rinsed with DI water and dried using an air gun.

The cross-sectional view of the 3D Au NP SERS substrate acquired using scanning electron microscopy (SEM, FEI Nova 200 NanoLab dualbeam system) is shown in Figure 3.3a. The SEM image reveals a dense, vertical arrangement of gold nanoparticle clusters that, based on experimental results, provide plasmonic hotspots necessary for ultrasensitive optical detection as described in Chapter 2. SEM images in Figure 3.3b and c show Au NP clusters before and after adsorption of 1 μM insulin, respectively.

Raman spectrum obtained from powdered insulin (Figure 3.4a) was replotted in 600-1400 cm^{-1} range of wavenumber as reference Raman signatures for insulin sensing. Also, SERS spectrum from 3D Au NP clusters incubated in 1 mM insulin was collected and show consistent peak intensities and locations (Figure 3.4b). The most intense peak at 1002 cm^{-1} was used to monitor the change in Raman intensity as a function of insulin concentration (Hilderink et al., 2013; Ortiz et al., 2004).

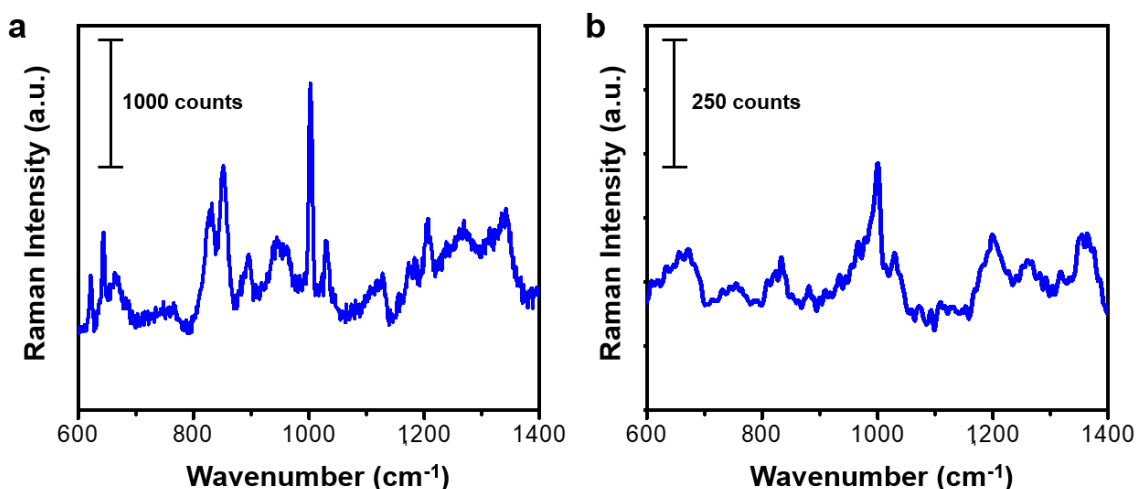


Figure 3.4: Raman spectra of (a) human insulin powder and (b) SERS substrate incubated in 1 mM insulin solution.

Insulin solutions at concentrations ranging from 100 pM to 1 mM were prepared in phosphate-buffered saline (PBS), pH 7.4. Measurements were performed at the center of each chip and at four additional points – top, bottom, left, and right, about 0.5 mm away from the center location – to characterize the Raman intensity and spatial uniformity.

3.2. SERS-Based Quantitative Measurements for Low-Level Insulin Detection

For quantitative SERS measurements for low-level insulin detection, insulin solutions at concentrations ranging from 100 pM to 1 mM were prepared in phosphate-buffered saline (PBS), pH 7.4. The 3D Au NP cluster chips were incubated in these insulin solutions for 12 hours at room temperature. Following this incubation, the samples were rinsed with DI water and dried using an air gun. The measurement condition using Renishaw inVia was 0.93 mW of laser power with 785 nm IR laser and 100 seconds of integration time.

The change in SERS signal intensity as a function of insulin concentration between 100 pM to 50 nM is shown in Figures 3.5a and b. The peak at 1002 cm^{-1} was identifiable at 100 pM and a linear increase in the Raman intensity was observed as the insulin concentration increased from 100 pM to 10 nM. The inset of Figure 3.5b shows a linear relationship between the Raman intensity and concentration from 100 pM to 10 nM (slope = 0.341, y-intercept = 12.6). The Raman intensity reached saturation at insulin concentrations greater than 50 nM, which indicates an almost complete monolayer coverage. Insulin can exist in solutions as a hexamer (~ 5 nm in diameter and 3.5 nm in height) in the presence of zinc ions at neutral pH, as a dimer (~ 4.5 nm diameter and ~ 2 nm in height) or as a monomer (~ 2 nm diameter and height ~ 2 nm) (Blundell et al., 1972). As no zinc ions were added to insulin containing buffers, the molecules are expected to be in a monomer-dimer equilibrium. Given the size of insulin molecules, even if there were a second layer sitting on top of the first layer, the second layer would be too far away from the surface to significantly benefit from the near-field enhancement on the surface, and the Raman-emission contribution by the second and/or third layers would be minimal (Masango et al., 2016). The signal-to-noise ratio (SNR) at 100 pM was calculated to be approximately 8.5,

and the theoretical detection limit was calculated to be 35 pM for a minimum acceptable SNR of 3.

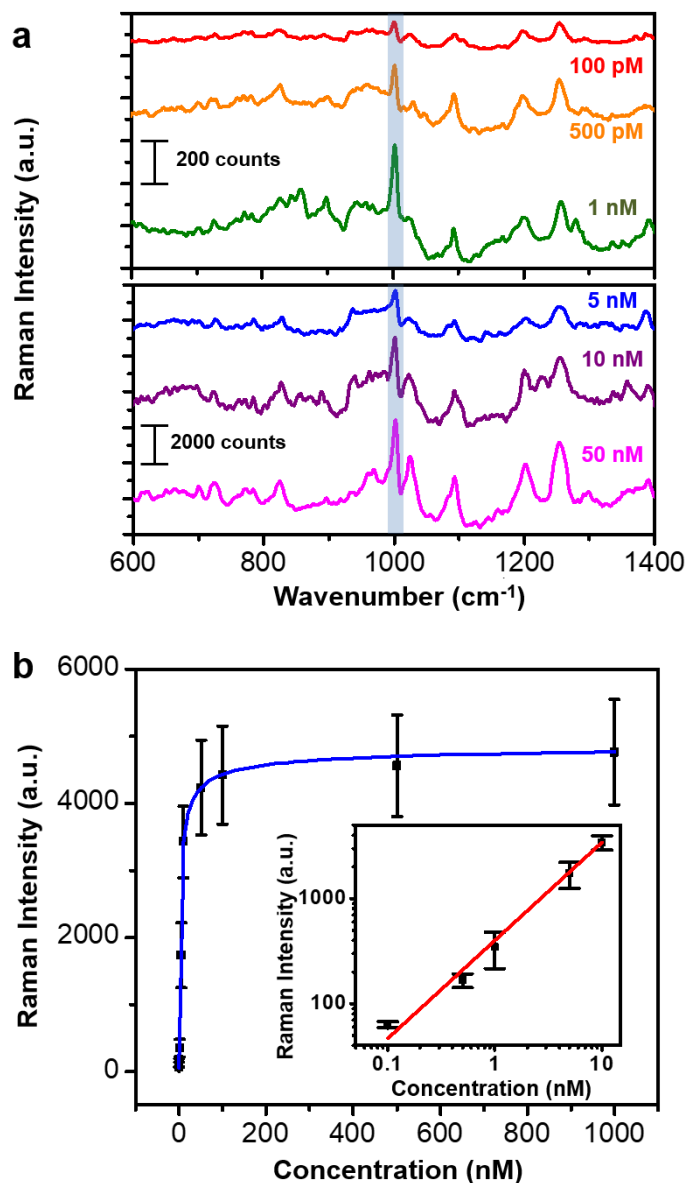


Figure 3.5: Quantitative measurements of insulin solutions. (a) SERS spectra of 100 pM, 500 pM, 1 nM, 5 nM, 10 nM, 50 nM human insulin solutions highlighting the target peak at 1002 cm⁻¹. (b) Experimentally measured relationship between the insulin concentration and SERS intensity; the inset shows a linear relationship between the Raman intensity and concentration from 100 pM to 10 nM.

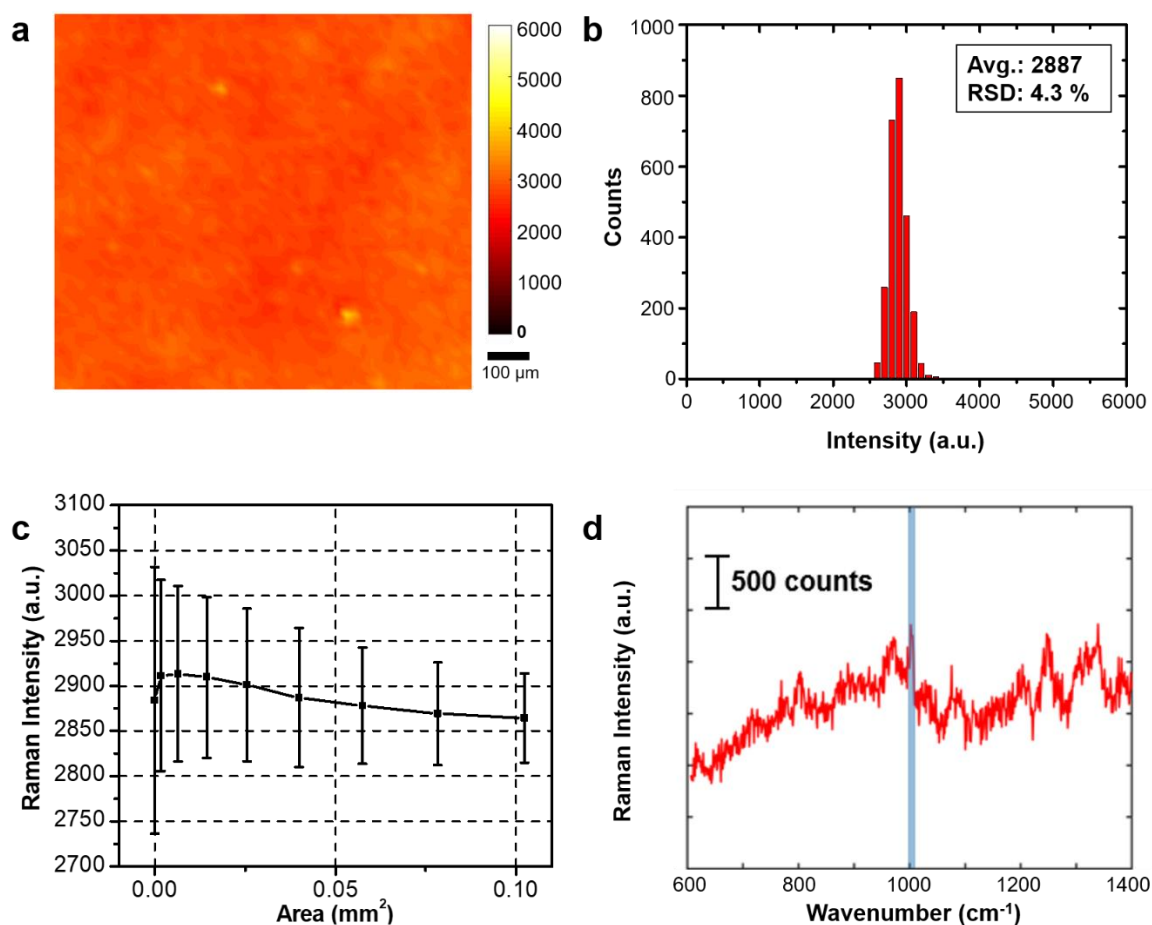


Figure 3.6: Evaluation of insulin coated SERS substrates. (a) 2D Raman-intensity mapping of a SERS chip after incubating in a 10 nM insulin solution. The RSD of the Raman signal over the $1 \times 1 \text{ mm}^2$ area was found to be 4.3%, demonstrating excellent spatial uniformity. (b) Histogram showing the narrow distribution of Raman intensity over the mapped region. (c) Graph showing the mean and standard deviation of Raman signals collected from the sample as a function of the scan size used for areal averaging. (d) A SERS spectrum captured from a 3D Au NP SERS chip coated with a drop of 100-pM human insulin solution followed by rapid on-chip evaporation.

For typical SERS substrates, even a small displacement of the incident laser could often lead to a huge change in Raman signal intensity due to non-uniformly distributed SERS hotspots. In order to improve the consistency of SERS measurements, recent focus has been placed on improving the chip-scale measurement uniformity either by implementing better substrates (Kanipe et al., 2016; Lin et al., 2017; Yang et al., 2017; Hoang et al.,

2017), or employing better measurement strategies such as areal averaging (Lee et al., 2011; Chang et al., 2016), which involves scanning a larger area on the substrate to collect and average more Raman-signal data points as opposed to making a single point measurement.

The SERS insulin sensor using 3D-stacked Au NP substrates showed excellent spatial uniformity. Two-dimensional (2D) mapping of Raman spectra was performed over a 1×1 mm² area with a step size of 20 μ m on a chip coated with a 10 nM insulin solution. For fast measurements, the measurement condition was changed to 12 mW laser power at the sample and 10 second integration time at each spot. The 2D mapping data is shown in Figure 3.6a. The relative standard deviation (RSD) of the signal fluctuation was 4.3%, indicating uniform enhancement of Raman signal over a large area of the sensor. A histogram of the Raman signals obtained over the mapped region also reveals a very narrow intensity distribution and indicates uniform enhancement (Figure 3.6b). Areal averaging was also explored to further improve the spatial uniformity of Raman measurements. Figure 3.6d shows the RSD as a function of the scan area used for averaging. The results show that increasing the averaging scan area improves the measurement uniformity. For example, increasing the average scan area from 50×50 μ m² to 400×400 μ m² reduces the RSD from 3.6% to 1.7%. However, it should be noted that the improvement in measurement uniformity from areal averaging is small, only about 1-3%, which is a testament to the excellent spatial uniformity of the 3D Au NP substrate.

In order to demonstrate a practical, rapid detection of low-level insulin using the SERS substrate, a 200 μ L drop of 100-pM insulin solution was applied to the surface of fresh SERS chips and dried by placing on a hotplate (without stirring) at 50°C for 30 minutes. The locations and intensities of the Raman peaks measured from the evaporation-prepared samples (Figure 3.6d) matched the substrates incubated in insulin solutions for 12 hours. The droplet is typically 0.5 cm in diameter, and signal was collected from central regions of the placed droplet, where insulin transport should be governed by diffusion and any thermal gradient-derived convective currents, thus avoiding the edges where evaporation-

driven concentrating ring effects are observed. As mentioned earlier, even if more than one layer of molecules were assembled on the surface, the second layer would be too far away from the surface to benefit from the near-field enhancement on the surface as the Raman-emission contribution by the second and/or third layers would be minimal (Masango et al., 2016). A <10% SNR reduction was observed in the faster evaporation-detection technique and the minimum detectable concentration was calculated to be approximately 40 pM.

From our measurements, the enhancement factor of the substrate for sensing insulin was calculated to be 3×10^7 (Drachev et al., 2005). This enhancement primarily originates from the exceptionally strong plasmonic (electromagnetic) enhancement of the 3D Au NP clusters. Capture of insulin on the gold substrate can be mediated through two possible interactions: a) hydrophobic regions of the insulin molecules can promote adsorption to the substrate, which exhibits extreme hydrophobicity with a measured water-substrate contact angle of 140 degrees and b) through strong binding interaction between the disulphide bonds of insulin molecules and the gold atoms of the SERS substrate (Keskin et al., 2011; Matteini et al., 2015; Kanipe et al., 31). The chemical interaction between sulphur and gold atoms is well known and has been extensively utilized by researchers in the form of thiol-gold linkages (Lin et al., 2017; Yang et al., 2017). These interactions between the insulin molecules and gold substrate can further contribute towards the enhancement of the Raman signal through the mechanism known as chemical enhancement of SERS (Hoang et al., 2017).

3.3. SERS-Based Sensing of Human Pancreatic Islet Secretion

We then utilized our label-free sensing method to assess the functionality of human pancreatic islets. Secretions from the islets were collected using a flow-culture system under low glucose (3 mM) and high glucose (17 mM) environments. Human islets were provided for research use by the Southern California Islet Cell Resources Center at the City of Hope (COH, Duarte, CA) with the approval of the COH Institutional Review Board and with written informed consent. Human islets were isolated by a modified Riccordi method

as described previously (Sweet et al., 2008). We established the insulin concentrations of the collected secretion samples by performing the ELISA on an aliquot extracted from each secretion sample. Briefly, 750 human islets were placed into a flow culture system and perfused at 37 °C in an air/5% CO₂ incubator with low (3 mM) or high glucose (17 mM) Krebs-Ringer-Bicarbonate buffer containing 1% human serum albumin. Samples (375 microliters) were collected at 5-minute intervals and kept at -80 °C until assessed for insulin concentration by ELISA (Human Insulin ELISA kit, Merckodia Inc., Winston Salem, NC, cat# 10-1113-01) or SERS.

For preparation of SERS-based sensors, we applied the collected secretion samples to 3D Au NP cluster chips and measured SERS signals. 5×5 mm² sensing chips were placed inside polydimethylsiloxane (PDMS) chambers, the islet secretions (200 μL) were added to the chambers without stirring and the PDMS chambers were covered with quartz cover slips. In the islet-secretion measurements, the Raman intensity of the insulin peak at 1002 cm⁻¹ consistently increased as a function of increasing glucose and insulin concentrations (Figure 3.7). Difference in the SERS intensity from low-glucose (Figure 3.7c) and high-glucose (Figure 3.7d) secretions was clearly visible.

The islet measurements also showed a highly linear relationship with the ELISA measurements as shown in Figure 3.8b, and this linear relationship was well described by a line whose slope is the same as that obtained in the calibration test. We compared the SERS signals of the islet secretions with those obtained previously in the calibration test performed on insulin in PBS buffer. A regression analysis was carried out on the islet-secretion measurements by fitting a line with the slope obtained from the calibration test (Figure 3.8b). While the slopes are the same, the y-intercept of the line fitted to the islet-secretion measurements (Figure 3b, y-intercept = 74.8) is approximately six times larger than that of the line fitted to the calibration-test results (inset of Figure 3.5b, y-intercept = 12.6), indicating that the line was shifted upward for the islet case. This was due to the presence of other molecules (primarily HSA) in the islet-secretion buffer, leading to an increase in the background intensity bias that pushed up the overall spectral intensity. Other

than the difference in the background intensity bias, our islet-secretion measurements were highly consistent with the calibration measurements made using insulin in PBS. The coefficient of determination (R^2) was 0.97, indicating an excellent linear fit (Figure 3b).

The RSDs for the Raman signals from islet-secretion samples were calculated as 5 % and 5.3 % for the low- and high-glucose samples, respectively, and showed a small increase as compared to 4.3 % obtained from calibration-test samples (Figure 3.6c). There was no significant change in the calculated detection limit for the islet secretions, which was estimated at approximately 36 pM using a SNR threshold of 3. Although the constant bias of the background signal (indicated by the elevated y-intercept in Figure 3b as compared to the y-intercept in Figure 3.5b (inset)) increased by a factor of six, the mean noise level (after subtracting the background bias) remained almost the same as in the islet-measurement case. As a result, the SNR remains almost constant from the insulin-in-PBS case to the islet case. Also, the slope of the Raman-intensity vs. insulin concentrations produced using our approach remained the same in both cases as shown in Fig. 3b even if the background bias increased in the islet case. The detection limit in this case signifies the minimum detectable change in insulin concentration in the target concentration range, which is important to characterize islet performance.

The increase in the background noise (after subtracting the constant bias) in the islet case was minimal because the influence of other molecules on our measurements was very weak. As glucose has a weak Raman cross-section and poor adhesion to metals (McCreery, 2000; Shafer-Peltier et al., 2003), change in glucose concentration has no influence on the obtained Raman signal. The influence on Raman signals from other hormones such as glucagon, amylin, somatostatin, and pancreatic polypeptide whose concentration could change in response to elevating glucose levels was considered as a potential source of error. However, the physiological concentration of glucagon released in islet secretions is less than 17 pM, which is lower than the detection limit of the sensor, and its influence was considered insignificant (Alford et al., 1977; Gardner et al., 2011). The concentration levels of amylin and somatostatin in the islet secretion are also very small, about 1/100 and 1/25

of the insulin concentration, respectively (Adeghate et al., 2011; Sorenson et al., 1980). Also, pancreatic polypeptide does not show the Raman peak at 1002 cm^{-1} from phenylalanine (Hilderink et al., 2013). Hence, when detecting insulin in islet secretions using the peak at 1002 cm^{-1} , the influence of other hormones on our measurements can be ignored.

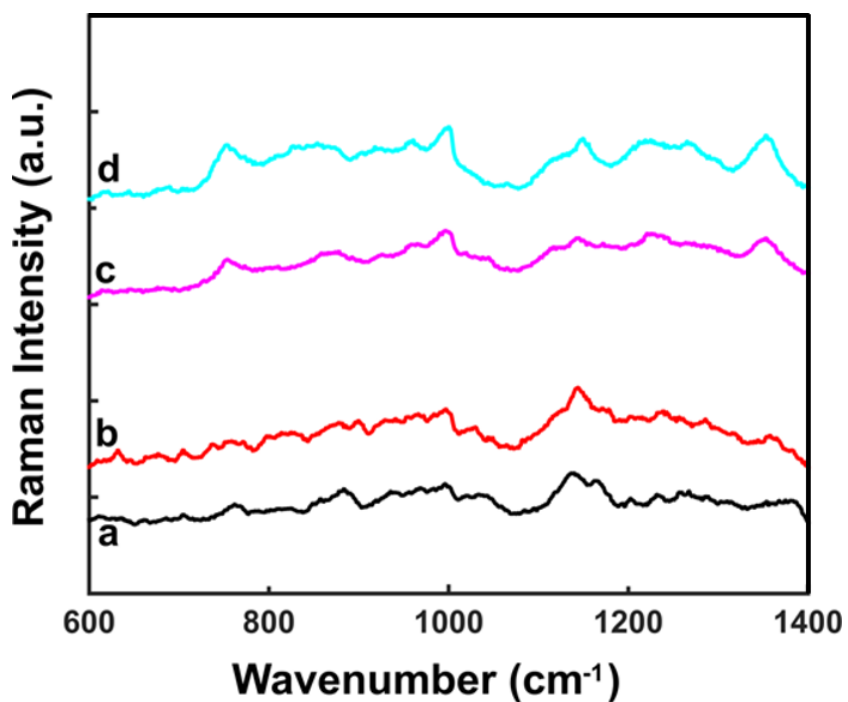


Figure 3.7: Representational SERS spectra obtained from (a) Low glucose buffer (b) High glucose buffer (c) Islet secretions in low glucose buffer with ELISA measured insulin concentration of approximately 138 pM. (d) Islet secretions in high glucose buffer with ELISA measured insulin concentration of approximately 513 pM.

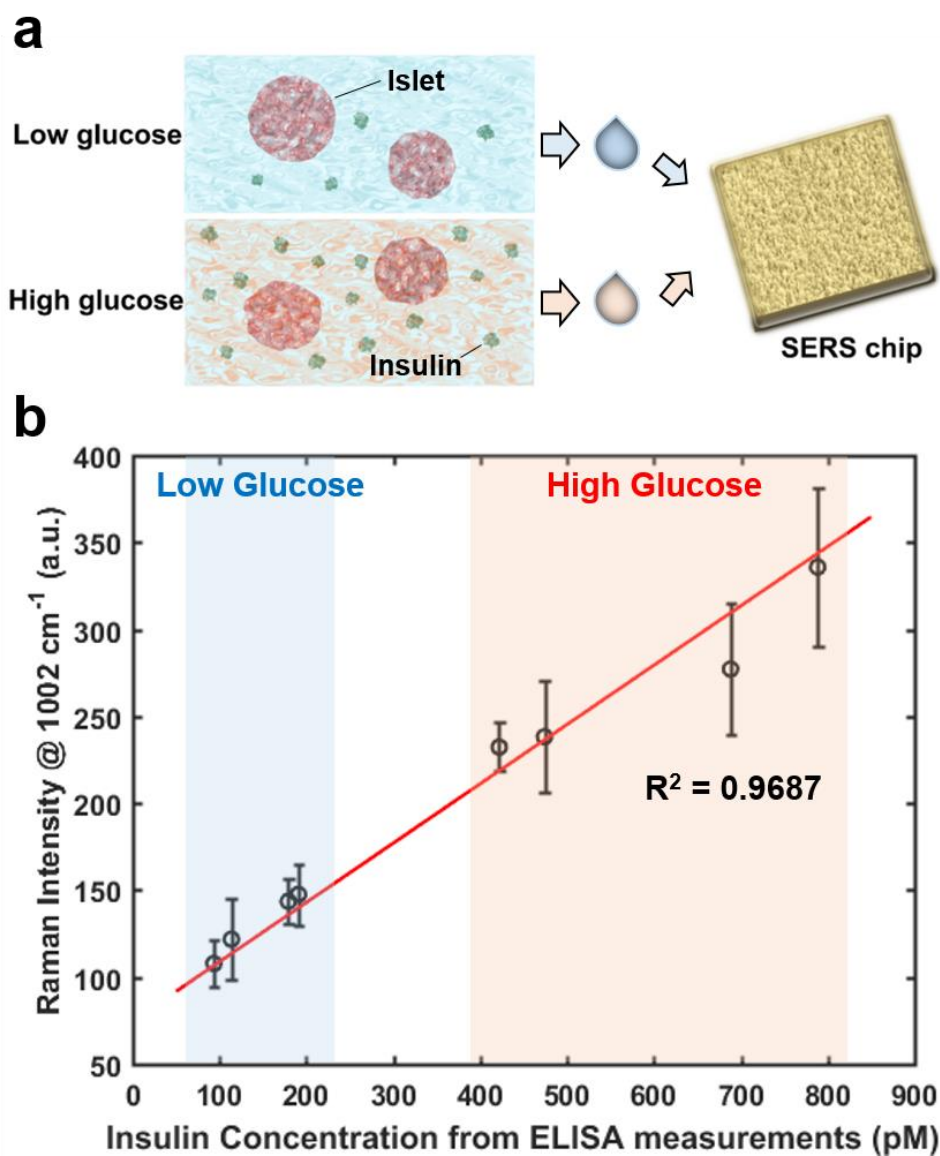


Figure 3.8: Label-free sensor to assess the functionality of human islet secretion. (a) Illustration of using a 3D Au NP SERS chip for analysis of pancreatic islet secretions. Secretions from islets were obtained under low and high glucose conditions. (b) SERS signal intensities measured on various islet secretions (the vertical axis) correlated with the concentrations of insulin in the samples obtained using the ELISA method (the horizontal axis).

3.4. Conclusion

We have demonstrated the optical detection of insulin at physiological concentrations using a highly enhanced plasmonic platform without any external labels such as antibodies. The densely-packed and uniformly distributed hotspots on the 3D Au NP substrate effectively trapped insulin and generated strong Raman emissions. The limit of detection far exceeds previously reported label-free optical sensing-based results and may be further improved using on-chip molecule-concentrating techniques and post-measurement signal processing (Lee et al., 2011; Chang et al., 2016; Masango et al., 2016).

These results have demonstrated the potential of using SERS-based label-free sensing for detecting insulin in various applications including daily monitoring of insulin at home as well as evaluating insulin secretion from pancreatic islets for research purposes in labs and for pre-islet-transplant screening in clinics. These SERS-based biosensors can lead to cost-effective, easy-to-use, and sufficiently accurate insulin sensors, not yet commercially available, for measurements at home, laboratories, and clinics.

References

- Cho, H.; Kumar, S.; Yang, D.; Vaidyanathan, S.; Woo, K.; Garcia, I.; Shue, H. J.; Yoon, Y.; Ferreri, K.; Choo, H. Surface-enhanced Raman spectroscopy-based label-free insulin detection at physiological concentrations for analysis of islet performance. *ACS Sens.* 2018 3 (1), 65-71.
- Seltzer, H. S.; Allen, E. W.; Herron Jr, A. L.; Brennan, M. T. Insulin secretion in response to glycemic stimulus: relation of delayed initial release to carbohydrate intolerance in mild diabetes mellitus. *J. Clin. Invest.* 1967, 46, 323-335.
- Weyer, C.; Bogardus, C.; Mott, D. M.; Pratley, R. E. The natural history of insulin secretory dysfunction and insulin resistance in the pathogenesis of type 2 diabetes mellitus. *J. Clin. Invest.* 1999, 104, 787-794.
- Yalow, R. S.; Berson, S. A. Plasma insulin concentrations in nondiabetic and early diabetic subjects: determinations by a new sensitive immuno-assay technic. *Diabetes* 1960, 9, 254-260.
- Melmed, S.; Polonsky, K. S.; Larsen, P. R.; Kronenberg, H. M. Williams textbook of endocrinology. 12th ed.; Elsevier Saunders: Philadelphia, 2011.
- Shapiro, A. J.; Lakey, J. R.; Ryan, E. A.; Korbitt, G. S.; Toth, E.; Warnock, G. L.; Kneteman, N. M.; Rajotte, R. V. Islet transplantation in seven patients with type 1 diabetes mellitus using a glucocorticoid-free immunosuppressive regimen. *N. Engl. J. Med.* 2000, 343, 230-238.
- Barton, F. B.; Rickels, M. R.; Alejandro, R.; Hering, B. J.; Wease, S.; Naziruddin, B.; Oberholzer, J.; Odorico, J. S.; Garfinkel, M. R.; Levy, M. Improvement in outcomes of clinical islet transplantation: 1999–2010. *Diabetes Care* 2012, 35, 1436-1445.
- Nano, R.; Clissi, B.; Melzi, R.; Calori, G.; Maffi, P.; Antonioli, B.; Marzorati, S.; Aldrighetti, L.; Freschi, M.; Grochowicki, T. Islet isolation for allotransplantation: variables associated with successful islet yield and graft function. *Diabetologia* 2005, 48, 906-912.
- Sweet, I.; Gilbert, M.; Scott, S.; Todorov, I.; Jensen, R.; Nair, I.; Al-Abdullah, I.; Rawson, J.; Kandeel, F.; Ferreri, K. Glucose-stimulated increment in oxygen consumption rate as a standardized test of human islet quality. *Am. J. Transplant.* 2008, 8, 183-192.
- Papas, K. K.; Suszynski, T. M.; Colton, C. K. Islet assessment for transplantation. *Curr. Opin. Organ Transplant.* 2009, 14, 674-682.
- Mork, T. A.; Killeen, C. T.; Patel, N. K.; Dohnal, J. M.; Karydes, H. C.; Leikin, J. B. Massive insulin overdose managed by monitoring daily insulin levels. *Am. J. Ther.* 2011, 18, e162-e166.
- Drachev, V. P.; Thoreson, M. D.; Nashine, V.; Khaliullin, E. N.; Ben-Amotz, D.; Davisson, V. J.; Shalaev, V. M. Adaptive silver films for surface-enhanced Raman spectroscopy of biomolecules. *J. Raman Spectrosc.* 2005, 36, 648-656.
- Keskin, S.; Kahraman, M.; Çulha, M. Differential separation of protein mixtures using convective assembly and label-free detection with surface enhanced Raman scattering. *Chem. Commun.* 2011, 47, 3424-3426.
- Matteini, P.; de Angelis, M.; Ulivi, L.; Centi, S.; Pini, R. Concave gold nanocube assemblies as nanotraps for surface-enhanced Raman scattering-based detection of proteins. *Nanoscale* 2015, 7, 3474-3480.

- Yu, N.-T.; Liu, C.S.; O'Shea, D.C. Laser Raman spectroscopy and the conformation of insulin and proinsulin. *J. Mol. Biol.* 1972, 70(1), 117-132.
- Hilderink, J.; Otto, C.; Slump, C.; Lenferink, A.; Engelse, M.; van Blitterswijk, C.; de Koning, E.; Karperien, M.; van Apeldoorn, A. Label-free detection of insulin and glucagon within human islets of Langerhans using Raman spectroscopy. *PLoS One* 2013, 8, e78148.
- Ortiz, C.; Zhang, D.; Xie, Y.; Davisson, V. J.; Ben-Amotz, D. Identification of insulin variants using Raman spectroscopy. *Anal. Biochem.* 2004, 332, 245-252.
- Blundell, T.; Cutfield, J.; Cutfield, S.; Dodson, E.; Dodson, G.; Hodgkin, D.; Mercola, D. Three-dimensional atomic structure of insulin and its relationship to activity. *Diabetes* 1972, 21, 492-505.
- Kanipe, K. N.; Chidester, P. P.; Stucky, G. D.; Moskovits, M. Large format surface-enhanced Raman spectroscopy substrate optimized for enhancement and uniformity. *ACS Nano* 2016, 10, 7566-7571.
- Lin, D.; Wu, Z.; Li, S.; Zhao, W.; Ma, C.; Wang, J.; Jiang, Z.; Zhong, Z.; Zheng, Y.; Yang, X. Large-area Au-nanoparticle-functionalized Si nanorod arrays for spatially uniform surface-enhanced Raman spectroscopy. *ACS Nano* 2017, 11, 1478-1487.
- Yang, D.; Cho, H.; Koo, S.; Vaidyanathan, S. R.; Woo, K.; Yoon, Y.; Choo, H. Simple, large-scale fabrication of uniform Raman-enhancing substrate with enhancement saturation. *ACS Appl. Mater. Interfaces* 2017, 9, 19092-19101.
- Hoang, P.; Khashab, N. M. Non-resonant large format surface enhanced Raman scattering substrates for selective detection and quantification of xylene isomers. *Chem. Mater.* 2017, 29, 1994-1998.
- Lee, M.; Lee, S.; Lee, J.-h.; Lim, H.-w.; Seong, G. H.; Lee, E. K.; Chang, S.-I.; Oh, C. H.; Choo, J. Highly reproducible immunoassay of cancer markers on a gold-patterned microarray chip using surface-enhanced Raman scattering imaging. *Biosens. Bioelectron.* 2011, 26, 2135-2141.
- Chang, H.; Kang, H.; Ko, E.; Jun, B.-H.; Lee, H.-Y.; Lee, Y.-S.; Jeong, D. H. PSA detection with femtomolar sensitivity and a broad dynamic range using SERS nanoprobes and an area-scanning method. *ACS Sens.* 2016, 1, 645-649.
- Masango, S. S.; Hackler, R. A.; Large, N.; Henry, A.-I.; McAnally, M. O.; Schatz, G. C.; Stair, P. C.; Van Duyne, R. P. High-resolution distance dependence study of surface-enhanced raman scattering enabled by atomic layer deposition. *Nano Lett.* 2016, 16, 4251-4259.
- McCreery, L., R., Raman Spectroscopy for Chemical Analysis. Wiley-Interscience: New York, 2000.
- Shafer-Peltier, K.; Haynes, C.; Glucksberg, M.; Van Duyne, R. Toward a glucose biosensor based on surface-enhanced Raman scattering. *J. Am. Chem. Soc.* 2003, 125, 588-593.
- Alford, F.; Bloom, S.; Nabarro, J. Glucagon levels in normal and diabetic subjects: use of a specific immunoabsorbent for glucagon radioimmunoassay. *Diabetologia* 1977, 13, 1-6.
- Gardner, D.; Shoback, D. Appendix: Normal Hormone Reference Ranges. Greenspan's Basic & Clinical Endocrinology. McGraw-Hill: New York, 2011.
- Adeghate, E.; Kalász, H. Amylin analogues in the treatment of diabetes mellitus: medicinal chemistry and structural basis of its function. *Open Med. Chem. J.* 2011, 5, 78-81.

Sorenson, R. L.; Lindell, D. V.; Elde, R. P. Glucose stimulation of somatostatin and insulin release from the isolated, perfused rat pancreas. *Diabetes* 1980, 29, 747-751.

Part II

Vocal Vibrations-Driven Energy Harvesters

CHARACTERIZATION OF VOCAL VIBRATIONS AS POWER SOURCES

Wearable, portable and implantable electronic devices offer tremendous opportunities to advance various fields such as communication, robotics and health care. However, these devices are limited by energy deficiency in the form of poor battery capacities resulting in weak processing power, frequent recharging need and limited application. Alternative methods for harvesting energy leading to practical and efficient power generators can improve energy supply and enhance lifetime of wearables and implantable biomedical devices such as pacemakers and deep-brain stimulators. In this chapter, we propose and demonstrate that vocal fold vibrations can serve as efficient power sources for wearable electronic products. Our comprehensive numerical and experimental characterization of the vocal fold vibrations identify them as consistent and powerful energy sources.

Part of the work that appears in this chapter was published and is included here with the permissions from the publishers as shown below.

© 2016 IEEE. Reprinted, with permission, from Cho et al., Efficient power generation from vocal folds vibrations for medical electronic implants, 2016 IEEE 29th International Conference on Micro Electro Mechanical Systems (MEMS), 2016.

© 2017 IEEE. Reprinted, with permission, from Cho et al., Powering portable electronics using vocal fold vibrations, 2017 IEEE 30th International Conference on Micro Electro Mechanical Systems (MEMS), 2017.

4.1 Energy Harvesting for Wearable Electronics and Biomedical Implants

Portable and wearable electronics have the potential to massively improve accessibility and provide real-time information in fields such as prosthetics, wearable sensors, implants, and robotics (Kim et al., 2011; Sun et al., 2012; Zeng et al., 2014). Wearable devices labeled as “smart electronics” have been introduced commercially as real-time personal health-

monitors (Figure 4.1) (Düking et al., 2016; Haghi et al., 2017), however they typically require battery packs that need to be charged periodically. While the small form factor of batteries typically employed in wearable electronic devices is an advantage for minimizing device size, it results in significant reduction in battery capacity and limits the processing power of the device (Rawassizadeh et al., 2015; Ostfeld et al., 2012).

In addition, there are a variety of different kinds of biomedical implants under development that require electricity (Figure 4.2). Neurostimulators (Levy et al., 2010; Shah et al., 2010) and cochlear implants are fast growing sectors in the medical industry (Krall and Sharma, 2012; Sandmann et al., 2012). Moreover, implantable neural prostheses also present a great potential in improving the condition of those with physical disabilities (Stieglitz et al., 2005; Gilja et al., 2011). However, all these medical electronic implants must also use batteries, which require periodic replacement. As a result, batteries are often implanted in the chest area, requiring long-running electrical lines through the moving parts of the body such as the neck to power the stimulators in the head, and causing additional reliability issues (Fakhar et al., 2013). These issues in wearable electronics and electrical biomedical implants make energy harvesting from unconventional sources inside the human body an attractive choice that could improve the available power and usage time for such wearable electronic devices.

Energy harvesting techniques derive energy from available sustainable resources such as light, wind or temperature difference to generate electrical energy (Priya et al., 2009; Beeby et al., 2006; Yildiz, 2009). Using an implantable power generator for medical electronics could provide an effective solution to the challenges harvestable energy sources are rare inside the human body. For example, there are no photons inside the body for photoelectric effect. Bodily thermal gradients are too small for practical power generation. A few thermoelectric generators (TEG) have been developed using the temperature difference between the skin and the ambient environment (Leonov, 2013; Kim et al., 2014; Bahk et al., 2015), however the reported power generation is still too low ($< 60 \mu\text{W}/\text{cm}^2$) under ambient condition (Bahk et al., 2015).

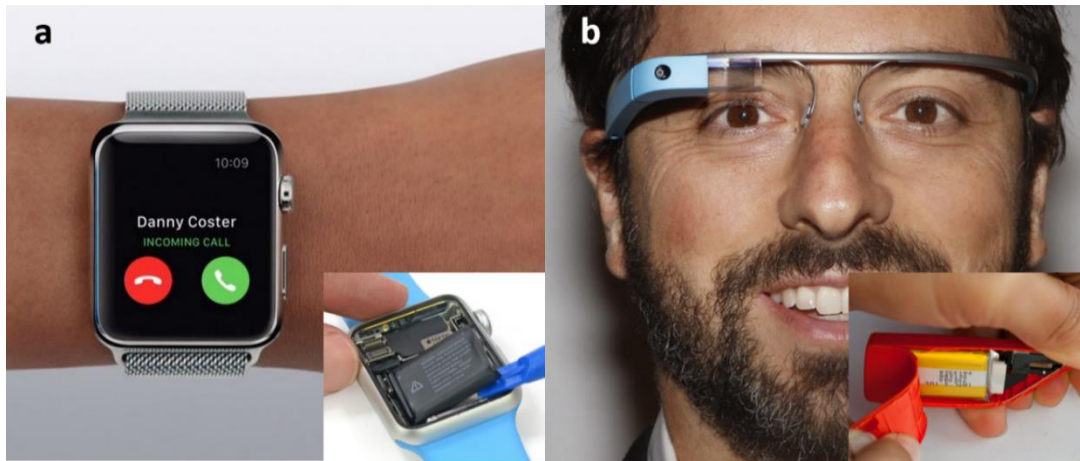


Figure 4.1: Examples of publicly released wearable electronic devices. (a) Apple Watch. Courtesy of Apple Inc. (b) Google Glasses. Courtesy of Google Inc. These devices still have batteries inside the packages (insets).

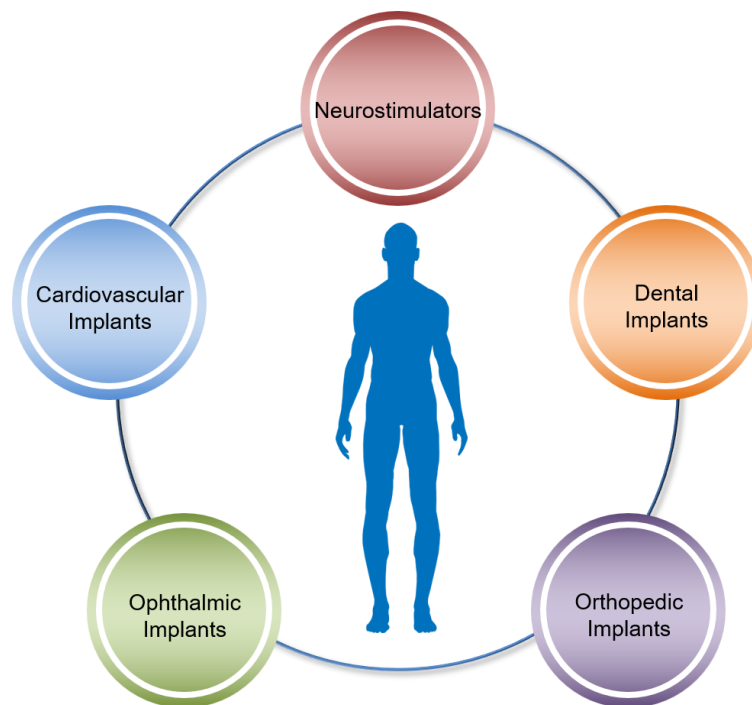


Figure 4.2: Various kinds of biomedical implants which require electricity including neurostimulators, cardiovascular implants, ophthalmic implants, orthopedic implants, and dental implants.

More recently, physiological movement in humans has been targeted as potential source for energy harvesting to charge wearable devices directly and continuously (Mitcheson et al., 2008; Dagdeviren et al., 2017). Physiological motion in humans exists at various scales including small motions such as blood vessel pulsing (Yang et al., 2015; Park et al., 2016), muscle stretching (Chung et al., 2012), skin deformations (Persano et al., 2013; Guido et al., 2016), and organ motions (Mercier et al., 2012; Dagdeviren et al., 2014), or large movements like elbow/knee bending (Lee et al., 2012; Hou et al., 2013; Lee et al., 2015; Yi et al., 2015; Jeong et al., 2015), footsteps (How et al., 2013; Niu et al., 2015; Kang et al., 2015; Jung et al., 2015; Guo et al., 2016), jaw movements (Delnavaz et al., 2014), and hand palm tapping (Niu et al., 2015). Among these movements, the pulsing of vessels can be classified as a periodic deformation whereas the rest are non-periodic with no set frequencies.

Harvesting of electrical energy from these physiological kinetic events has been accomplished using triboelectric (Lee et al., 2012; Hou et al., 2013; Lee et al., 2015; Yi et al., 2015) (transfer of charge), piezoelectric (Yang et al., 2015; Park et al., 2016; Chung et al., 2012; Persano et al., 2013; Guido et al., 2016; Mercier et al., 2012; Dagdeviren et al., 2012) (transfer of vibrational energy), and electromagnetic (Starner and Paradiso, 2004; Saha et al., 2008) (transfer of motion to magnetic generators) transductions. Among these methods, piezoelectric transduction has shown promising results in the conversion of physiological movement of diverse scales to electricity. However, reported trials in this direction still suffer from two major shortcomings. Primarily, electrical energy generated from small human motions mentioned above (current $< 1 \mu\text{A}$, voltage $< 10 \text{ V}$) has so far remained insufficient to charge commonly used battery packs since it is difficult to construct power management circuits that require power below $100 \mu\text{W}$ (Vullers et al., 2012). Secondly, while the large human motions mentioned above could provide strong mechanical vibrations or pressures to energy harvesting devices, the frequencies of these vibrations are either inconsistent (elbow/knee bending, jaw movements, hand palm tapping) or very low ($\leq 5\text{Hz}$). Such frequency unreliability causes difficulties in collecting power due to

inefficient AC/DC converting systems at very low (<100 Hz) or non-resonant frequency (Cheng et al., 2011).

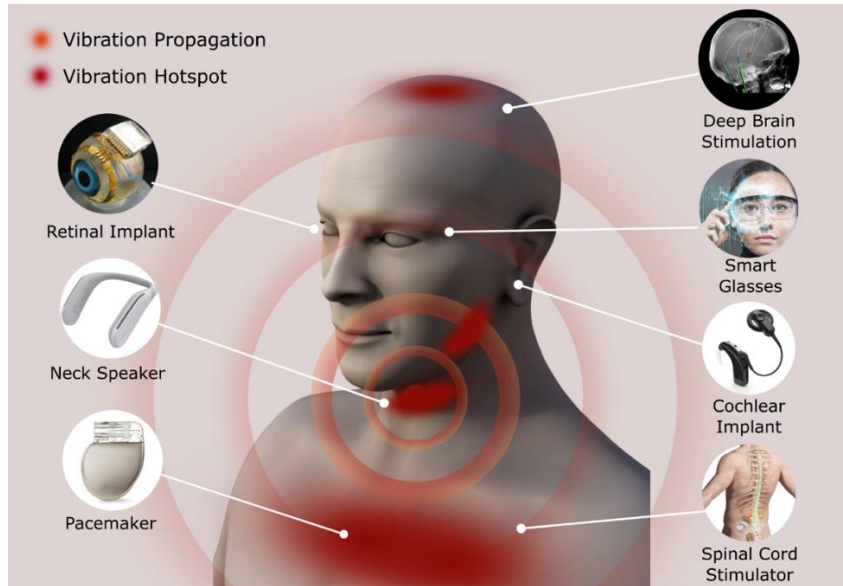


Figure 4.3: Vocal vibrations to harvest energy into wearable devices and biomedical implants.

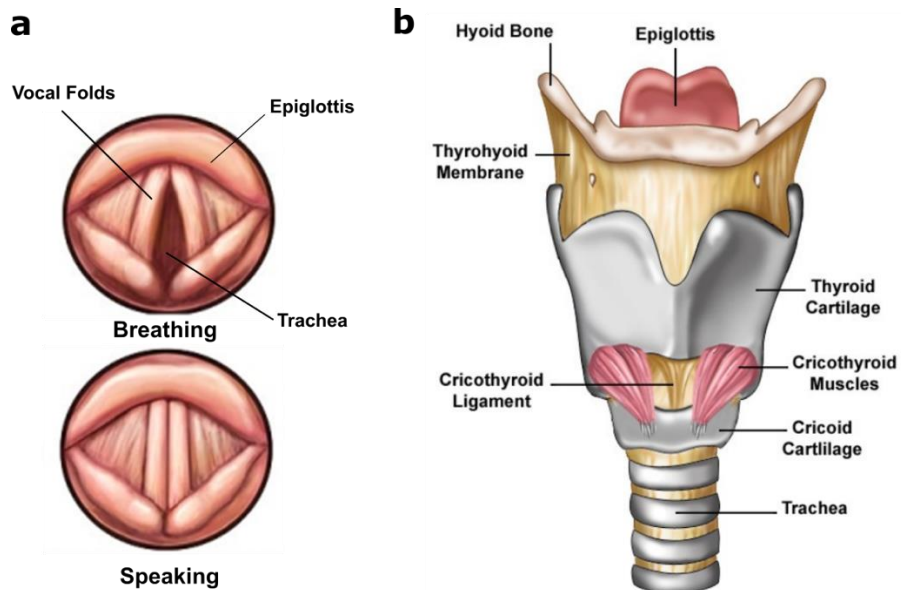


Figure 4.4: Structure of the larynx. (Anatomy of the Larynx, Elena Rizzo Riera, 2008, Trialsight Medical Media). (a) Interior view and (b) exterior view of the larynx.

In Chapters 5-7, vocal fold vibrations, which propagate from the larynx through the air cavities in the human head, are proposed and applied as power sources at various points around the head to drive portable and wearable electronics (Figure 4.2). Human vocal folds can serve as built-in frequency-tunable power sources and excite vibration-driven energy harvesters at their resonances, achieving a high mechanical vibration to electrical energy transduction efficiency. To demonstrate the vocal vibrations as promising power generation sources, we have characterized the energy distribution of vocal vibrations and identified the locations of vibration hotspots on the upper body including head, neck, and chest using multiple accelerometers in this chapter.

4.2 Basic Characterization of Vocal Vibrations

The vocal folds located within the larynx at the top of the trachea vibrate during phonation and modulate the air flow expelled from the lungs. They are composed of two mucous membranes stretched horizontally, from back to front, across the larynx. The way they vibrate is determined by the Bernoulli effect (Figure 4.4a). When the vocal folds are closed, positive air pressure from the lungs forces them open momentarily, but the high velocity air produces a lowered pressure by the Bernoulli effect which brings them back together.

The structure and behavior of vocal folds, laryngeal ligaments and muscles at the larynx are well-studied by physicians and physiologists, and the oscillatory characteristics of vocal fold vibrations have been investigated in sound pathology and audiology (Hollien et al., 1971; Švec and Schutte, 1996; Wittenberg et al., 2000). The vocal folds resonate at a certain frequency which determines individual voice pitch. The muscles of the larynx change the elasticity and tension of the vocal folds to determine the pitch of the sound. Figure 4.4b illustrates how the cricothyroid muscles produce tension and elongation of the vocal folds by drawing up the cricoid cartilage, so that one can tune their voice. The typical frequency range is 80–700 Hz for males and 140-1100 Hz for females. In order to quantify the energy harvesting capability of vocal folds, it is important to analyze whether vocal cords can provide consistent vibrations with sufficient mechanical amplitudes and well-defined frequencies.

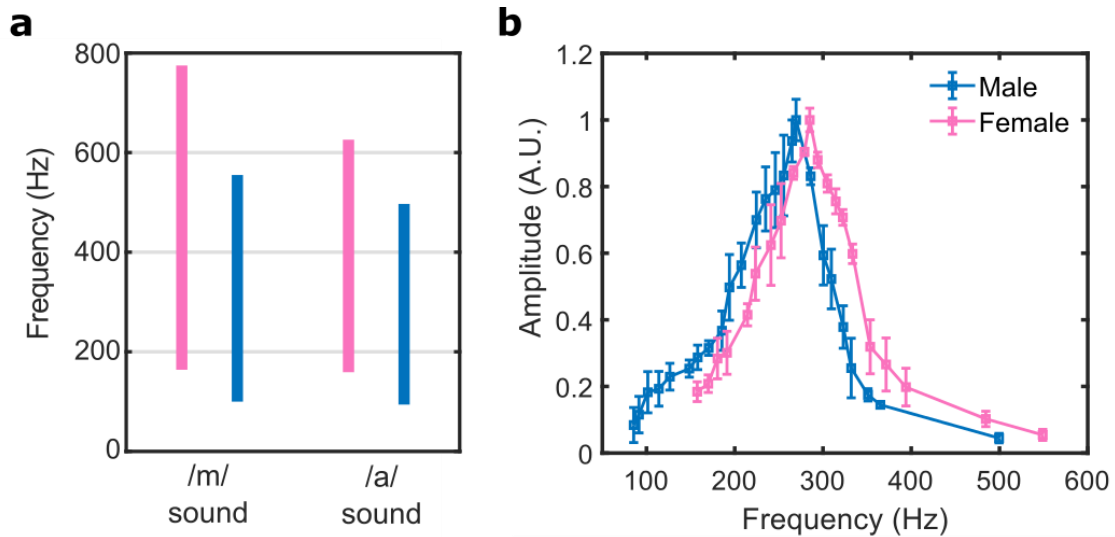


Figure 4.5: Characterization of vocal fold vibrations. (a) Average frequency range of vocal fold vibrations from male and female participants when they make /a/ sounds and /m/ sounds. (b) Amplitudes measured from accelerometers as the target male and female participants changed their vibrations frequencies.

We performed frequency analysis of these vocal vibrations, as well as verification of vibration hotspots around the head, neck, and chest from sample objects of 10 men and 10 women. Analog Devices' ADXL327 was used for the three-axis accelerometer. Accelerometers were attached to spots on the head each time for the frequency measurements at the various locations around the head (Figure 4.11a). In each set of measurements, ultrasonic gel was spread on the surface of the accelerometer to provide a better air-tissue interface and allow the vibrations to transfer better through the skin to the accelerometer. Medical tape was used to tape the accelerometers to the locations on the head. For locations that were covered with hair, the hair was parted such that enough skin was exposed to attach the accelerometer. In each new set of measurements, the accelerometers were removed, cleaned, and reattached to the next locations with a new layer of ultrasonic gel. To analyze the transient voltage signals, we connected accelerometers to a National Instruments' Data Acquisition (DAQ) device, using LabVIEW to gather the appropriate data and convert it to the units we needed. The signals were turned into Fast Fourier Transform in LabVIEW for the frequency analyses.

Participants generated continuous vowel sounds like /m/ sounds and /a/ sounds from their lowest to highest frequencies. The frequency of the vocal vibrations can be affected by the shape of vocal tracts required to emanate the sound (Mermelstein, 1966; Ishizaka and Flanagan, 1972). The path length of a nasal sound such as /m/ is longer than of a predominantly oral sound such as /a/, which results in the /m/ sound being of a lower frequency than the /a/ sound. While men and women typically use 125-175 Hz and 200-250 Hz frequency ranges respectively during speaking (Titze, 1994), they can tune their voices to wider frequency ranges. Figure 4.5(a) shows the tunable frequency range of male's and female's vocal vibrations from our measurements on participants. The frequency range of males when they made the /a/ sound was at 95-555 Hz, while females could tune their voices from 164 Hz to 775 Hz.

Such variation in frequencies can be correlated with variation in sound levels as well as mechanical amplitudes of vocal vibrations. Air cavities around the upper body, where the acoustic waves from the vocal folds propagate through, act like resonators. These air cavities in the upper body such as chest, mouth, nose, and head act like chambers in acoustic instruments, and each cavity is associated with resonating different tones (Titze, 1994). For example, head resonance is used primarily for softer singing and chest resonance adds deeper tone coloring for a tenor (Henrich et al., 2011). To identify the efficient frequency range where large vibrations reside, we characterized relative amplitudes of vibrations from different body parts or frequencies. One individual male and female participant was selected for the rest of the tests. Figure 4.5(b) shows the normalized relationship between electrical amplitudes from the accelerometer and the frequency of the humming-based vocal vibrations of test participants. The strongest vibrations were at 271 Hz and 285 Hz for the male and the female participants, respectively. We used these efficient frequency ranges to set the target frequency of the engineered energy harvesting devices in the next section.

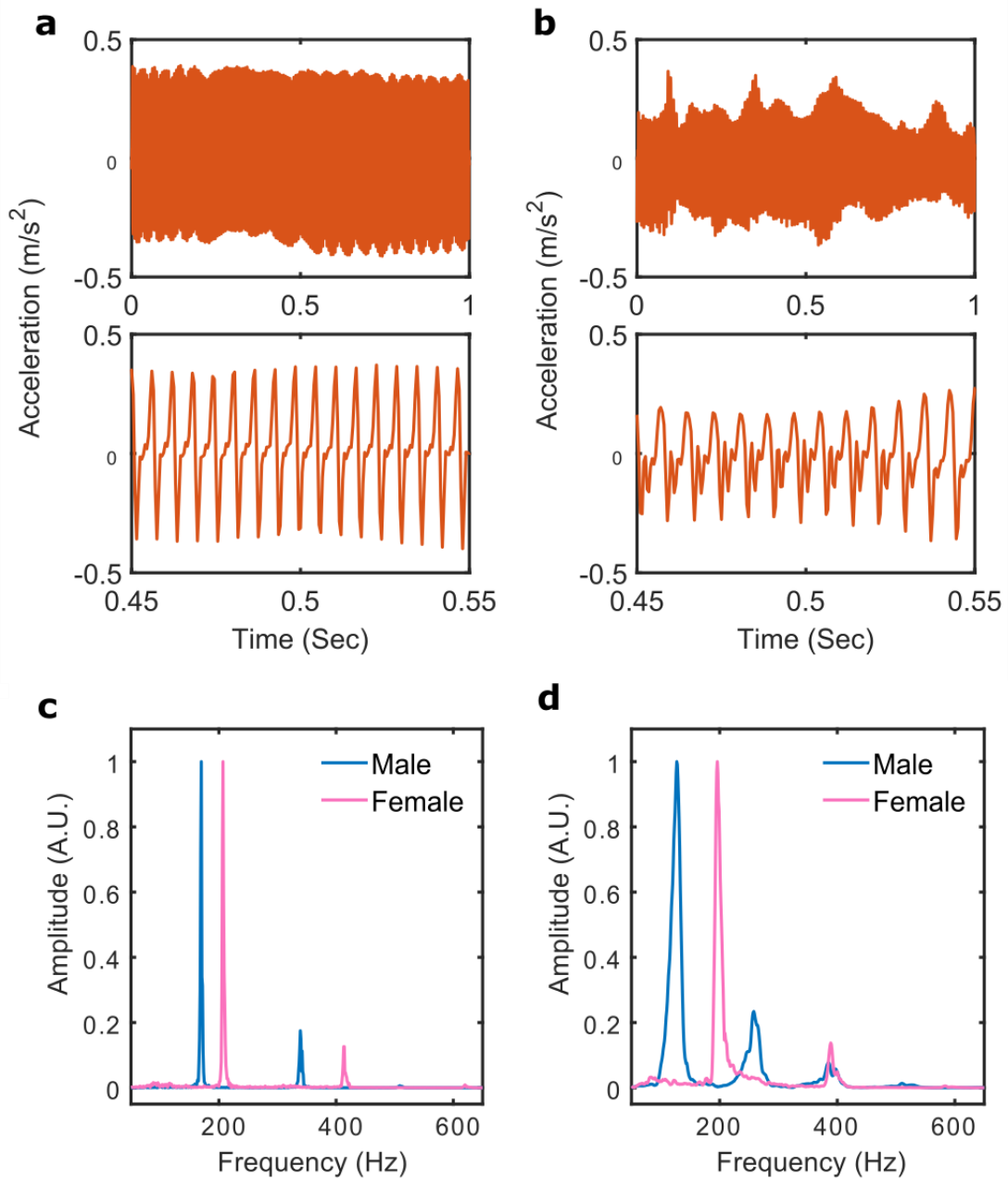


Figure 4.6: Transient output of the acceleration from the accelerometer during humming (a) and reading (b). Normalized frequency responses of the accelerations (along z-axis to the skin) obtained above during humming (c) and reading (d).

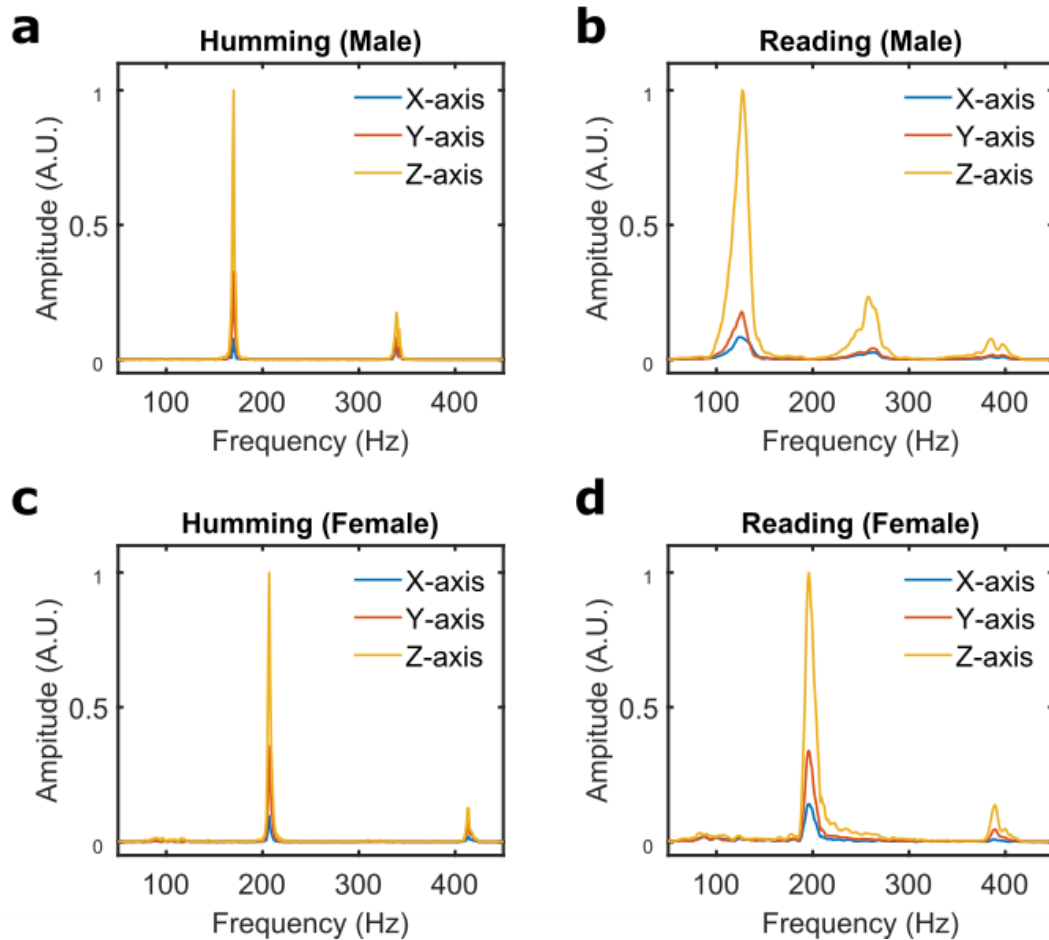


Figure 4.7: Three-axis measurement results using MEMS accelerometers placed on the human larynx while a man was humming (a) and reading (b), and a woman was humming (c) and reading (d). The vibrations along the z-axis is obviously dominant one among three-axis measurement results.

The frequency responses of vocal vibrations from target participants were then measured while humming or reading a simple sentence, with comfortable phonation without intending to change frequency or sound level. The accelerometer measured the amplitudes of vibrations for one second, followed by the fast Fourier transforms of the signal to identify the frequency components. Figure 4.6 shows the transient amplitude signals and corresponding frequency responses of vocal vibrations while humming or reading. With only a few insignificant higher-order harmonics, the acousto-mechanical vibration from humming shows a single dominant peak with 73 ± 4 % of the total energy (Figure 4.6c).

While reading required pronouncing complicated words, which may cause scattering of frequencies, still $63\pm 8\%$ of the vibration energy was still observed at the dominant frequencies (Figure 4.6d). From these measurements, it turns out that the energy source provides very focused vibration energy during phonation including humming and reading.

Also, each mechanical vibration along the x-/y-/z-axis was measured (Figure 4.7). The normal direction to the skin is z-axis, while x-axis indicates the left-right direction and y-axis points the up-down direction. The vibration along z-axis to the skin is dominant among three-axis components for both humming and reading. These characterizations prove that human vocal folds can provide significant unidirectional vibrational energy focused on dominant frequencies for energy harvesting applications.

4.3 Vibration Hotspots Mapping Around Human Upper Body

Next, we identified and mapped out the vibration hotspots around the head and neck area using finite element model simulations of the human head and verified them with mechanical and optical measurement techniques. In order to locate the true vibration hotspots, it is necessary to understand how the vibration propagates throughout the head. The head model simulation was performed to project the route of vibration propagation, followed by acceleration measurements on both human participants and a real head model to verify the principle.

For the simulation of human head model, publicly available full-body CT-scanned images were obtained from the National Biomedical Imaging Archive. Scans with both mouths remained open and closed were obtained for male in order to render the effect of the mouth's position in the propagation of vibration in the human head. These 3D images were imported into the 3D image processing software (ScanIP by Synopsys Inc.) and rendered in 3D (Figure 4.8). These 3D models, which consist of tissues including bone, fat, muscle, brain, and skin, were then segmented into grayscale value depending on tissue material properties. The generated 3D human head models were imported into a commercial finite element simulator (COMSOL Multiphysics®) for vibration simulations. Material properties such as the Young's modulus and the Poisson's ratio of the tissues of our interest

were obtained through literature (Table 4.1). The vibration from the vocal folds was incorporated into the models by prescribing a small displacement at the larynx to demonstrate the vibration of the vocal folds. The acoustic-structure interaction module was used to measure the Von Mises stress on each tissue level. A frequency domain study was performed with frequencies 100, 200 and 300 Hz.

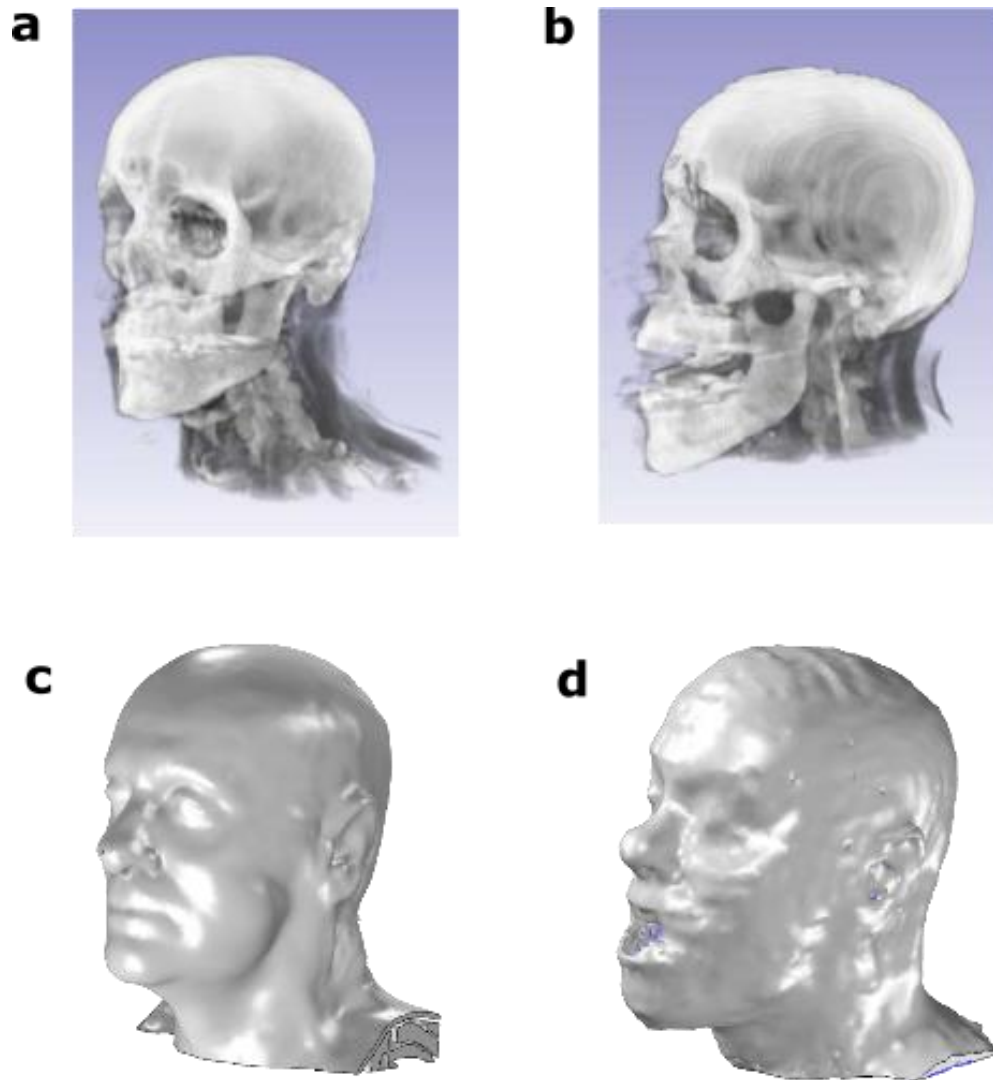


Figure 4.8: Building a 3D human head model for finite element simulation. 3D rendered image from CT scanned images with mouth closed (a) and open (b). Segmented and smoothed 3D head model with mouth closed (c) and open (d).

The mouth of the head model is closed, so the vibration analysis from this simulation reflected the case where a human hums or pronounces the /m/ sound, while the other head model with mouth open represents one who pronounces the /a/ sound. Stress mappings on the head models are shown in Figure 4.9. In case of the head model with the mouth open, an identifiable vibration hotspot does not exist except the location at the larynx. This is because most of the vibration energy reaching the oral cavity is released through the open mouth.

However, the closed mouth model shows several hotspots on the skin and bone around the head, mouth and neck at 100, 200, and 300 Hz (Figure 4.9). The colormap indicates that the neck and jaw area provide stronger vibrations over other areas, which can be due to bone conduction of the vibrations from the larynx. Moreover, the vibration hotspot can also be found at the top of the head. The vibration energy at the oral cavity keep propagating through nasal the cavity and brain cavity, so that the vibration can even reach the top of the head. Thus, while bone conduction is one of the primary methods of vibration propagation, air cavities like nasal cavity and soft tissues such as the tongue and the brain can also be sources of vibration propagation when the mouth is closed, allowing these vibrations to reach the skull.

We further identified these vibrations hotspots around the neck, jaw, and skull using two measurement methods: (a) measuring mechanical vibrations with accelerometers and (b) optical measurements using laser Doppler vibrometer (LDV). Commercially available accelerometers and LDV were used to measure the mechanical vibrations.

Table 4.1: The material properties used in the head model simulation.

	Mass Density [kg/m ³]	Young's Modulus [Pa]	Poisson's Ratio	Speed of Sound [m/s]	Reference
Bone	1810	18E9	0.143	2814	Pal, 2014; Shahar et al., 2010
Brain	1046	9.21E3	0.458	1546	Soza et al., 2005
Fat	911	10.3E3	0.495	1440	Gefen and Haberman, 2007
Muscle	1090	11.5E3	0.3	1588	Collinsworth et al., 2002; Dobrin and Doyle, 1970
Skin	1109	6.25E3	0.48	1624	Pailleur-Mattei et al., 2008; Delalleau et al., 2006

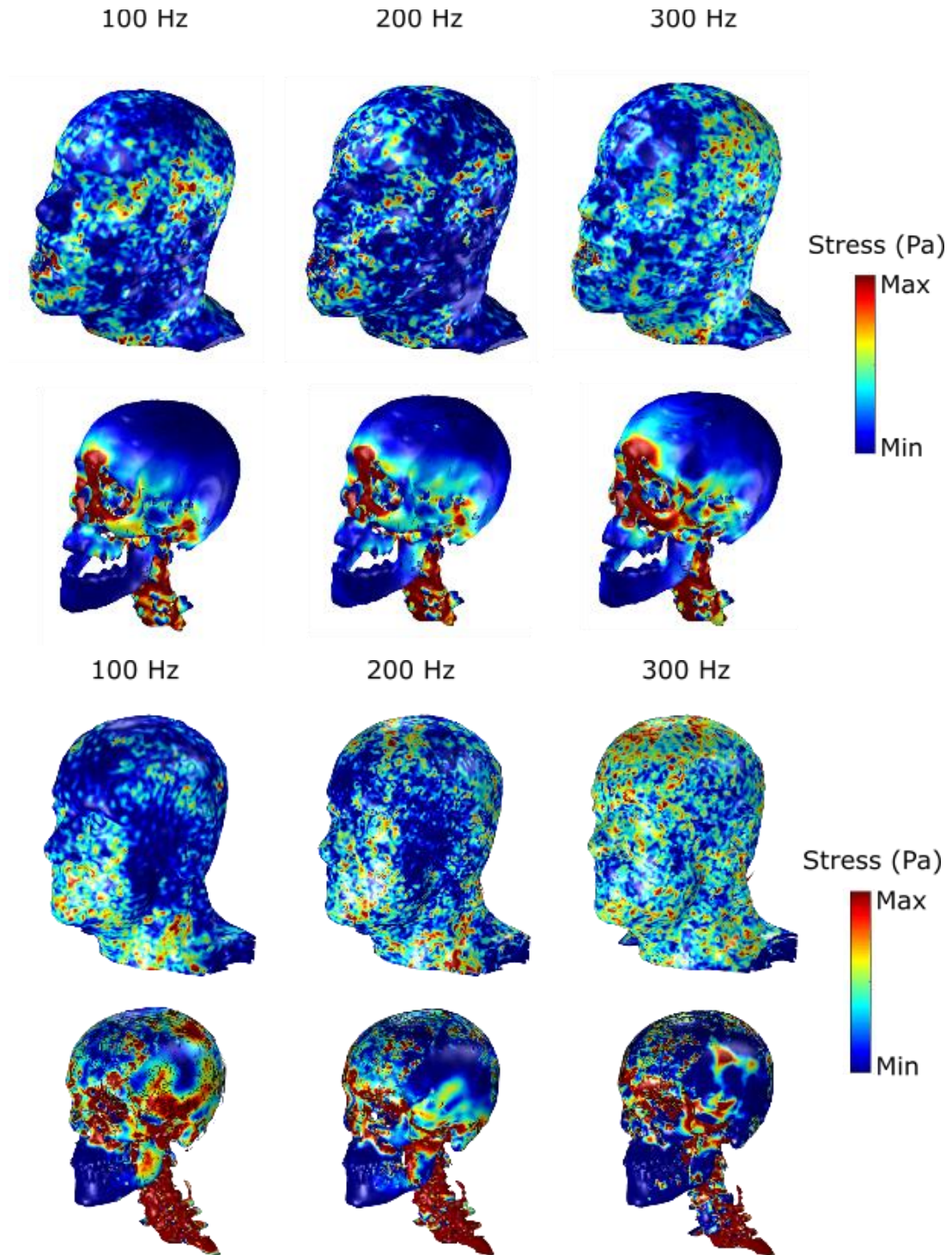


Figure 4.9: Colormaps of stress at frequencies of 100, 200 and 300 Hz on the head model with mouth open (above) and mouth closed (below).

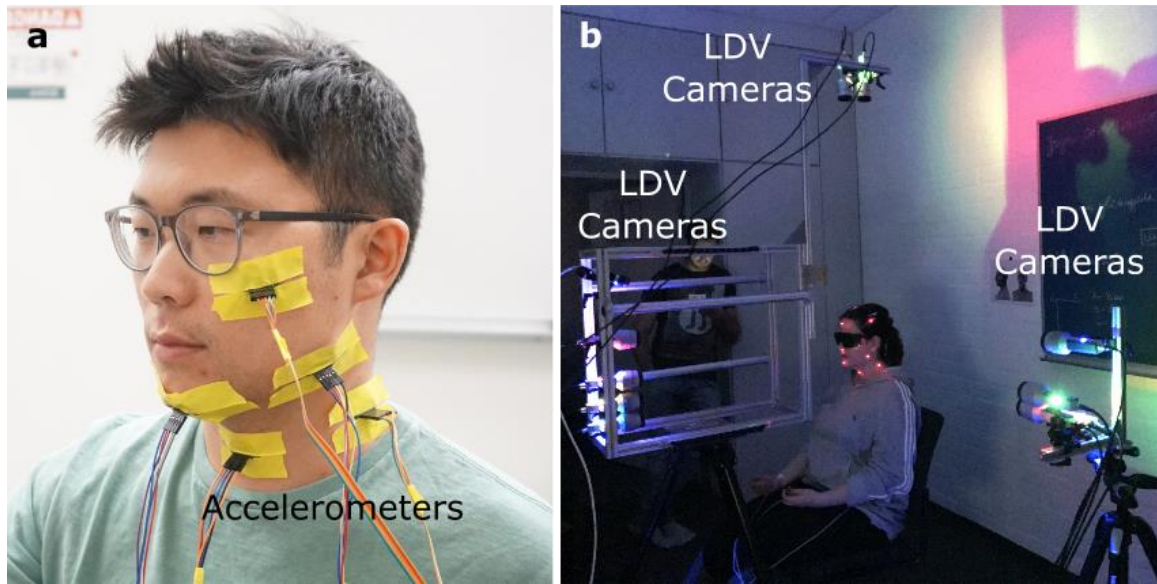


Figure 4.10: Pictures of the vibration hotspots identification around the head. Accelerometer measurements (a) and laser Doppler vibrometer (LDV) measurement (b).

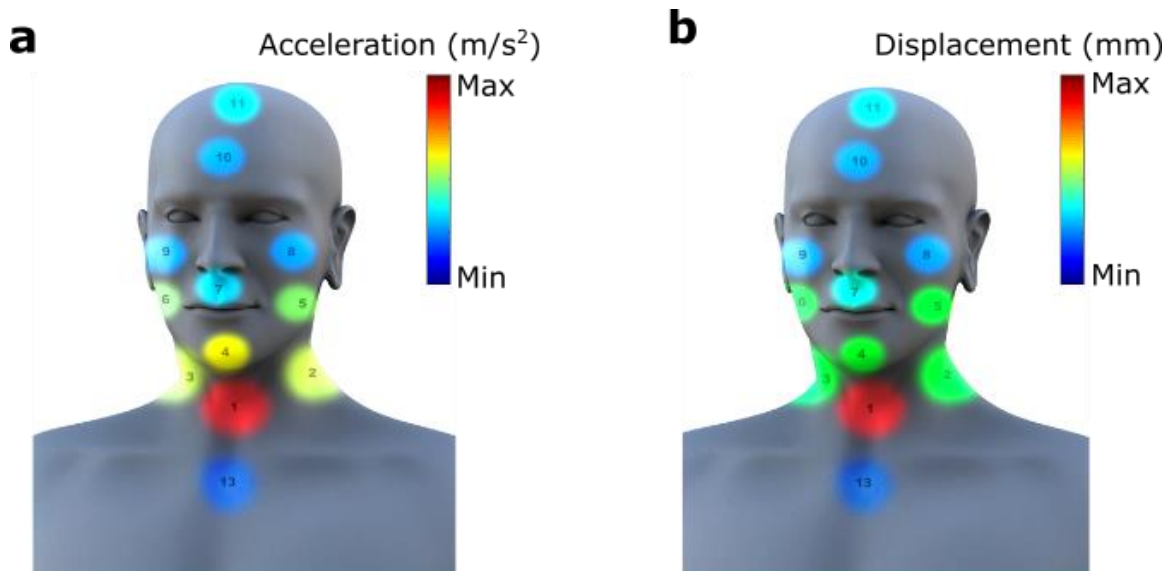


Figure 4.11: Colormap of the vibration hotspots around the head and neck using accelerometers (a) and LDV measurements (b).

For real time comparison among the locations, five accelerometers were attached on five different locations on the upper body at the same time (Figure 4.10a). In order to maintain a consistent vibration amplitude from the vibration source between different measurements, one accelerometer was always kept on the larynx to serve as a reference point while 4 other points were measured simultaneously. The acceleration values from tested locations were calculated using 5-second humming sessions by the participants. The mapping results are shown in Figure 4.10a.

LDV measurements were carried out with our collaborator in TU Clausthal, Germany (Mignanelli and Rembe, 2018). Polytec's MPV-800 multipoint vibrometer was used as time synchronous optical vibrometer with 10 channels. The reflection tape was attached on each test location around the head to enhance the reflected signal from the surface and the 10 cameras were aligned to the surface to get the highest signal. Polytec's MPV software was also used to collect and analyze the signals from all 10 channels. To measure vibration amplitudes around the head using LDV, we used a multipoint vibrometer with 10 channels allowing 10 different locations to be measured simultaneously. We placed ten cameras aligned to different locations around the head (Figure 4.10b) and measured amplitudes of the surface displacements while the participants hummed.

Colormap of the vibration amplitudes from 11 locations around the head can be seen in Figure 4.11. Understandably, the most efficient vibrations exist at the larynx (#1). As shown in the simulation results, the other locations around the neck (#2, #3) and jaw area are also good vibration sources (#5, #6). These other regions provide around 20-40% of the vibration amplitude as compared to the larynx and can serve as potential energy harvesting locations for hearing aids or cochlear implants. Additionally, measurement points at the nasal cavity, at the top of the head through the brain cavity, and at the chest area (#13) can also provide between 10-20% of vibrations as compared to the larynx, which is possible due to propagation of vibrations through the air cavities. The top of the head (#11) could be an appropriate location for the attachment of vocal fold vibration-driven energy harvesters and could deliver the power to implantable devices for deep brain

stimulations. Similarly, the chest area can be a good candidate for vocal fold vibration-driven recharging of a pacemaker battery.

Table 4.2: Power requirements to operate various biomedical electronic implants.

Device	Power	Adjacent Vibration Source
Biomonitoring System	< 100 μ W	
Pacemaker	< 100 μ W	Chest (#13)
Cochlear Processor	200 μ W	Jaw or sides of neck (#2, #3, #5, #6)
Hearing Aid	100-2000 μ W	Jaw or sides of neck (#2, #3, #5, #6)
Deep Brain Simulation	1-3 mW per electrode	Top of the head

Table 4.2 shows the list of possible biomedical electronic implants whose batteries could possibly be recharged by energy harvesting methods using vocal vibrations. The adjacent vibration hotspots are also mentioned such as chest, jaw, sides of neck, and the top of the head. The required powers were compiled from the literature (Rasouli et al., 2010).

4.4 Conclusion

In this chapter, we have demonstrated an energy harvesting device which utilizes vocal fold vibrations generated during “humming” or “speaking” for powering wearable electronics. We identified frequency analyses of vocal vibrations with male and female participants and verified vocal vibration-based energy harvesting “hotspots” on the human upper body through simulations as well as experimental verification by measuring acceleration and displacement.

References

- Kim, D. H.; Lu, N.; Ma, R.; Kim, Y. -S.; Kim, R. -H.; Wang, S.; Wu, J. et al. Epidermal electronics. *Science* 1997, 333, 838-843.
- Sun, J. -Y.; Zhao, X.; Illeperuma, W. R. K.; Chaudhuri, O.; Oh, K. H.; Mooney, D. J.; Vlassak, J. J.; Suo Z. Highly stretchable and tough hydrogels. *Nature* 2012 489, 133-136.
- Zeng, W.; Shu, L.; Li, Q.; Chen, S.; Wang, F.; Tao, X. M. Fiber-based wearable electronics: a review of materials, fabrication, devices, and applications. *Adv. Mater.* 2014, 26, 5310-5336.
- Düking, P.; Hotho, A.; Holmberg, H.C.; Fuss, F. K.; Sperlich, B. Comparison of non-invasive individual monitoring of the training and health of athletes with commercially available wearable technologies. *Front. Physiol.* 2016, 7, 71.
- Haghi, M.; Thurow, K.; Stoll, R. Wearable devices in medical internet of things: scientific research and commercially available devices. *Healthc. Inform. Res.* 2017, 23 (1), 4-15.
- Rawassizadeh, R.; Tomitsch, M.; Nourizadeh, M.; Momeni, E.; Peery, A.; Ulanova, L.; Pazzani, M. Energy-efficient integration of continuous context sensing and prediction into smartwatches. *Sensors* 2015, 15, 22616-22645.
- Ostfeld, A.E.; Gaikwad, A.M.; Khan, Y.; Arias, A.C., High-performance flexible energy storage and harvesting system for wearable electronics. *Sci. Rep.* 2016, 6(26122).
- Levy, R.; Deer, T. R.; Henderson, J. Intracranial neurostimulation for pain control: a review. *Pain Physician* 2010, 13, 157-165.
- Shah, R. S.; Chang, S.-Y.; Min, H.-K.; Cho, Z.-H.; Blaha, C. D.; Lee, K. H. Deep brain stimulation: technology at the cutting edge. *J. Clin. Neurol.* 2010, 6, 167-182.
- Kral1, A.; Sharma, A., Developmental neuroplasticity after cochlear implantation. *Trends in Neurosciences.* 2012, 35, 2, 111-122.
- Sandmann, P.; Dillier, N.; Eichele, T.; Meyer, M.; Kegel, A.; Pascual-Marqui, R. D.; Marcar, V. L.; Jäncke, L.; Debener, S. Visual activation of auditory cortex reflects maladaptive plasticity in cochlear implant users. *Brain* 2012, 135, 555-568.
- Stieglitz, T.; Schuettler, M.; Koch, K. P. Implantable biomedical microsystems for neural prostheses. *IEEE Eng. Med. Biol. Magn.* 2005, 24, 58-65.
- Gilja, V.; Chestek, C. A.; Diester, I.; Henderson, J. M.; Deisseroth, K.; Shenoy, K. V. Challenges and opportunities for next-generation intracortically based neural prostheses. *IEEE Trans. Biomed. Eng.* 2011, 58, 7, 1891-1899.
- Fakhar, K.; Hastings, E.; Butson, C. R.; Foote, K. D.; Zeilman, P.; Okun, M. S. Management of deep brain stimulator battery failure: battery estimators, charge density, and importance of clinical symptoms. *PLoS One* 2013, 8, 3, e58665.
- Priya, S.; Inman, D. J., Energy Harvesting Technologies, New York: Springer US.
- Beeby, S. P.; Tudor, M. J.; White, N. M. Energy harvesting vibration sources for microsystems applications. *Meas. Sci. Technol.* 2006, 17(12), R175.
- Yildiz, F. Potential ambient energy-harvesting sources and techniques. *Journal of Technology Studies* 2009, 35(1), 40-48.
- Leonov, V. Thermoelectric energy harvesting of human body heat for wearable sensors. *IEEE Sens. J.* 2013 13(6), 2284-2291.

- Kim, S. J.; We J. H.; Cho, B. J. A wearable thermoelectric generator fabricated on a glass fabric. *Energy Environ. Sci.* 2014, 7, 1959-1965.
- Bahk, J. -H.; Fang, H.; Yazawaa, K.; Shakouria, A. Flexible thermoelectric materials and device optimization for wearable energy harvesting. *J. Mater. Chem. C* 2015, 3, 10362-10374.
- Mitcheson, P. D.; Yeatman, E. M.; Rao, G. K.; Holmes, A. S.; Green, T. C. Energy harvesting from human and machine motion for wireless electronic devices. *Proc. IEEE* 2008, 96(9), 1457-1486.
- Dagdeviren, C.; Li, Z.; Wang, Z. L. Energy harvesting from the animal/human body for self-powered electronics. *Annu. Rev. Biomed. Eng.* 2017, 19, 85-108.
- Yang, J.; Chen, J.; Su, Y.; Jing, Q.; Li, Z.; Li, F.; Wen, X.; Wang, Z.; Wang, Z.L. Eardrum-inspired active sensors for self-powered cardiovascular system characterization and throat-attached anti-interference voice recognition. *Adv. Mater.* 2015, 27(8), 1316-1326.
- Park, S. H.; Lee, H. B.; Yeon, S. M.; Park, J.; Lee, N. K. Flexible and stretchable piezoelectric sensor with thickness-tunable configuration of electrospun nanofiber mat and elastomeric substrates. *ACS Appl. Mater. Interfaces.* 2016, 8(37), 24773-24781.
- Chung, S.Y.; Kim, S.; Lee, J.-H.; Kim, K.; Kim, S.-W.; Kang, C.-Y.; Yoon, S.-J.; Kim, Y.S. All-solution-processed flexible thin film piezoelectric nanogenerator. *Adv. Mater.* 2012, 24(45), 6022-6027.
- Persano, L.; Dagdeviren, C.; Su, Y.; Zhang, Y.; Girardo, S.; Pisignano, D.; Huang, Y.; Rogers, J.A. High performance piezoelectric devices based on aligned arrays of nanofibers of poly(vinylidene fluoride-co-trifluoroethylene). *Nature Comm.* 2013, 4, 1633.
- Guido, F.; Quattieri, A.; Algieri, L.; Lemma, E.D.; Vittoio, M.D.; Todaro, M.T., AlN-based flexible piezoelectric skin for energy harvesting from human motion. *Microelectron. Eng.* 2016, 159(15) 174-178.
- Mercier, P. P.; Lysaght, A. C.; Bandyopadhyay, S.; Chandrakasan, A. P.; Stankovic, K. M. Energy extraction from the biologic battery in the inner ear. *Nat. Biotech.* 2012, 30(12), 1240.
- Dagdeviren, C.; Yang, B. D.; Su, Y.; Tran, P. L.; Joe, P.; Anderson, E. et al. Conformal piezoelectric energy harvesting and storage from motions of the heart, lung, and diaphragm. *Proc. Natl. Acad. Sci. U.S.A.* 2014, 111(5), 1927-1932.
- Lee, M.; Chen, C.-Y.; Wang, S.; Cha, S.N.; Park, Y.J.; Kim, J.M.; Chou, L.-J.; Wang, Z.L. A Hybrid piezoelectric structure for wearable nanogenerators. *Adv. Mater.* 2012, 24(13) 1759-1764.
- Hou, T.-C.; Yang, Y.; Zhang, H.; Chen, J.; Chen, L.-J.; Wang, Z.L. Triboelectric nanogenerator built inside shoe insole for harvesting walking energy, *Nano Energy* 2013, 2(5), 856-862.
- Lee, S.; Ko, W.; Oh, Y.; Lee, J.; Baek, G.; Lee, Y.; Sohn, J.; Cha, S.; Kim, J.; Park, J.; Hong, J. Triboelectric energy harvester based on wearable textile platforms employing various surface morphologies, *Nano Energy* 2015, 12, 410-418.
- Yi, F.; Niu, S.; Yang, P.K.; Wang, Z.; Chen, J.; Zhou, Y.; Zi, Y.; Wang, J.; Liao, Q.; Zhang, Y.; Wang, Z.L., A hyper-stretchable elastic-composite energy harvester. *Adv. Func. Mater.* 2015, 25(24), 3688-3696.

- Jeong, C.K.; Lee, J.; Han, S.; Ryu, J.; Hwang, G.-T.; Park, D.Y.; Park, J.H.; Lee, S.S.; Byun, M.; Ko, S.H.; Lee, K.J. A hyper-stretchable elastic-composite energy harvester. *Adv. Mater.* 2015, 27(18), 2866-2875.
- How, T.-C.; Yang, Y.; Zhang, H.; Chen, J.; Chen, L.-J.; Wang, Z.L. Triboelectric nanogenerator built inside shoe insole for harvesting walking energy. *Nano Energy* 2013, 2(5), 856-862.
- Niu, S.; Wang, X.; Yi, F.; Zhou, Y.S.; Wang, Z.L. A universal self-charging system driven by random biomechanical energy for sustainable operation of mobile electronics. *Nat. Comm.* 2012, 6, 8975.
- Kang, Y.; Wang, B.; Dai, S.; Liu, G.; Pu, Y.; Hu, C. Folded elastic strip-based triboelectric nanogenerator for harvesting human motion energy for multiple applications. *Appl. Mater. Inter.* 2015, 7(36), 20469-20476.
- Jung, W.-S.; Lee, M.-J.; Kang, M.-G.; Moon, H.G.; Yoon, S.-J.; Baek, S.-H.; Kang, C.-Y. Powerful curved piezoelectric generator for wearable applications. *Nano Energy* 2015, 13, 174-181.
- Guo, H.; Yeh, M.-H.; Lai, Y.-C.; Zi, Y.; Wu, C.; Wen, Z.; Hu, C.; Wang, Z.L. All-in-one shape-adaptive self-charging power package for wearable electronics. *ACS Nano* 2016, 10, pp 10580-10588.
- Delnavaz, A.; Voix, J. Flexible piezoelectric energy harvesting from jaw movements. *Smart Mater. Struct.* 2014, 23(10).
- Starner, T.; Paradiso, J. A. (2004). Human generated power for mobile electronics. Low Power Electronics Design Ed. C Piguat (Boca Raton, FL: CRC Press)
- Saha, C.R.; O'Donnell, T.; Wang, N.; McCloskey, P. Electromagnetic generator for harvesting energy from human motion. *Sensor. Actuat. A-Phys.* 2008, 147, 248-253.
- Vullers R.J.M.; van Schaijk R.; Doms I.; Van Hoof C.; Mertens R. Micropower energy harvesting. *Solid State Electron.* 2009, 53, 684-693.
- Cheng S.; Jin Y.; Rao Y.; Arnold D.P. An active voltage doubling AC/DC converter for low energy harvesting applications. *IEEE Trans. Power Elect.* 2011, 26(8), 2258-2265.
- Hollien, H.; Dew, D.; Philips, P. Phonational Frequency Ranges of Adults. *J. Speech Lang. Hear. Res.* 1971, 14(4), 755-760.
- Švec, J.G.; Schutte H.K. Videokymography: High-speed line scanning of vocal fold vibration. *J. Voice* 1996, 10(2), 201-205.
- Wittenberg T.; Tigges M.; Mergell P.; Eysholdt U. Functional imaging of vocal fold vibration: Digital muticlise high-speed kymography. *J. Voice* 2005, 14(3), 422-442.
- Mermelstein P. Determination of the vocal-tract shape from measured formant frequencies. *J. Acoust. Soc. Am.* 1966, 41, 1283.
- Ishizaka K.; Flanagan J.L. Synthesis of voiced sounds from a two-mass model of the vocal cords. *Bell Syst. Tech. J.* 1972, 51(6), 1233-1268.
- Titze, I. R. (1994). Principles of Voice Production (Prentice-Hall, Englewood Cliffs, NJ)
- Henrich N.; Smith J.; Wolfe J. Vocal tract resonance in singing: Strategies used by sopranos, altos, tenors, and bartones. *J. Acoust. Soc. Am.* 2011, 129 (2), 1024-1035.
- Pal, S. Design of Artificial Human Joints & Organs, Ed. Boston, MA: Springer, 2014, pp. 23-40.

- Soza, G.; Grosso, R.; Nimsy, C.; Hastreiter, P.; Fahlbusch, R.; Greiner, G. Determination of the elasticity parameters of brain tissue with combined simulation and registration. *Int. J. Med. Robot.* 2005, 1, 87-95.
- Gefen, A.; Haberman, E. Viscoelastic properties of ovine adipose tissue covering the gluteus muscles. *J. Biomech. Eng.* 2007, 129, 924-30.
- Collinsworth, A. M.; Zhang, S.; Kraus, W. E.; Truskey, G. A. Apparent elastic modulus and hysteresis of skeletal muscle cells throughout differentiation. *Am. J. Physiol. Cell Physiol.* 2002, 283, C1219-27.
- Dobrin P. B.; Doyle, J. M. Vascular smooth muscle and the anisotropy of dog carotid artery, *Circ. Res.* 1970, 27, 105-19.
- Pailler-Mattei, C.; Bec, S.; Zahouani, H. In vivo measurements of the elastic mechanical properties of human skin by indentation tests. *Med. Eng. Phys.* 2008, 30, 599-606.
- Delalleau, A.; Josse, G.; Lagarde, J. M.; Zahouani, H.; Bergheau, J. M. Characterization of the mechanical properties of skin by inverse analysis combined with the indentation test, *J. Biomech.* 2006, 39, 1603-10.
- Mignanelli, L.; Rembe, C. Uncertainty contribution of the laser-beam orientation for laser Doppler vibrometer measurements at the carotid artery. *Journal of Physics: Conference Series*, 2018, Volume 1149, conference 1.
- Rasouli, M.; Phee L. S. Energy sources and their development for application in medical devices. *Expert Rev. Med. Devices* 2010, 7(5), 693-709.

POWER GENERATION USING VOCAL VIBRATIONS

Based on the promising results obtained in chapter 5 of potential energy harvesting of vocal fold vibrations, in this chapter I will present the successful development of the vocal fold vibration harvesting device. Using this device, we were able to generate 3.99 mW of electrical power from the acousto-mechanical vibrations originating from the human vocal folds and successfully charged a 15-mAh lithium polymer battery. These results indicate that vocal fold vibrations can be an extremely efficient energy source for portable and wearable electronics leading to significant improvement in device performance.

Part of this work that appears in this chapter was published and is included here with the permission from the publisher as shown below.

© 2017 IEEE. Reprinted, with permission, from Cho et al., Powering portable electronics using vocal fold vibrations, 2017 IEEE 30th International Conference on Micro Electro Mechanical Systems (MEMS), 2017.

5.1 Piezoelectric Energy Harvester and Energy Harvesting Array

There are three basic energy conversion mechanisms that convert vibration into electric energy. These three methods are electromagnetic, electrostatic, and piezoelectric conversions (Williams and Yates, 1996; Erturk and Inman, 2011). Among these methods, piezoelectric transduction has shown promising results in conversion of physiological movement of diverse scales to electricity (Yang et al., 2015; Park et al., 2016; Chung et al., 2012; Persano et al., 2013; Guido et al., 2016; Mercier et al., 2012; Dagdeviren et al., 2014). The main advantages in energy harvesting using piezoelectric devices are their large power densities of piezoelectric materials and ease of application (Erturk and Inman, 2011).

We have developed energy harvesting devices using a piezoelectric generator which is based on the piezoelectric effect. The piezoelectric energy harvesting method was chosen to take advantages of focused vibrational energy with one direction at dominant frequencies from vocal vibrations. For piezoelectric material, we chose lead zirconate titanate (PZT), the most popular piezoceramic material which has the strongest electromechanical coupling coefficient (Sodano et al., 2005). Particularly, PZT-5A was the material used which is the most widely implemented piezoceramic material (Sodano et al., 2004).

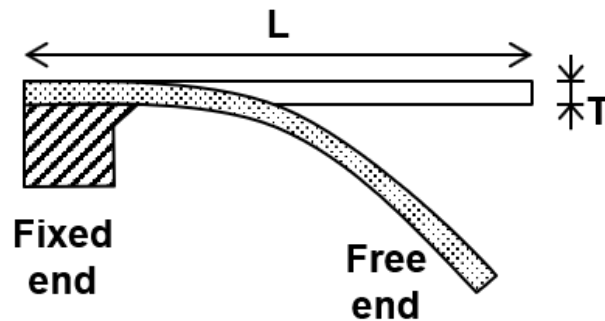


Figure 5.1: Schematic of piezoelectric cantilever beam. The beam length (L) and thickness (T) determine the resonance frequency of the beam.

For the unit device structure, a bimorph cantilever beam (510 μm thick) was used (Figure 5.1). The length of the cantilever beam was determined to achieve resonance conditions at the desired frequency. As discussed earlier (Figure 4.5b), the mechanical amplitudes of the vocal vibrations while humming was highest in the 260-285 Hz range for the target participants. Basically, natural frequency (f_n) of the cantilever beam is determined by material properties and dimensional parameters. f_n decreases with increasing the cantilever mass (m) using the spring-mass system equation:

$$\omega_n = \sqrt{\frac{k}{m}} \quad (5.1)$$

where $\omega_n = 2\pi f$ and k is the spring stiffness. This equation (6.1) can also be expressed as

$$\omega_n = \alpha_n^2 \sqrt{\frac{EI}{mL^4}} \quad (5.2)$$

where E is the modulus of rigidity of the cantilever material, I is the moment of inertia of the cantilever cross-section, and α_n can be solved as shown in the table below.

Table 5.1: Solutions for α_n in Equation 5.2.

n	1	2	3	4	5	6
α_n	1.875	4.694	7.855	10.996	14.137	17.279

Each vibrational mode shape of cantilever beam is shown in Figure 5.2. The mode shapes were achieved using finite element simulation with COMSOL Multiphysics.

The piezoelectric material properties such as Young's modulus, density and dimensional parameters including beam length and thickness determine the resonance frequencies of the cantilever beams. Our simulations were done using PZT-5A material to find the proper beam length. Figure 5.3a shows resonance frequencies obtained from simulations with varying both the lengths and the thicknesses of the beam. Through this result, the desired beam length for resonance in the target frequency range (260-285 Hz) is found to be 28 mm (276 Hz of resonance frequency expected) when the thickness of the beam is 0.51 μm . Using these parameters, 1 V of electrical voltage is expected to be generated from the simulation (Figure 5.3b).

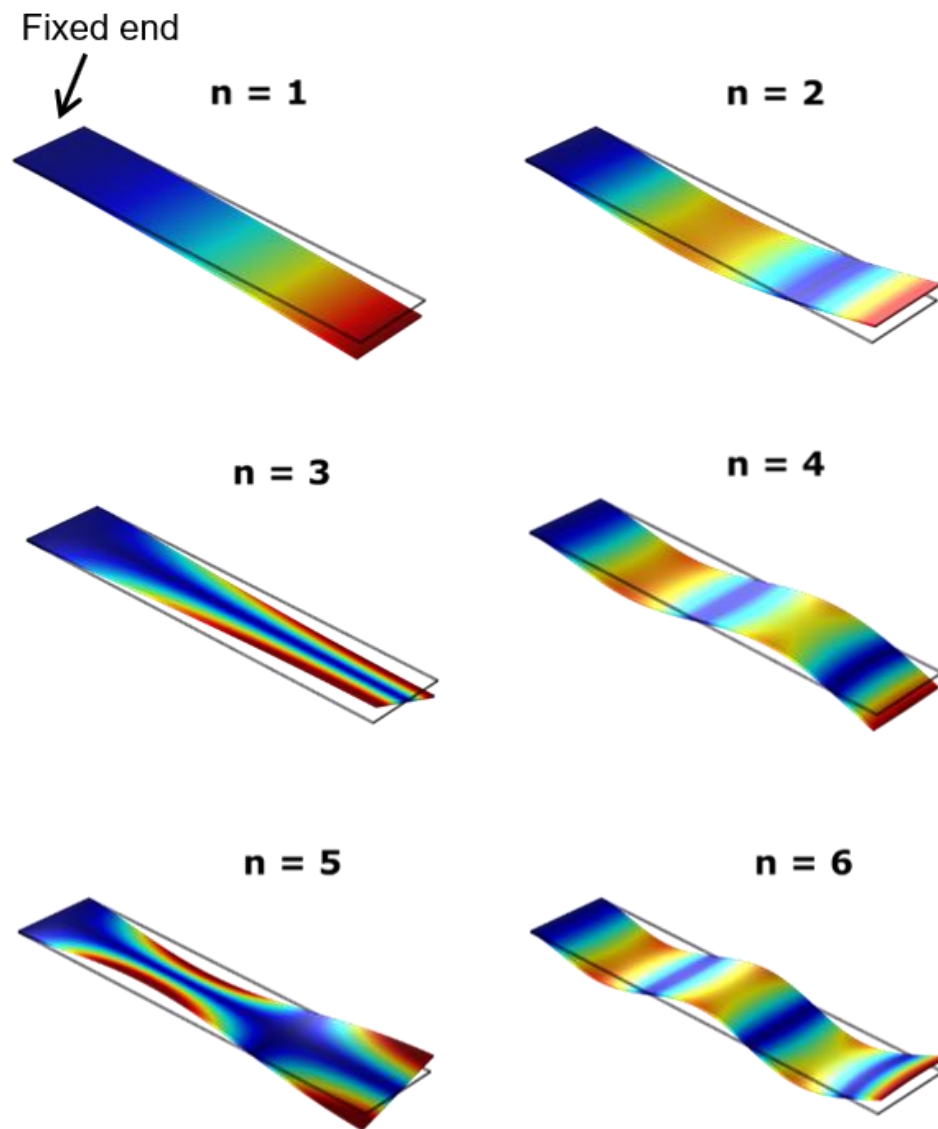


Figure 5.2: Mode shapes of cantilever beam when $n = 1, 2, \dots, 6$ in α_n .

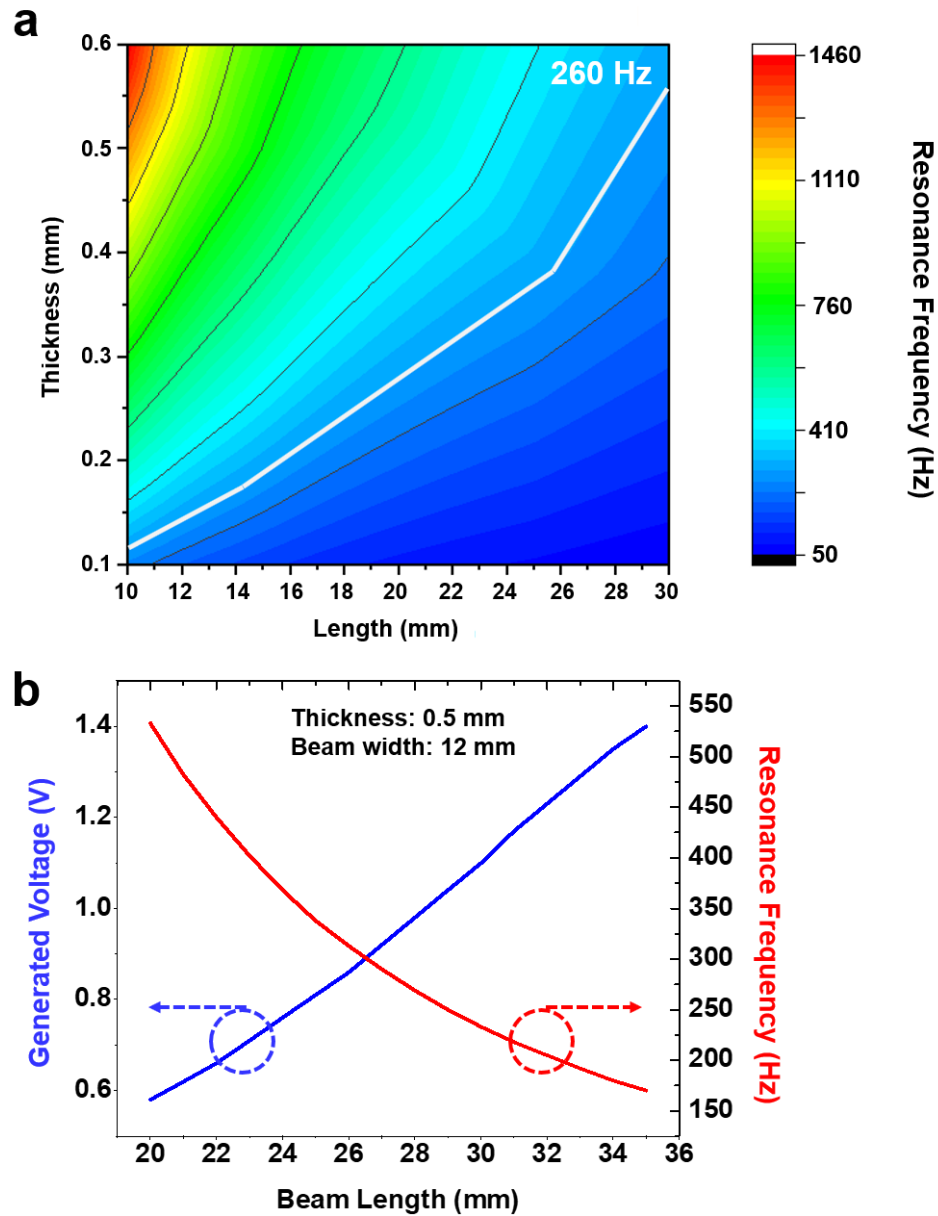


Figure 5.3: Expected resonance frequency and generated power of the beam using simulation method. (a) Resonance frequencies obtained from simulations with varying both lengths and thicknesses of the beam. The white line indicates the 260 Hz of resonance frequency. (b) Generated voltage and resonance frequency expectations as the beam length increases, when the thickness and the beam width were fixed. When the beam length is 28 mm and the resonance frequency is 260 Hz, 1.0 V will be generated.

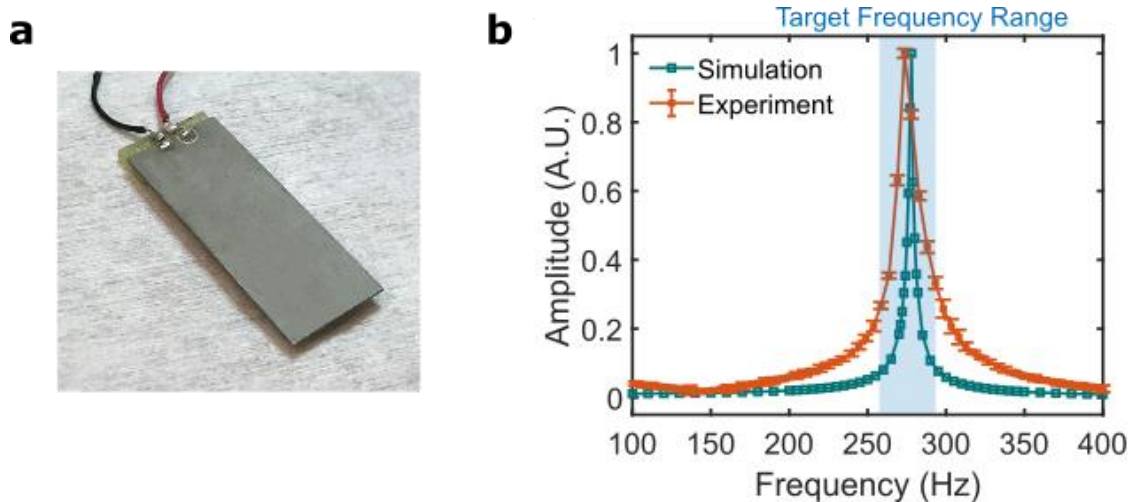


Figure 5.4: Fabricated energy harvesting cantilever beam (a) and its frequency analysis (b). Both simulation result and measurement data are shown in (b).

PZT-5A sheets were purchased from Piezo System Inc. The metal shim was placed between two PZT-5A sheets to construct the bimorph structure. Laser micromachining process was applied to cut the beam. The fabricated cantilever beam is shown in Figure 5.4a. For the frequency analysis, this beam was evaluated using a vibration generator. The vibration generator (3B Scientific's U56001) was controlled by a function generator to vary the frequency. Figure 5.4b shows the relative output voltage amplitude normalized to its maximum from simulation and experimental results. The resonance frequency of the cantilever beam was 274 Hz, within the target frequency range.

Then, the energy harvesting array was designed to collect energy from multiple piezoelectric energy harvesters using a 3D printed structure. As discussed earlier, the larynx serves as the most efficient vibration generating location, although it has a limited physiological surface area. For efficient utilization of this potential energy source (laryngeal vibrations), we stacked the cantilever devices using a 3D-printed package to create a parallelly-connected energy harvesting array. To transfer the vocal vibrations to piezoelectric devices efficiently, it was necessary to build an optimized packaging structure

that aids in the vibrational energy to be delivered through an array of piezoelectric cantilever beams with minimal loss of vibrational energy. Each piezoelectric cantilever was placed inside a casing (Figure 5.5a), and multiple casings were then stacked and rigidly clamped, forming a multi-stack array (Figure 5.5b). The clamping package was built using Ultimaker's Ultimaker2 3D printer. Polylactic acid (PLA) was chosen for the 3D printing material due to its rigid and sophisticated printing properties. A 10-stacked energy harvesting array assembled in the clamping package is shown in Figure 5.5b. This package can tightly hold the energy harvesting array allowing to maximize the vibration transfer. The outer dimension of the package, which consists of 2×5 rigidly clamped cantilevers (10 units in total) forming an energy harvesting array, was 30×35×22 mm³. The bottom part of the clamping mount included a curved surface with a 46 mm radius of curvature to fit the geometry of the neck (Figure 5.5c).

Afterwards, phase synchronization effect was tested to ensure the minimal energy loss of the package (Figure 5.6a). Synchronization is the process where two or more systems interact with each other and start to actuate together. A well-known experiment for describing the synchronization is the metronomes experiment (Pantaleone, 2002). The metronomes all move in a different manner at the beginning, but they become synchronized and move together after they are placed on rolling cans (Figure 5.6a). The small motion of the base couples each vibrating object causing synchronization. Similarly, our packaging structure with 10 cantilevers acts like a moving base with metronomes. In Figure 5.6b, the packaging structure acts like the board and the neck acts like a can, so that the small motion of the clamping package couples the cantilevers and makes them in-phase.

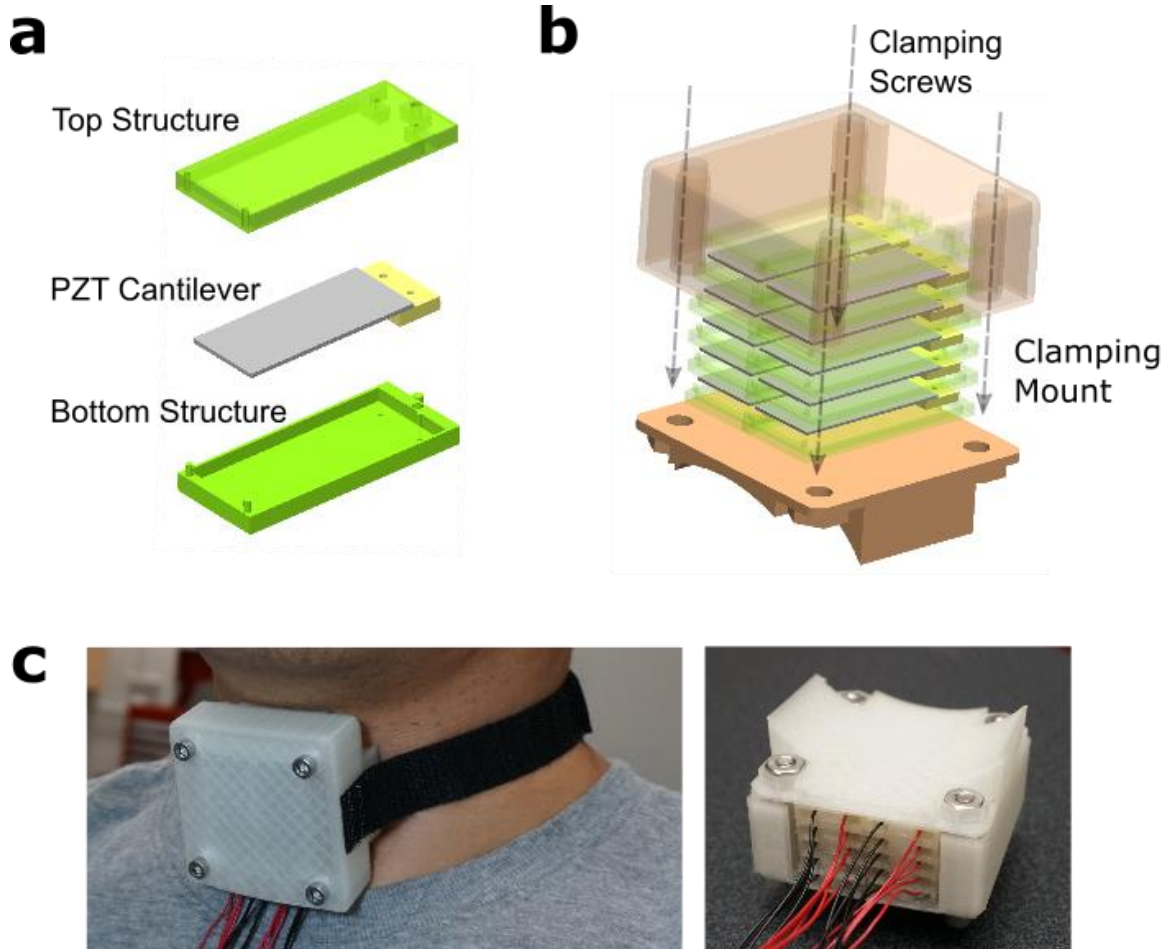


Figure 5.5: Structure of the energy harvesting package. (a) 3D-printed package for unit energy harvesting device. (b) Clamping packaging structure containing 10 energy harvesters. The 10-energy harvesting array consists of 10 energy harvesters packaged in a unit structure, then the whole structure is rigidly clamped in the 3D-printed clamping structure and screws. (c) Assembled 10-stacked energy harvesting array fixed on the larynx. The bottom surface of the clamping structure has a curvature, so that it can fit to the outer diameter of the neck.

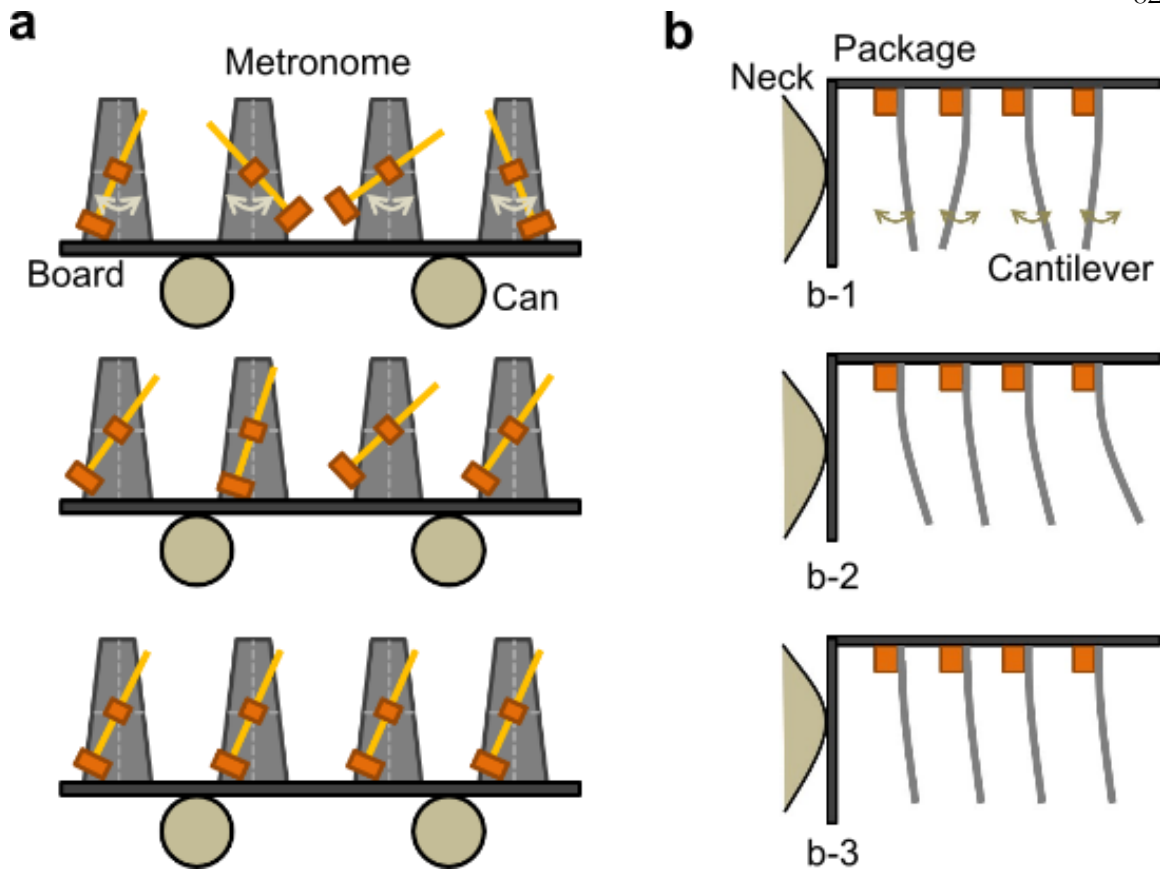


Figure 5.6: Synchronization effect found in the clamping package structure. (a) Metronome experiment. (b) Cantilevers in the clamping package first move out of phase, and eventually couple in phase.

We observe this synchronization effect by measuring transient AC signals from 4-stacked cantilevers in the clamping package. Right after the start of humming, a large phase difference is observed in the transient phase (Figure 5.7b-1). However, after 50 msec, the waves start synchronizing with minimal phase difference leading to the steady state condition. The phase difference among 4 cantilevers was less than 0.06π . Such synchronized AC transient signals contribute significantly to the AC-DC converting step for higher converting efficiency.

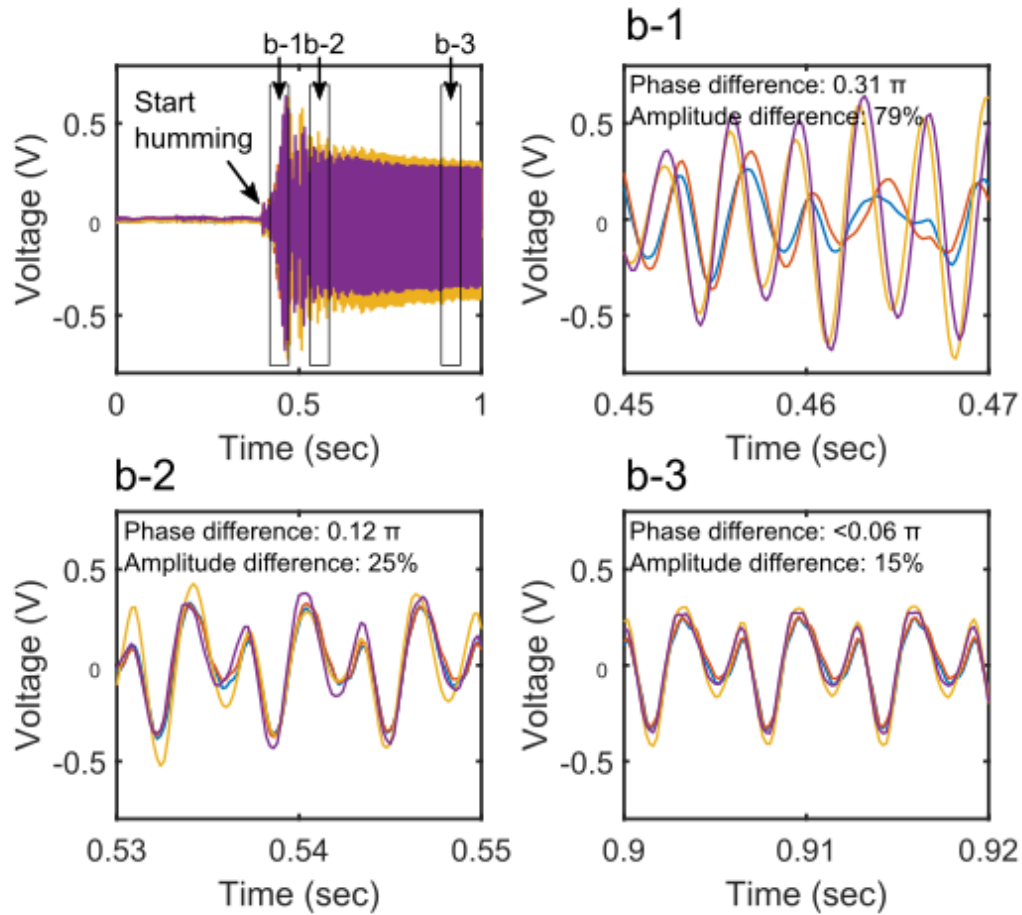


Figure 5.7: Transient signals from four energy harvesters. When the humming started, the phase difference and amplitude difference were large (Phase b-1), but the waves started to synchronize together after 50 milliseconds (Phase b-2), then eventually settled in near complete synchronization (Phase b-3).

5.2 Energy Harvesting Circuit and System

To demonstrate the efficient energy harvesting capability of the PZT devices, we built an energy harvesting system including an array of piezoelectric devices, an AC/DC converter, a boost charger, and a battery together with our collaborator in Texas A&M University (TX, USA) (Figure 5.8a). Firstly, we designed a battery charging system using a passive LC resonant voltage double rectifier and a boost charger shown in Figure 5.8b. The presence of a large internal capacitance of the piezoelectric device, C_{PZT} , significantly

decreases the energy harvesting efficiency because its charging and discharging operation at every cycle consumes a large portion of the sinusoidal output current of the PZT device. This reduces the output current to the load and consequently the output power. Therefore, it is critical to minimize the charging and discharging of the internal capacitance to accomplish a higher efficiency. To solve this issue, we used a passive LC resonant rectifier because the parallel LC resonance stops the output sinusoidal current from flowing into the internal capacitance. The schematic of energy harvesting array and LC resonance rectifier is shown in Figure 5.8b. Moreover, since the human vocal vibration frequency is stable around 260~280 Hz, the potential resonance frequency mismatch of the LC resonant rectifier can be overcome.

Based on the modeling of a single unit device, the matching inductance was determined. Also, Schottky barrier diodes (Avago Technologies' HSMS-2862) were employed in order to reduce the diode forward voltage drop. The boost charger Analog Devices ADP5090 was used for the DC voltage step-up conversion. The ADP5090's maximum power point tracking (MPPT) property helps to convert the rectified voltage to a higher voltage level suitable for LiPo battery charging. Circuit simulations by Linear Technologies LTSpice were also done to expect the amount of voltage generation (Figure 5.8c). In this simulation, the parallel-connected current source, resistor, and capacitor are equivalent to the piezoelectric device. For the data acquisition, we connected the energy harvesting devices to a National Instruments' Data Acquisition (DAQ) device (USB X-Series).

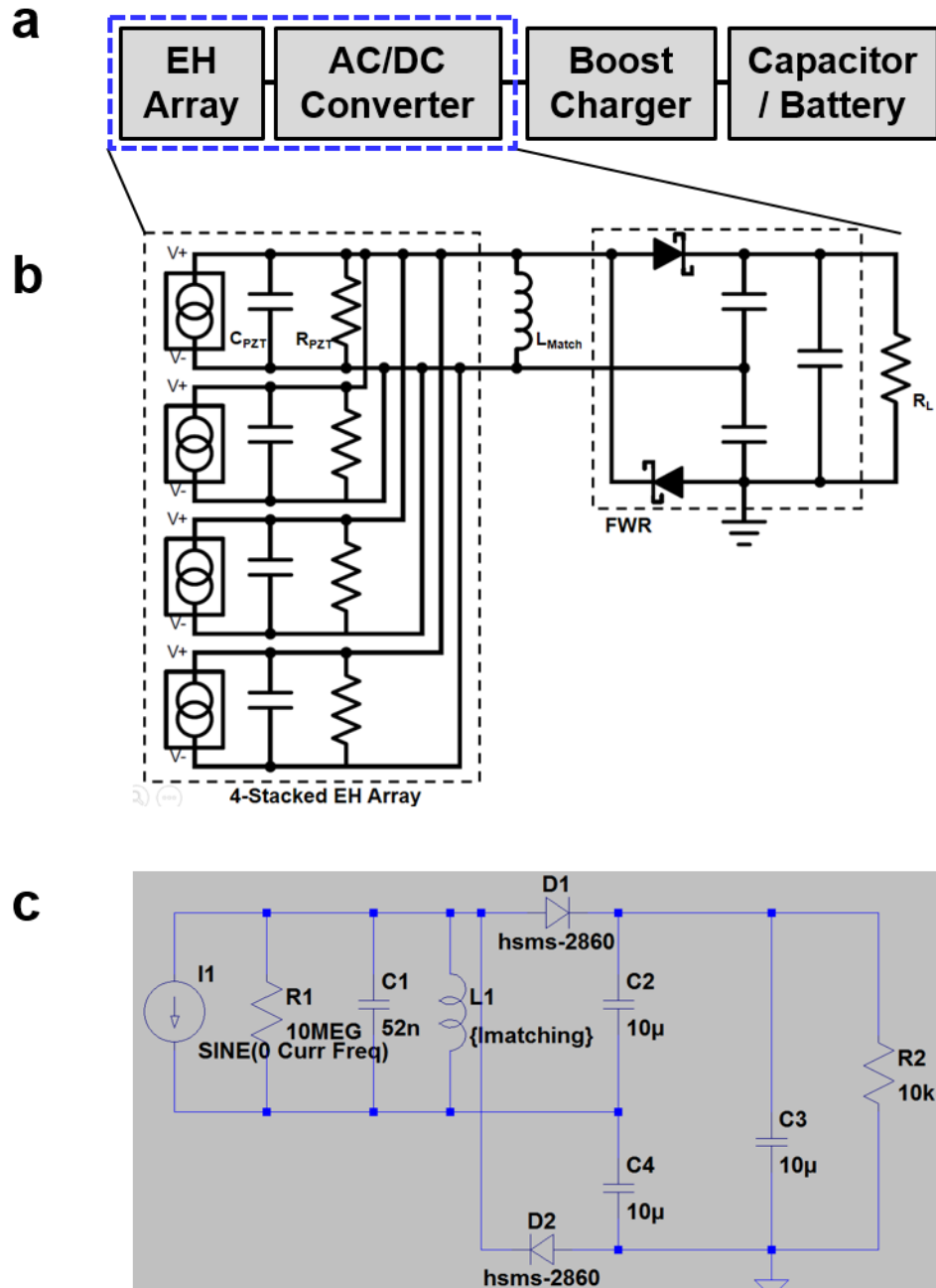


Figure 5.8: Energy harvesting circuit in the energy harvesting system. (a) Energy harvesting system diagram. (b) Schematic of the energy harvesting system including the 4-stacked energy harvesting array and the LC resonant double rectifier. (c) LTSpice schematic of the piezoelectric device and the LC resonant voltage double rectifier.

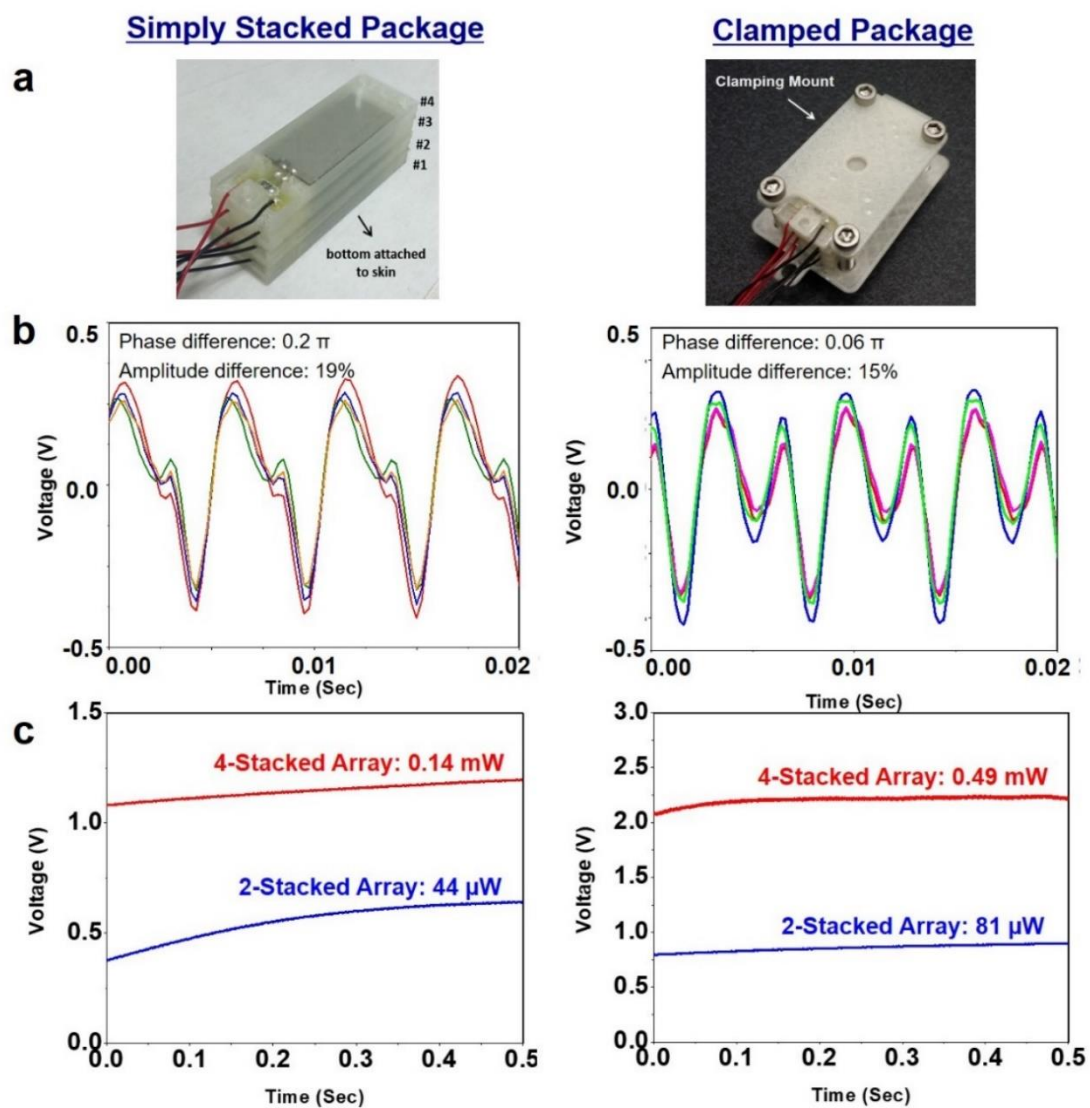


Figure 5.9: Comparison of the simply stacked package and the clamped package using 2- and 4- stacked arrays. (a) Photo images of the simply stacked package and clamped package using 4 devices. (b) Transient measurements using each package without AC/DC conversion. The simply stacked one shows larger phase and amplitude differences. (c) DC output voltage measurements using AC/DC converter. The clamped packaged devices generated about twice more output voltage than voltage that the simply stacked package generated.

Firstly, we measured the output voltage from the energy harvesting (EH) array with the clamping package. To measure the power generation efficiency of the clamping package, voltage generation from the EH array with the simply stacked package (Figure 5.9a) was also analyzed. We used a vibration generator (3B Scientific U56001) with a function generator to maintain the same amount of vibrations to the EH array. Figure 5.9b shows the AC transient measurements without the AC/DC converter. Both phase difference and amplitude difference were improved using the clamping package with the synchronization effect. With the AC/DC converter and a 10 kOhm output load, the 2- and 4-stacked clamping packages showed a 100% improvement in DC voltage generation as compared to a 4-stacked package only. 81 μW and 49 μW were generated from the 2- and 4- stacked EH clamping packages, respectively (Figure 5.9c).

The AC/DC converter with LC resonant rectifier was then applied to the 10-stacked EH array. We varied the load resistance (R_L) and measured the DC output voltage to find the optimum load for extracting the maximum power from the 10-stacked EH array. As shown in Figure 5.10a, we found the optimal load value to be 10 kOhm. Then, we characterized the output power from the EH arrays. Figure 5.10b shows the simulated and measured output voltage from each structure. The circuit simulation was also performed using LTSpice. The electrical powers generated using single-, 4-, and 10-stacked EH arrays were 37 μW (0.6 V_{DC}), 0.49 mW (2.2 V_{DC}), and 3.12 mW (5.5 V_{DC}), respectively. Therefore, the generated voltage is proportional to the number of stacked devices.

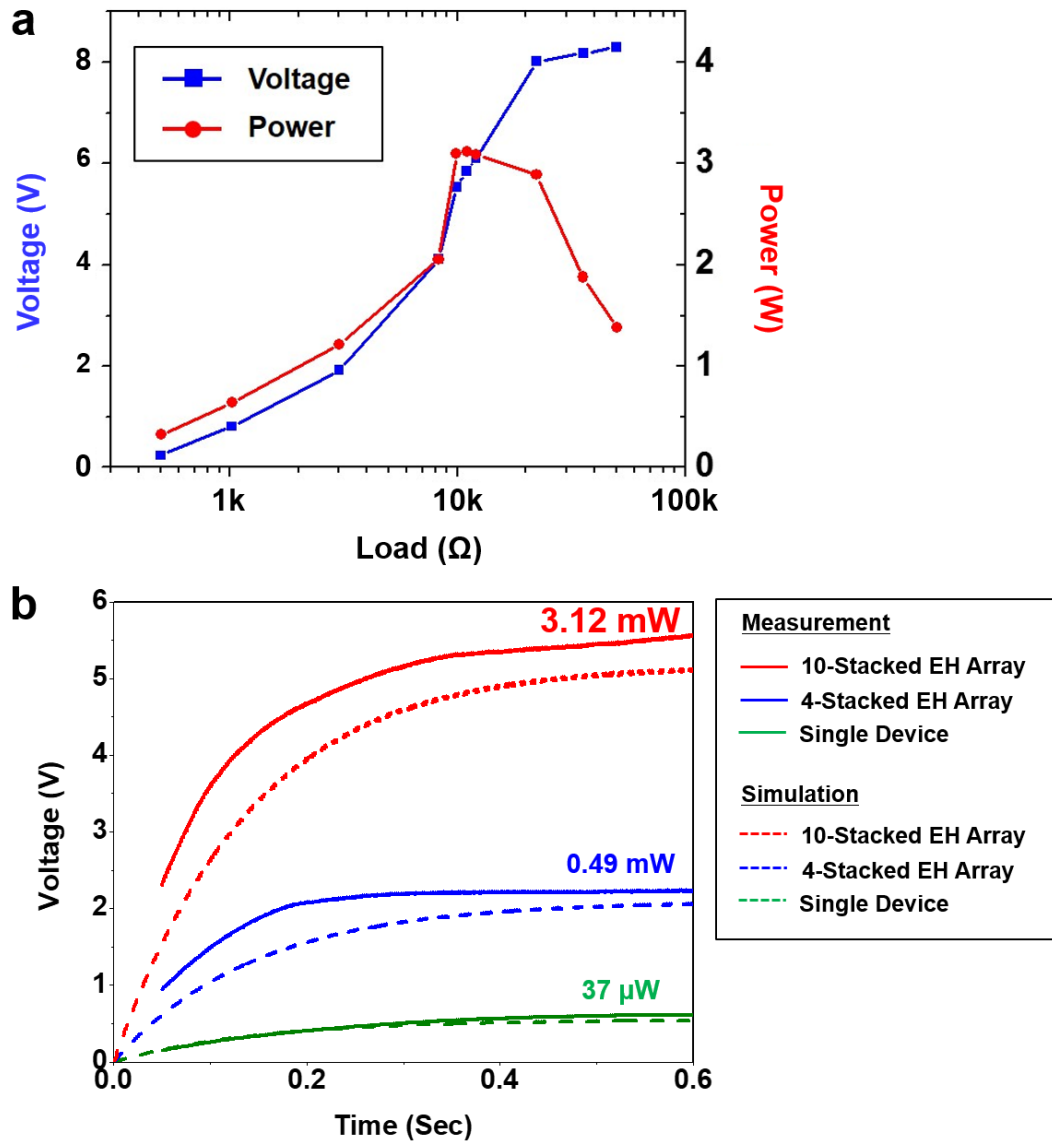


Figure 5.10: DC voltage measurement using clamping packaged EH array and LC resonant rectifier. (a) Load optimization for 10-stacked EH array. (b) DC output voltage measurements and simulation results using different number of stacked piezoelectric devices.

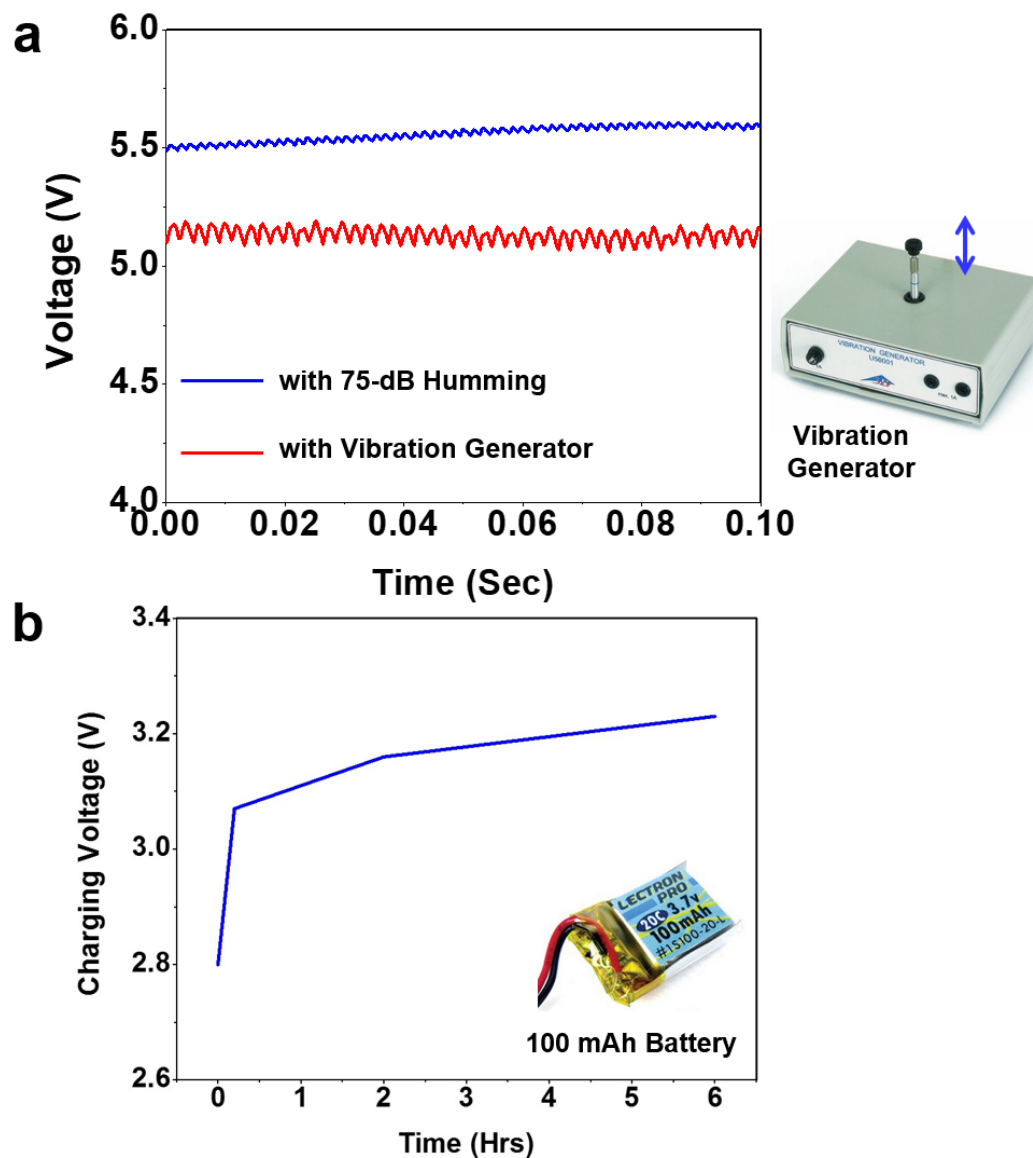


Figure 5.11: Charging a Li-Po battery using the energy harvesting array. (a) DC voltage generation using a vibration generator with 10-stacked EH array to charge a Li-Po battery for a long time. (b) Charging voltage to charge 3.7 V-100 mAh LiPo battery for six hours.

By adding a boost charger to the LC resonant rectifier, a 100 mAh LiPo battery was charged. To mimic a 75-dB humming for an extended time period, a vibration generator was utilized. The comparison of voltage generations from 75-dB humming and the

vibration generator is shown in Figure 5.11a. The 3.7 V - 100 mAh battery was charged up to 3.23 V after 6 hours of long-term charging.

Next, active diodes were applied to a full wave rectifier for further boost in voltage generation from the EH array. AC to DC conversion was conducted by a full wave rectifier which consists of two active diodes, two passive diodes, and a switched inductor (Figure 5.12a). The designed full wave rectifier is composed of two passive diodes (D_1 and D_4) and two active diodes (D_2 and D_3). An active diode is a combination of a comparator and a NMOS transistor. Since a large forward voltage drop across a diode deteriorates the power conversion efficiency of a rectifier significantly, it is important to have low a forward voltage drop. From this perspective, an active diode is preferred to a passive diode. However, active diode implementations of D_1 and D_4 require PMOS transistors which tend to increase the number of devices in low voltage operation due to small on-resistance. Therefore, Schottky barrier diodes were employed for D_1 and D_4 .

The SSHI technique (Guyomar et al., 2005) was also implemented by an inductor, a switch, sensing circuits (R_{SEN} and C_{SEN}), and pulse-based control circuits including hysteresis comparators and pulse generators. The principle behind the SSHI is flipping the voltage, V_{PZT} , across C_{PZT} instantly by using an inductor when the direction of the output AC current changes reducing the amount of charges that flow into the C_{PZT} from the PZT device. Furthermore, a smaller inductance can be used in comparison with that of the resonance rectifier because high frequency resonance is desirable for quick voltage flipping. To detect the direction change of the output AC current, I_{PZT} , a first order high pass filter was implemented by R_{SEN} and C_{SEN} . The hysteresis comparators and pulse generators are controlled when the inductor switch is turned on/off for voltage flipping. The pulse width generated by the pulse generators is adjustable to filter out glitch pulses at the inductor switch so that the undesirable inductor switching is prevented. Figure 5.12b shows the detailed schematic of the full wave rectifier with active diodes drawn by Altium's Altium Designer. Toshiba Semiconductor's SSM6N44FELMCT NMOS transistors were used for active diodes. For the two passive diodes in the full wave rectifier circuit, Schottky diodes

from Avago Technologies (HSMS-2862) were used. Analog Devices' ADP5090 was applied as a boost charger following the full wave rectifier.

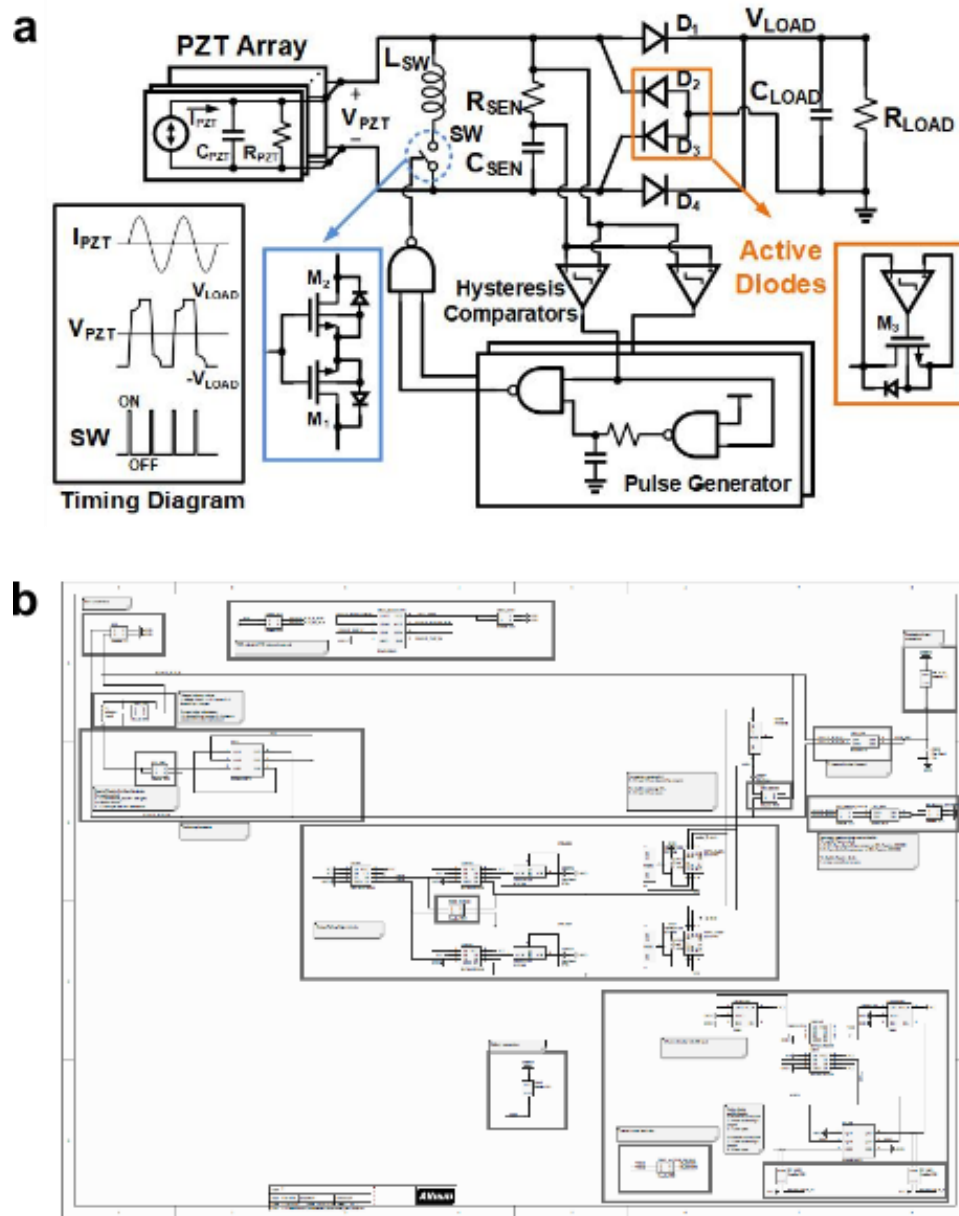


Figure 5.12: Full wave rectifier as AC/DC converter in the energy harvesting system. (a) Schematic of the full wave rectifier as AC/DC converter which consists of two active diodes, two passive diodes, and a switched inductor; the left image is the corresponding circuit board. (b) Detailed schematic including the elements of full wave rectifier, connections between the elements, and the connectors.

5.3 Power Generation Results Using Vocal Vibrations

Figure 5.13a shows the layout design of the printed circuit board (PCB) and the fabricated PCB where the proposed full wave rectifier with a switched inductor was implemented. The layout was drawn using Altium Designer and PCB was fabricated in Mir System Co. Ltd. A passive diode-only full wave rectifier was additionally implemented on this board for the purpose of comparison with the proposed full wave rectifier. The boost charger was connected to this board for DC voltage step-up conversion. The maximum power point tracking (MPPT) property of the boost charger helped to convert the rectified voltage to a higher voltage level suitable for battery charging. For power measurements, the 10-stacked energy harvesting array (Figure 5.5c) was excited using the vocal fold vibrations generated at the larynx of the test participants during humming.

To find the optimum load for the maximum power extraction from the 10-stacked EH array using an active diodes-implemented full wave rectifier, we varied again the load resistance (R_{LOAD}) and measured the DC output voltage. The optimal load is found to be 4 k Ω as shown in Figure 5.13b. Afterwards, we characterized the output power from the EH arrays shown in Figure 5.13c. The generated power using a passive diode-only full wave rectifier was 3.05 mW with 3.57 V_{DC} which is very close to the previous output power using the LC resonant double rectifier (also a passive diode-only AC/DC converter). The EH array with a switched full wave rectifier generated 4.01 V_{DC} and 3.99 mW, showing an increase of 30% compared to the output power using the passive diode-only full wave rectifier.

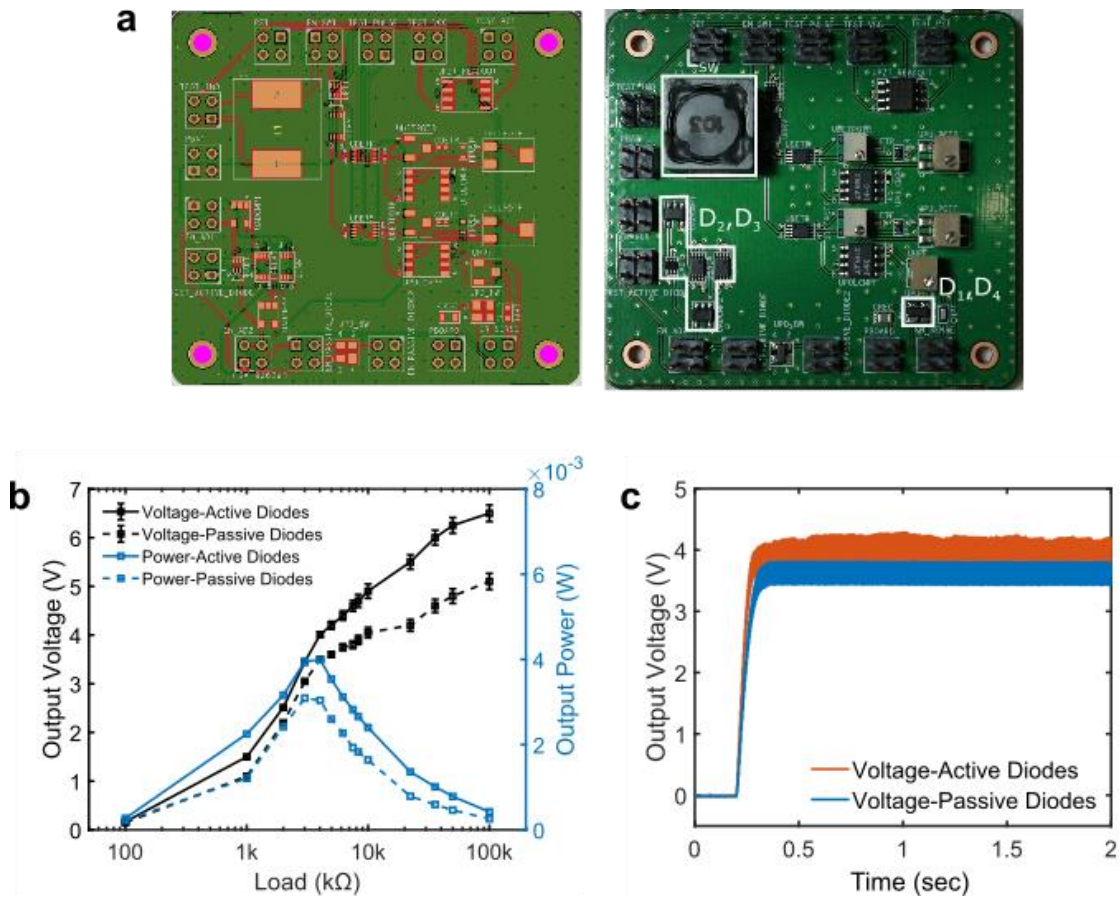


Figure 5.13: Power generation using the fabricated full wave rectifier. (a) Layout design of the printed circuit board (PCB) and the fabricated PCB where the proposed full wave rectifier with a switched inductor was implemented. (b) Load test with active full wave rectifier and passive full wave rectifier. The black line and blue line with triangle symbols are voltage and power measurements from with the active full wave rectifier, and the other black line and blue line with triangle symbols are voltage and power measurements using the passive full wave rectifier. The maximum attained power was found to be at 4 kΩ load. (c) An array of 10 energy harvesting units generated 3.99 mW with a 4 kΩ load.

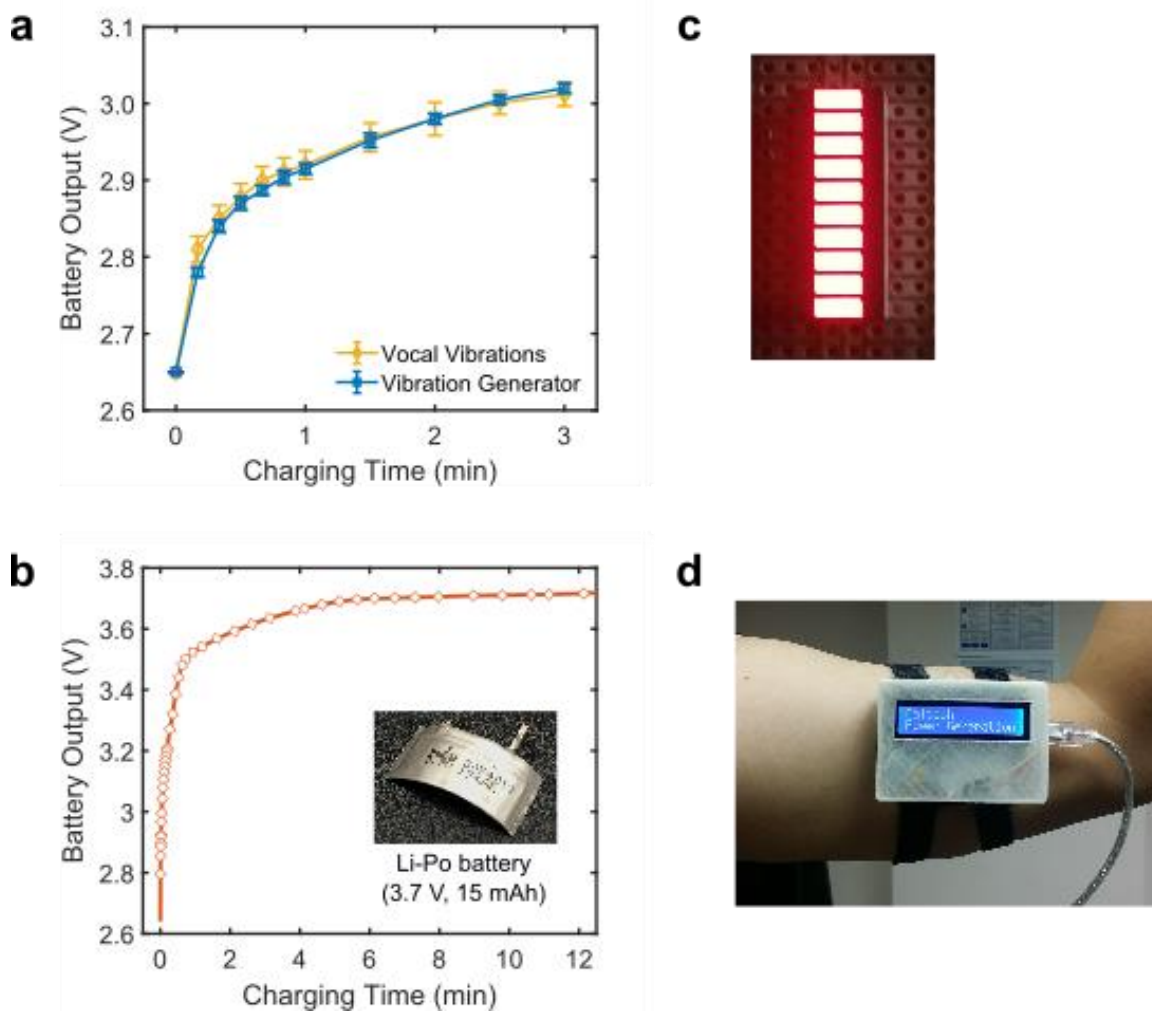


Figure 5.14: 15-mAh Li-Ion battery charging using a 10-stacked energy harvesting array. (a) The first three seconds of battery charging using vocal the vibrations and vibration generator. (b) Cumulative charging with the vibration generator. The voltage at the battery reached 3.76 V after 12 hours of charging. (c & d) The battery charged for 10 minutes with vocal vibrations was sufficient to operate the 10-LED array and the 2×16 LCD backlight unit.

To demonstrate this battery charging capability, the boost charger was loaded with a 15-mAh thin 3.7 V-LiPo battery ($2 \times 12 \times 12 \text{ mm}^3$) instead of a load resistor. Charging the battery in a deeply discharged state with 75-dB humming for 3 minutes increased the

battery output voltage from 2.65V to 3.01V, as shown in Figure 5.13a. The 75-dB humming was verified by a sound level meter (Extech Instruments' 407730). The sound level meter was placed at a distance of 1 m from the sound source to keep producing the 75-dB humming while measurements were taken. We used a vibration generator to mimic vocal fold vibration at 75 dB for longer time periods and were able to charge the battery completely using this method (Figure 5.14a). Charging the 15-mAh battery using vibration energy from the vibration generator is also shown in Figure 5.14a. The transient response of the battery output voltage charged by a vibration generator can be seen in Figure 5.14b. The battery output voltage reached up to 3.72 V after 12 hours.

A battery charged for 3 minutes by 75-dB humming was sufficient to operate a 10-LED array (power consumption: 2.2 V, 10 mA) or a 2×16 LCD unit (power consumption: 2.8 V, 10 mA) for about 30 seconds (Figure 5.14c-d).

Using an array of piezoelectric energy harvesters, we generated electrical power from various locations around the head including jaw, chest, and neck. As discussed earlier, the jaw and chest areas can also be potential energy sources for implantable devices. Figure 5.15a shows the additional hotspot verification at the chest area using 3-axis MEMS accelerometers. The jaw regions provide around 20-40% of the vibration amplitude as compared to the larynx. 14-18% of vibrational energy compared to the energy from the larynx can be provided at a large area on the chest (26×8 cm²).

We experimentally verified jaw and chest locations as energy sources using wearable energy harvesting packages. (Figure 5.15b, c). We constructed appropriate packaging structures suited to each area and tested power generation from each area. Then, we were able to obtain output powers of 1.20 mW and 0.32 mW from the human jaw and chest area, respectively (Table 5.3).

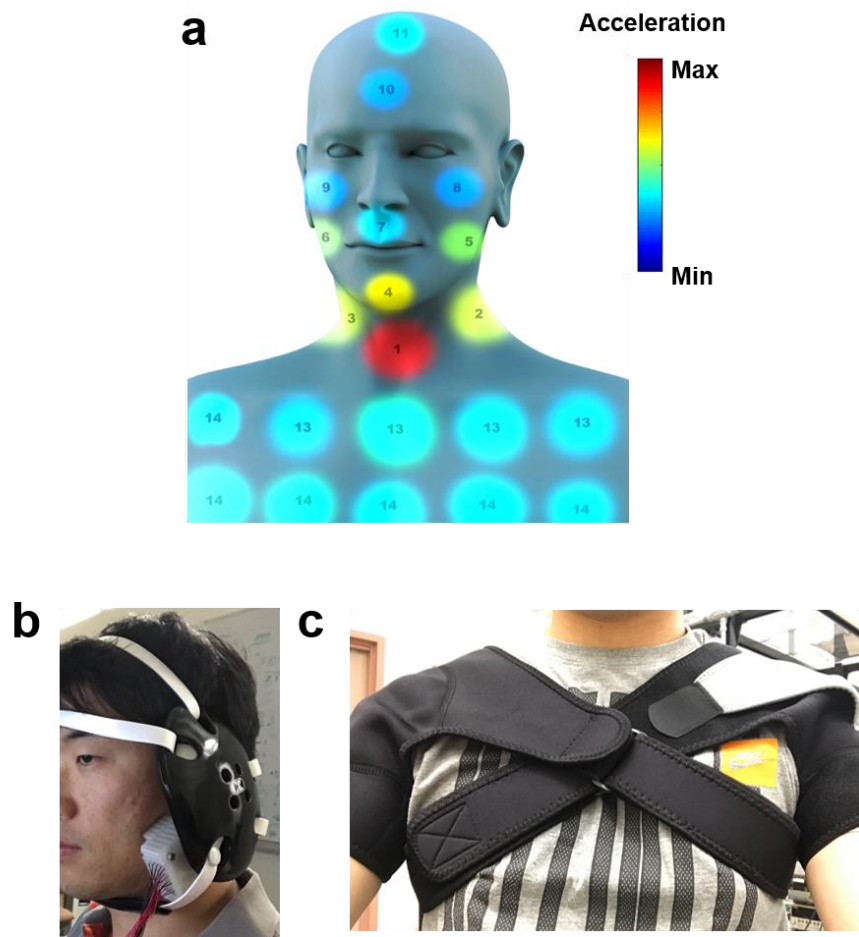


Figure 5.15: Wearable energy harvesting device demonstration. (a) Vibration distribution measured by accelerometers in the upper body including the chest area. (b) Wearable energy harvesting from the jaw area. (c) Wearable energy harvesting package using the chest area. (d) Bow-tie shaped energy harvesting package using the neck area.

As shown in Figure 4.11 and Figure 5.15a, the larynx serves as the most efficient vibration generating location. However, the farther away from the center of the neck, the weaker the vibration energy gets. For practical demonstration of energy harvesting at the larynx, we made a bow-tie shaped energy harvesting package consisting of 4 piezoelectric energy harvesters (Figure 5.16). To implement the energy harvesting system together with the energy harvester, a small sized AC/DC converter, voltage regulator and a 15-mAh Li-Po

battery were attached on the shirt collar. This bow tie energy harvesting device was able to produce an output of 0.62 mW (1.58 VDC), which was capable of charging Bluetooth headphones through a Li-Po battery (Figure 5.16).



Figure 5.16: Bow tie shaped energy harvester using a 4-energy harvesting array. The battery and circuits were placed inside the shirt collar to charge the Bluetooth headphones.

Table 5.2: Power generation using wearable energy harvesting devices.

Device area	Number of energy harvesters used	Generated power (mW) (dc voltage, V_{DC})	Power Density ($\mu\text{W}/\text{cm}^2$)
Jaw	10 (2×5 stacked)	1.2 (2.19)	35.7
Chest	10	0.32 (1.14)	9.5
Neck (bow tie shaped)	4	0.98 (1.98)	72.1

According to Table 4.2, generated powers from the neck, jaw and chest areas were capable of driving biomonitoring systems, pacemakers, cochlear processors, and hearing aids. The deep brain stimulation can also provide pulses using this amount of power depending on the treatment method (Alexis et al., 2004). The power generation results from wearable energy harvesting devices are summarized in Table 5.2. Power density from each location is $35.7 \mu\text{W}/\text{cm}^2$ (jaw), $9.5 \mu\text{W}/\text{cm}^2$ (chest), and $72.1 \mu\text{W}/\text{cm}^2$ (neck).

5.4 Conclusion

The vocal fold vibration-based energy harvesting system developed in this study consisting of a 10-stacked array with switched full wave rectifier stably generated 3.99 mW from human humming at 75 dB. Additionally, we demonstrate a successful charging of a 15-mAh thin LiPo battery, with full charge achieved after 12 hours of cumulative charging. Charging the battery for 10 minutes allowed us to turn on a 10-LED array (requiring 2.2 V, 10 mA) or 2×16 LCD backlight unit (requiring 2.8 V, 10 mA) for about half a minute. Most of the existing biomechanical energy harvesters fall short of producing sufficient output current ($<100 \mu\text{A}$) and meeting the energy requirements of typical wearable electronics – especially medical devices. Our device can produce almost 1mA current with minimal physical effort as summarized in Figure 5.17.

Higher frequencies of vocal fold vibrations ($> 100 \text{ Hz}$) as compared to other biomechanical motions ($\leq 5\text{Hz}$) can assist in further developing efficient electronics to boost up the energy harvesting capabilities. Moreover, the vocal nature of this harvesting technique can be particularly helpful in cases where individual mobility is restricted. These results and features demonstrate that vocal fold vibration-energy harvesting can be a highly efficient and powerful tool for diverse energy applications including wearable communication devices, displays, as well as biomedical implants such as pacemakers, deep-brain stimulators, or cochlear implants.

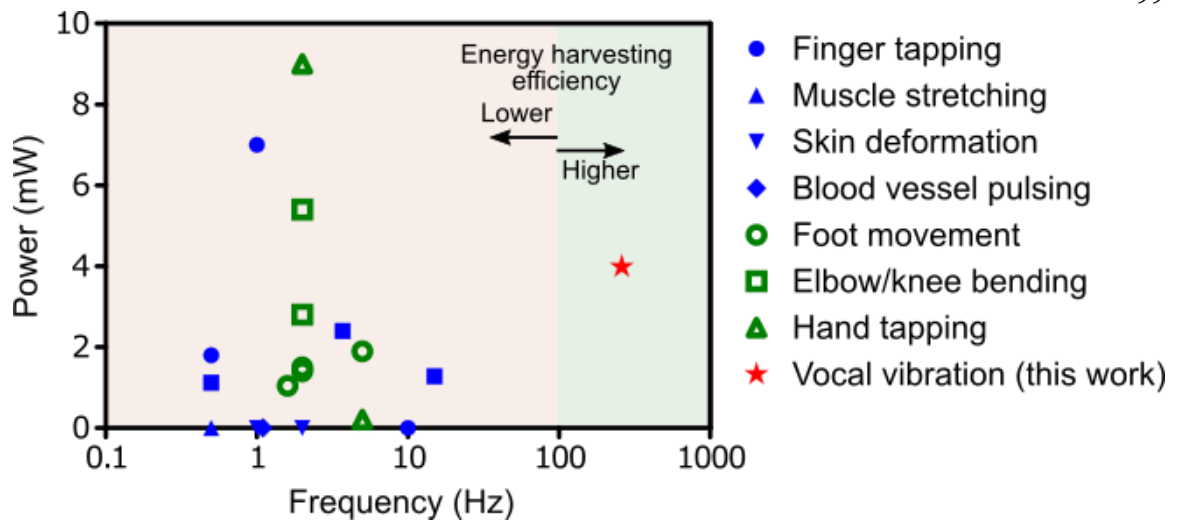


Figure 5.17: Summary of the literature survey on biomechanical energy harvesting devices in terms of output power vs frequency. The results are divided in two colors: blue requiring negligible physical movements and green requiring intensive physical movements. Results acquired in this work are marked and compared with previous literatures.

References

- Williams, C.B.; Yates, R.B. Analysis of a micro-electric generator for microsystems. *Sens. Actuat. A: Phys.* 1996, 52, 1-3, 8-11.
- Erturk A.; Inman D.J. (2011), *Piezoelectric Energy Harvesting*, Wiley Publishing.
- Yang, J.; Chen, J.; Su, Y.; Jing, Q.; Li, Z.; Li, F.; Wen, X.; Wang, Z.; Wang, Z.L. Eardrum-inspired active sensors for self-powered cardiovascular system characterization and throat-attached anti-interference voice recognition. *Adv. Mater.* 2015, 27(8), 1316-1326.
- Park, S. H.; Lee, H. B.; Yeon, S. M.; Park, J.; Lee, N. K. Flexible and stretchable piezoelectric sensor with thickness-tunable configuration of electrospun nanofiber mat and elastomeric substrates. *ACS Appl. Mater. Interfaces.* 2016, 8(37), 24773-24781.
- Chung, S.Y.; Kim, S.; Lee, J.-H.; Kim, K.; Kim, S.-W.; Kang, C.-Y.; Yoon, S.-J.; Kim, Y.S. All-solution-processed flexible thin film piezoelectric nanogenerator. *Adv. Mater.* 2012, 24(45), 6022-6027.
- Persano, L.; Dagdeviren, C.; Su, Y.; Zhang, Y.; Girardo, S.; Pisignano, D.; Huang, Y.; Rogers J.A. High performance piezoelectric devices based on aligned arrays of nanofibers of poly(vinylidene fluoride-co-trifluoroethylene). *Nature Comm.* 2013, 4, 1633.
- Guido, F.; Quattieri, A.; Algieri, L.; Lemma, E.D.; Vittoio, M.D.; Todaro, M.T. AIN-based flexible piezoelectric skin for energy harvesting from human motion. *Microelectron. Eng.* 2016, 159(15), 174-178.
- Mercier, P. P.; Lysaght, A. C.; Bandyopadhyay, S.; Chandrakasan, A. P.; Stankovic, K. M. Energy extraction from the biologic battery in the inner ear. *Nat. Biotech.* 2012, 30(12), 1240.
- Dagdeviren, C.; Yang, B. D.; Su, Y.; Tran, P. L.; Joe, P.; Anderson, E. et al. Conformal piezoelectric energy harvesting and storage from motions of the heart, lung, and diaphragm. *Proc. Natl. Acad. Sci. U.S.A.* 2014, 111(5), 1927-1932.
- Sodano, H.A.; Inman, D.J.; Park, G. Comparison of piezoelectric energy harvesting devices for recharging batteries. *J. Intell. Material Syst. Struct.* 2005, 16 (10) 799-807.
- Sodano, H.A.; Inman, D.J.; Park, G. A review of power harvesting from vibrations using piezoelectric materials. *Smart Mater. Struct.* 2004, 16 (3), R1.
- Pantaleone, J. Synchronization of metronomes. *Am. J. Phys.* 2002, 70, 992-1000.
- Guyomar, D.; Badel, A.; Lefeuvre, E.; Richard, C. Toward energy harvesting using active materials and conversion improvement by nonlinear processing. *IEEE T. Ultrason. Ferr.* 2005, 52, 584-595.

PRACTICAL ENERGY HARVESTING FROM HUMAN VOCAL FOLDS

As shown in the previous chapter, vibrational energy from vocal folds can be a good candidate as an energy harvesting source for various kinds of wearable or implantable devices around the human head. For practical use of human vocal vibrations, we showed feasible power generation from the neck, jaw, and chest areas. In addition, the location at the top of the head was also studied as available energy source for deep brain stimulation.

Speaking is more general phonation process than humming, but the frequency during talking/reading is more spread than that from humming (Figure 4.7). Even the dominant frequency keeps changing while talking/reading. Therefore, it is necessary to develop an energy harvesting device for pragmatic use of vocal vibrations that can be utilized at a broadband frequency. In this chapter, we will showcase the development of piezoelectric energy harvesting structures for low frequency broadband applications using serpentine and spiral shaped designs. For spiral shaped structures, the resonance frequencies of multi-mode vibrations were controllable by changing the design parameters of the spiral beams. Our comprehensive comparative studies between the serpentine and spiral structure showed that the spiral structure is superior for the low frequency, broadband vibration driven energy harvesting method. In the process, dc voltage generation of 0.61 V is successfully achieved using the normal sound level of book reading.

Additionally, the location at the top of the head is studied to project a relatively large area of vibration hotspot to harvest energy to the medical implant around the human brain. A realistic head model was used to verify the applicable area on the scalp and on the skull and a titanium packaged energy harvesting device was applied to test this top of the head location.

6.1 Energy Harvesting for Broadband Application

As discussed in Chapter 4, the frequency range of vocal vibrations from reading or speaking is more spread out than that from humming. As shown in Figure 4.8, frequencies of males and females while humming range between 100-160 Hz and 180-220 Hz, respectively. Consequently, broad resonance frequency of energy harvesting devices can achieve more efficient power generation leading to practical and viable applications of vocal vibrations.

Recently developed energy harvesting techniques from human body motions (vocal vibrations, footsteps, breathing motion) as described in Section 4.1, or the environment such as wind or tidal current (Lee et al., 2012; Wang, 2014; Li et al., 2014) function at a very low frequency (1-100 Hz). However, state-of-the-art efficient energy harvesters operate at frequencies above 1000 Hz. In this regard, developing energy harvesting methods efficient in low frequencies for broadband applications is an urgent issue in energy harvesting field.

Unfortunately, energy harvesters with low resonant frequencies typically suffer from reduced electrical power generation. Harvesting low-frequency energy using an electromagnetic generator may be ineffective, since the output power decays greatly with the decrease of frequency (Kulah and Najafi, 2004) and the output voltage is rather low at low frequencies.

In case of piezoelectric energy harvesting, the resonance frequency (f_r) of the beam is dependent on the beam length, l , beam width, b , and beam thickness, d , as shown in Equation 6.1. For a general rectangular beam, d needs to be low because increasingly compliant springs are required to resonate at lower frequencies for a given area. This requires additional space to permit large mechanical displacements as well as mechanical stops to prevent breakage during accelerations. The extra space lowers the system's power density and form factor. In addition, the reduced volume of the piezoelectric material due to thin thickness can decrease the total mechanical energy input, W_t , due to the relation

between W_t and the volume, vol , as described in Equation 6.2 where s_{33}^D is elastic compliance and T is stress on element.

$$f_r \propto \sqrt{\frac{bd^3}{l^4}} \quad (6.1)$$

$$W_t = \frac{(vol)(s_{33}^D T^2)}{2} \quad (6.2)$$

To achieve low resonance frequency in a limited area, several types of structures have been reported such as S-shaped structures (Liu et al., 2012), cymbal structures (Kim et al., 2004), and 3D configurations (Hu et al., 2013; Tao et al., 2014). However, they were still not appropriate for broadband applications since they only focused on the first mode vibration to lower the resonance frequency. We have designed serpentine and spiral shaped piezoelectric structures whose vibration modes are controllable with changing the design parameters to get broadband frequency response at target resonance frequency. Afterwards, we have fabricated and characterized the structures to confirm the design and simulation.

Firstly, the serpentine structure and spiral structure were designed using FEM simulations (COMSOL Multiphysics) to determine the design parameters. Then, the designed beams were fabricated using laser cutting methods. Using these fabricated beams, the mode shapes were obtained from laser Doppler vibrometer (LDV) and frequency responses were measured by mechanical energy-to-electrical energy measurement setup. Lastly, the electrical powers from both types of beams were measured while humming and reading.

Figure 6.1a shows the basic configuration of the serpentine beam and the spiral beam that we applied to the energy harvesting structure. Bents in the serpentine beam were at right angles to use as a large piezoelectric area as possible in a given space. The Archimedean spiral which has consistent beam width was chosen as a spiral structure. The length of the spiral beam, L_{ser} can simply be expressed as Equation 6.3 where b is the outer width, g is

the gap between bents and n_{ser} is the number of bents. At a given outer dimension, g is determined by n_{ser} . The radius of the spiral beam can be described by the Equation 6.4 where a is the initial radius, b_g is the spiral radius growth rate, which is determined by the number of turns n_{spi} , and r and θ are in polar coordinates. The effective length of the spiral beam, L_{spi} , can be obtained from Equation 6.5 where θ_1 is the initial angle and θ_2 is the final angle. Figure 6.5b shows the calculated spiral length by changing a and n_{spi} at a given outer dimension ($12 \times 12 \text{ mm}^2$). To get the target resonance frequency at a given outer dimension, every parameter in the serpentine beam is kept fixed, while two parameters including a and n_{spi} are changed for the spiral beam.

$$L_{ser} = (n_{ser} + 1)b + n_{ser}g \quad (6.3)$$

$$r = a + b_g\theta \quad (6.4)$$

$$L_{spi} = \int_{\theta_1}^{\theta_2} \sqrt{r^2 + \left(\frac{dr}{d\theta}\right)^2} d\theta \quad (6.5)$$

The modal analysis of the rectangular, serpentine, and spiral structures obtained from simulations are summarized in Table 6.2. The top left end of each beam is kept constant and the color map expresses the amount of displacement. The serpentine and spiral beams were designed to get the first mode resonance frequency at 200 Hz, and the rectangular beam has the same dimension as the other two. The n_{ser} of the serpentine beam was 6 turns, and a and n_{spi} of the spiral beam were 1.5 mm and 5 turns, respectively. The first mode shape is bending towards the beam end, while the second mode is torsional bending. The third mode is second harmonic bending at the beam end. The frequency response using this serpentine beam is shown in Figure 6.6. Although 200 Hz of resonance frequency can be achieved in a given area ($12 \times 12 \text{ mm}^2$), other resonance modes exist away from the frequency range of vocal vibrations.

The spiral beam was further studied to examine the change of resonance frequencies with respect to the inner radius and number of turns. Further modal analyses of spiral beams

with a different initial radius with a fixed number of turns of 5 are shown in Table 6.3.

While the effective beam length increases by increasing the initial radius, the resonance frequency at each mode decreases.

The first to the sixth resonance frequencies were calculated using COMSOL Multiphysics at each initial radius (0.5 - 4.0 mm) and number of turns (2 - 8) as shown in Figure 6.3. The resonance frequencies are plotted with respect to the initial radius (n_{spi} fixed) and number of turns (a fixed). In both cases, the resonance frequencies are inversely proportional to the initial radius and number of turns. Also, it should be noted that the resonance frequency decreases to a larger slope as the modal order increases, so the resonance frequency of each mode gets closer at a large initial radius or number of turns.

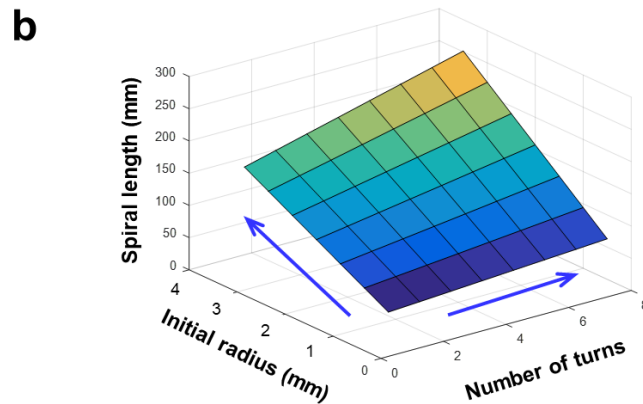
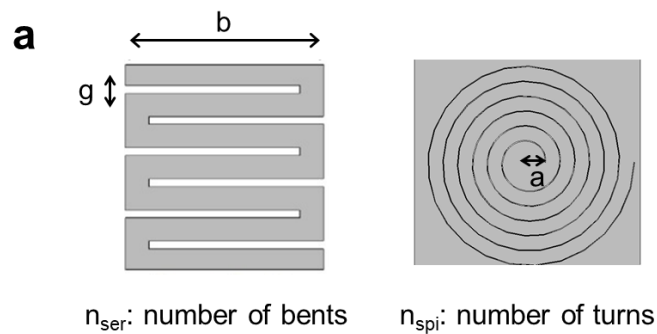
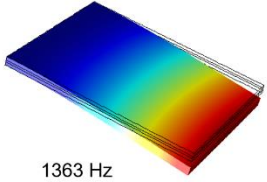
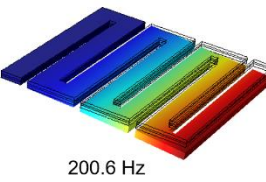
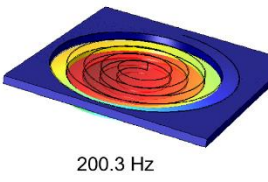
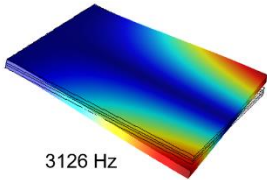
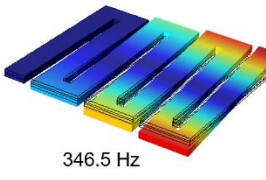
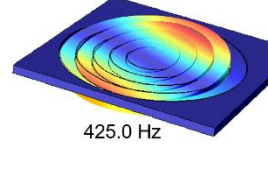
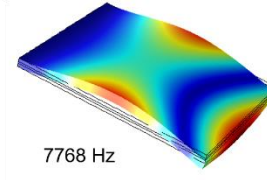
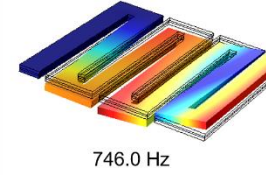
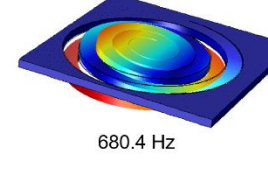


Figure 6.1: Determining the parameters of the serpentine and spiral beams. (a) Basic configuration of serpentine beam and spiral beam used for the energy harvesting structure. (b) Calculated spiral length by changing initial radius and number of turns of the spiral at a given outer dimension ($12 \times 12 \text{ mm}^2$).

Table 6.1: The 1st, 2nd and 3rd mode shapes of the rectangular, serpentine, and spiral beams.

Resonance Mode	Rectangular Beam	Serpentine Beam	Spiral Beam
1st	 1363 Hz	 200.6 Hz	 200.3 Hz
2nd	 3126 Hz	 346.5 Hz	 425.0 Hz
3rd	 7768 Hz	 746.0 Hz	 680.4 Hz

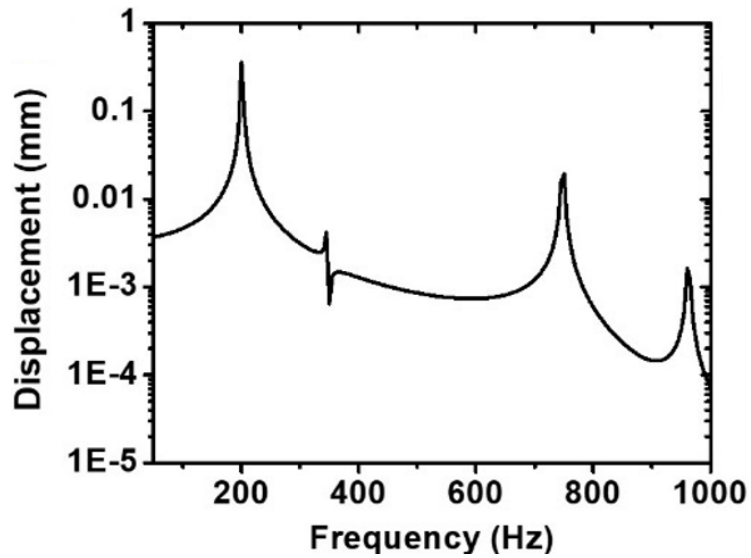
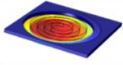
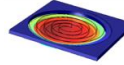
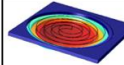
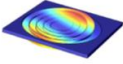
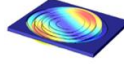
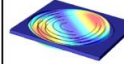
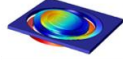
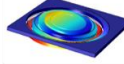
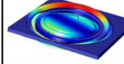
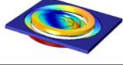
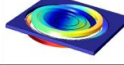
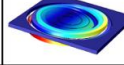
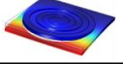
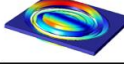
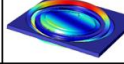
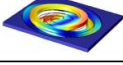
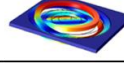
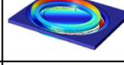
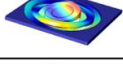
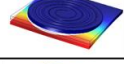
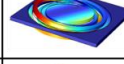
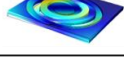
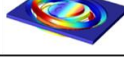
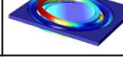


Figure 6.2: Frequency response of serpentine beam from simulation. This beam has 6 bents and the beam width is 1.5 mm.

Table 6.2: Mode shapes (modal order is 1 to 8) of spiral beams with a different initial radius of spiral when the number of turns is fixed at 5.

Mode #	a=1.0			a=2.0			a=3.0		
	Freq (Hz)	Mode Name	Deflection Shape	Freq (Hz)	Mode Name	Deflection Shape	Freq (Hz)	Mode Name	Deflection Shape
1	235	1 st bending		168	1 st bending		109	1 st bending	
2	492	1 st torsional		366	1 st torsional		249	1 st torsional	
3	794	2 nd bending		580	2 nd bending		399	2 nd bending	
4	1083	2 nd torsional		821	2 nd torsional		597	2 nd torsional	
5	1265	Beam bend		908	3 rd torsional		644	3 rd torsional	
6	1559	3 rd torsional		1052	4 th torsional		712	4 th torsional	
7	1963	3 rd bending		1245	Beam bend		852	5 th torsional	
8	2466	4 th torsional		1272	5 th torsional		1004	6 th torsional	

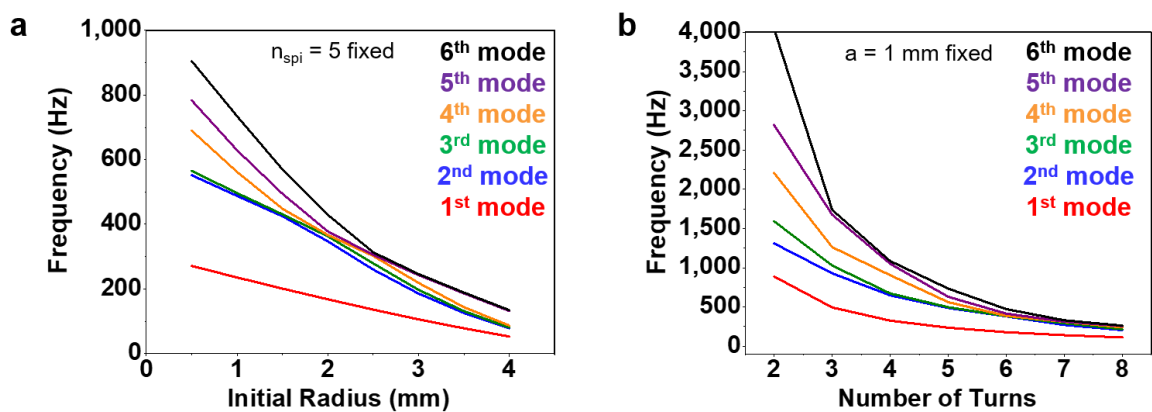


Figure 6.3: Calculated resonance frequencies at 1st to 6th mode with (a) the initial radius changed (number of turns fixed) and (b) different numbers of turns (initial radius fixed).

6.2 Characterization of the Broadband Applicable Piezoelectric Beams

Serpentine and spiral shaped structures were patterned by the laser cutting process. To minimize the crack issue at the cutting edge and the loss of area by the cutting process, the ultra-short pulse (8 psec) laser micromachining (Ekspla's Nd:YAG) was chosen for minimal heat effect (Perry et al., 1999; Emmelmanna et al., 2011). The wavelength of the laser source was 355 nm, process power was 4 W, and the repetition rate was 400 kHz. The cutting setup (Figure 6.4a) also had suction tools to remove the debris during the cutting process. The cutting edges of the PZT materials are shown in Figure 6.4b and c. The PZT edge cut by CO₂ laser has a larger burning area and more debris than those caused by an ultra-short pulse laser. The width of area lost by cutting line was 100 μm (CO₂ laser) and 10 μm (ultra-short pulse laser).

The processed serpentine and spiral piezoelectric beams are shown in Figure 6.5. To have the first resonance frequency to be at around 200 Hz, the serpentine beam has 6 number of bents and 1.5 mm of serpentine width, while the serpentine beams were fabricated in five different shapes by changing the initial radius and the number of turns of the spiral.

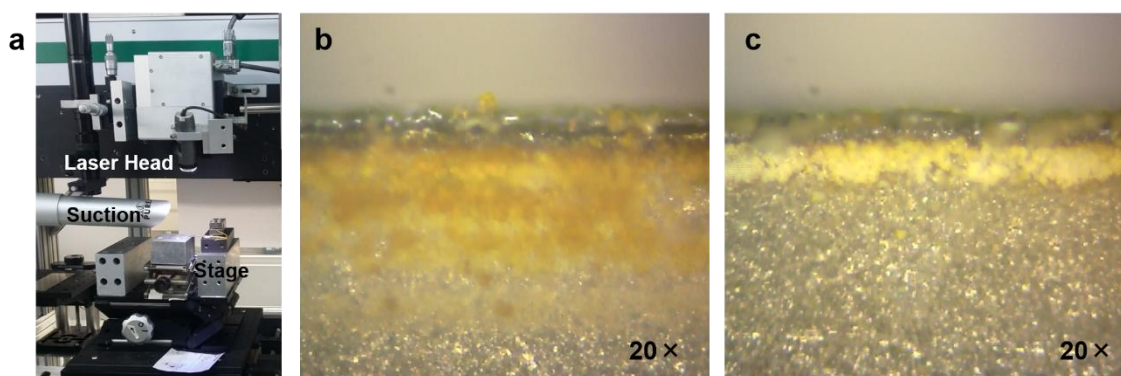


Figure 6.4: Laser cutting process to pattern the serpentine and spiral beams. (a) laser cutting setup including laser head, stage, and suction tool. Laser cutting edge of the piezoelectric material using (a) CO₂ laser and (b) ultra-short pulse laser.

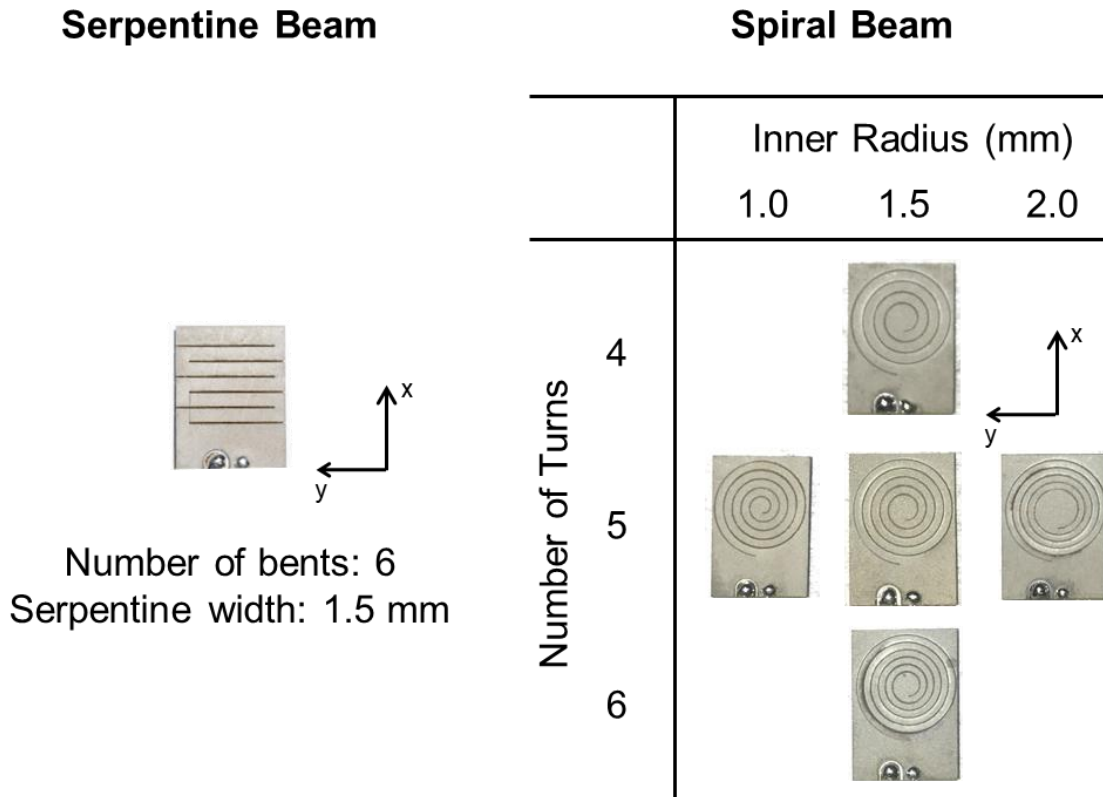


Figure 6.5: Fabricated serpentine beam and spiral beams. Spiral beams were made in five different shapes by varying the inner radius and the number of turns.

The modal analysis was done by a laser Doppler vibrometer (LDV) using the fabricated serpentine and spiral beams with our collaborator in TU Clausthal, Germany (Kowarsch et al., 2017). The LDV measurement setup is shown in Figure 6.6. Polytec OFV-2500-2 decoder was used to measure out-of-plane vibrations on the beams. A dichroitic mirror (DM) superimposed the vibrometer beam with the microscope optics and the Köhler illumination was provided by a LED. 66 equidistant measurement points were chosen along the beams to enable the high resolution of the 1st to even higher deflection modes in x-direction and y-direction. Additionally, for each measurement point, a complex averaging of 25 measurements was conducted to reduce noise. For the reconstruction of the deflection shapes, we synchronously display the sequential measurements in MATLAB.

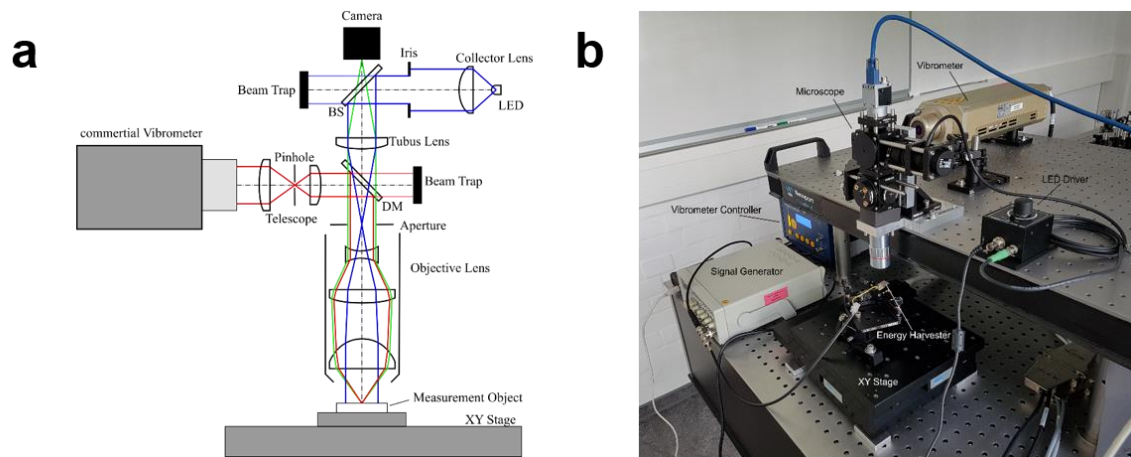


Figure 6.6: Laser Doppler vibrometer setup for modal analysis of piezoelectric beams. (a) Schematic of the of scanning confocal vibrometer microscope. (b) Photo of the whole measurement setup.

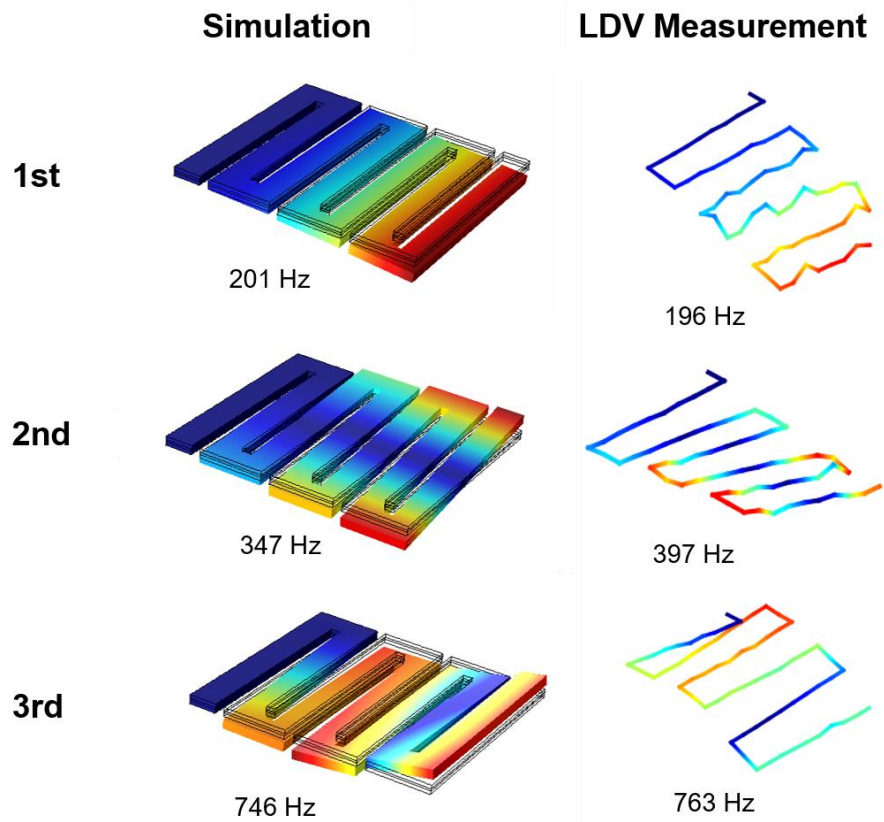


Figure 6.7: Modal analyses of the serpentine beam using simulation and LDV measurements.

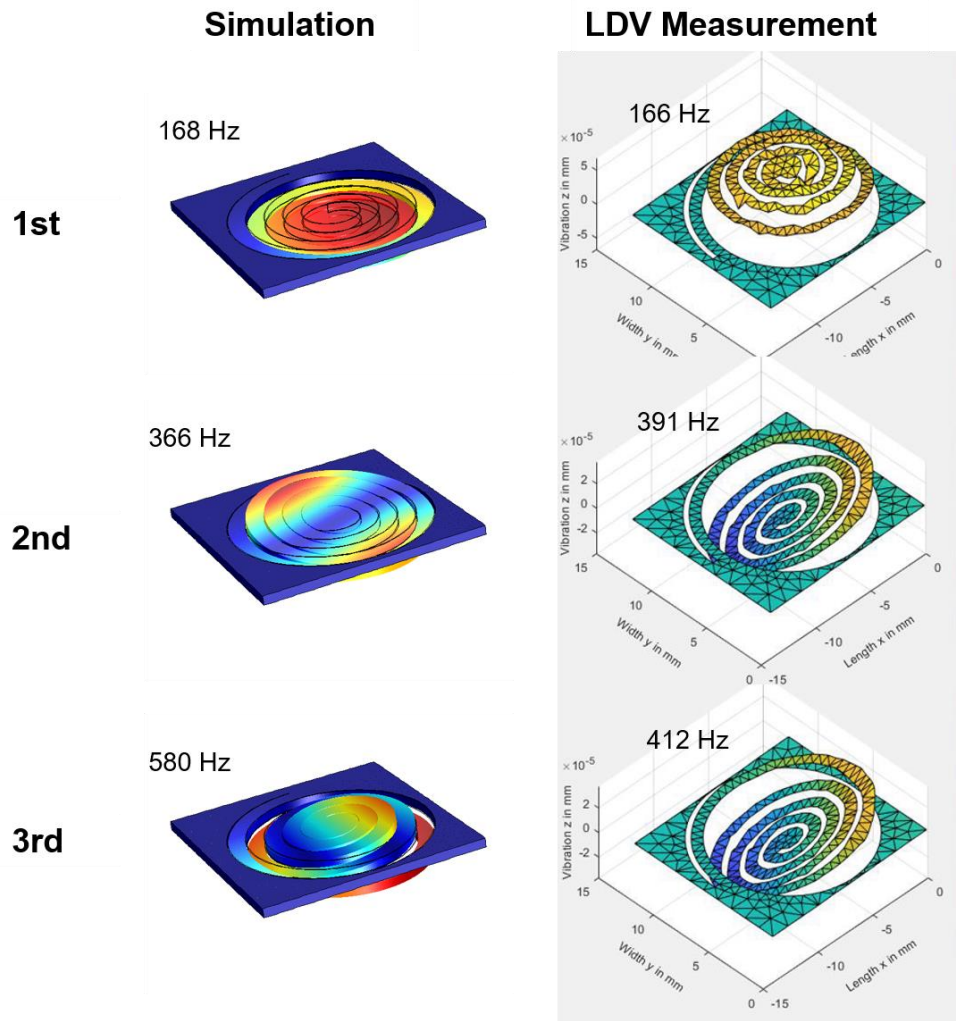


Figure 6.8: Modal analyses of the spiral beam using simulation and LDV measurements.

The summarized modal analyses using COMSOL simulations and LDV measurements are shown in Figure 6.7 and Figure 6.8. Among five different shapes, the spiral beam which has 5 turns and 1.5 mm of initial radius was used for the LDV measurement. Figure 6.7 shows the mode shapes of the serpentine beams up to the third modal order from simulation and LDV measurements. The similar mode analyses of the spiral beam are also shown in Figure 6.8. From both cases of serpentine beam and spiral beam, the mode shapes of first, second, and third modal order are the same as expected from the FEM simulation.

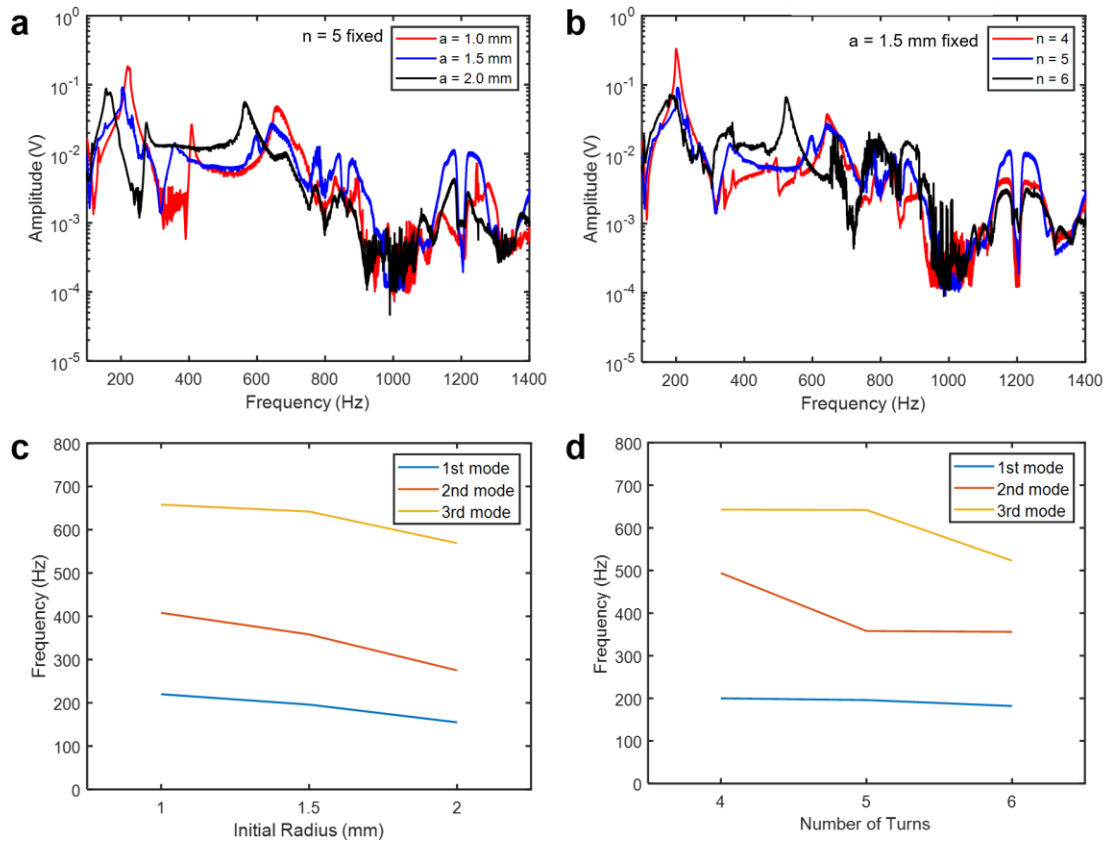


Figure 6.9: Frequency analyses of spiral beams by changing the initial radius (a) and number of turns (b). The resonance frequencies at 1st - 3rd modal orders are summarized in (c) and (d).

Frequency analysis is carried out by measuring generated voltage from the beams with a frequency modulated vibration. The subject beam was connected to a vibration generator (3B Scientific's U56001) and the function generator (Agilent 33120A) that provide AC signals to vibration generator controlled by LabVIEW. The LabVIEW varied the frequency of the function generator and collected generated voltage data simultaneously.

The frequency responses from spiral beams by varying the initial radius, a , and number of turns, n , are shown in Figure 6.13a, b. The summarized results of resonance frequencies are also shown in Figure 6.13c, d. The resonance frequencies of the first three modal orders are 2-29 % away from the simulation results. As expected, the resonance frequencies are inversely proportional to the initial radius and number of turns. As the frequency gap

between each mode got smaller, the amplitude obtained over the first three modes increased. When we calculated the sum of amplitudes at 100-600 Hz, the sum increased by 39.5% and 52.5% respectively according to changes of a and n . This can be considered an advantage in utilizing spread vocal vibrations during reading or speaking.

The frequency response of the serpentine beam was also analyzed as shown in Figure 6.10. The fundamental resonance frequency was at 216 Hz which was 8% away from the expected resonance frequency from simulation. The amplitude decreased rapidly after the second mode since the frequencies of the higher modal order are relatively far away compared to these from the spiral beams.

To characterize the power generation from the serpentine and spiral beams, the AC output powers from the beams were measured as the load connected to the beam was swept from 1 k Ω to 100 k Ω . Among five shapes of spiral beams, the spiral beam which had 6 turns and 1.5 mm of initial radius was used for the power measurements from the load test (Figure 6.11). The 10 k Ω of load resistor allowed the maximum output power from both types of the beams.

With this load found, then, the output signals from humming and reading were measured using both beams. Figure 6.12 shows time- and frequency-domain transient output signals from the spiral beam and the serpentine beam while humming and reading. Since voltage output from the serpentine beam at the first mode resonance was larger than that from serpentine beam, humming at 200 Hz which is near the first resonances of the beams enables larger voltage output from the serpentine beam. However, larger voltage outputs from reading came out from the spiral beam because close-gathered higher modes contributed to achieve higher voltage generation in a broadband region from reading.

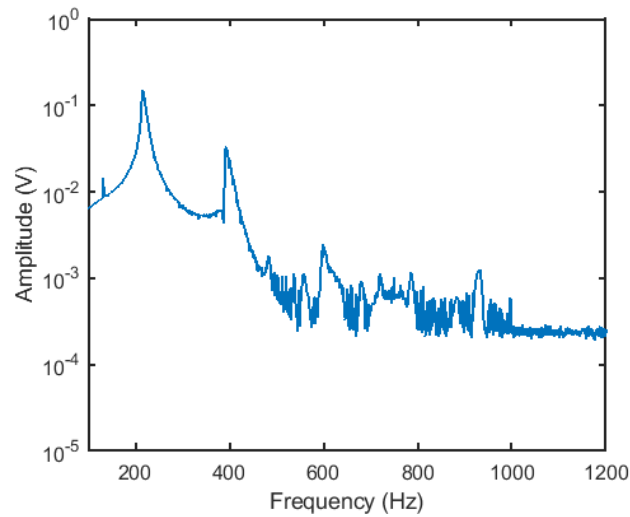


Figure 6.10: Frequency analysis of serpentine beam.

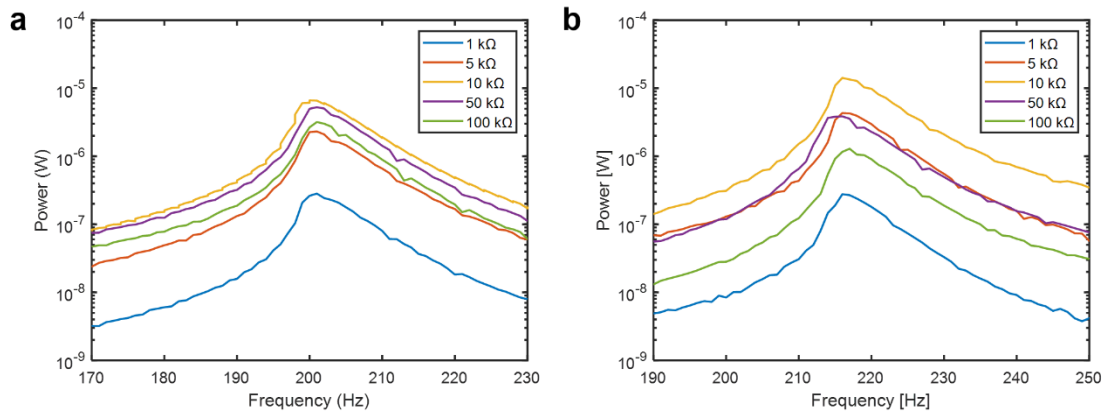


Figure 6.11: Optimum load test by measuring output power with each load from the spiral beam (a) and the serpentine beam (b).

Then, 4-stacked spiral energy harvesters with an AC/DC converter consisting of a voltage double rectifier successfully produced $0.61 \text{ V}_{\text{DC}}$ with 70-dB of reading while EH packaging with 4-stacked serpentine beams only generated $0.23 \text{ V}_{\text{DC}}$ (Figure 6.13). Based on the results so far, the spiral beams can have advantages in broadband applications to achieve low fundamental resonance frequency at a limited area.

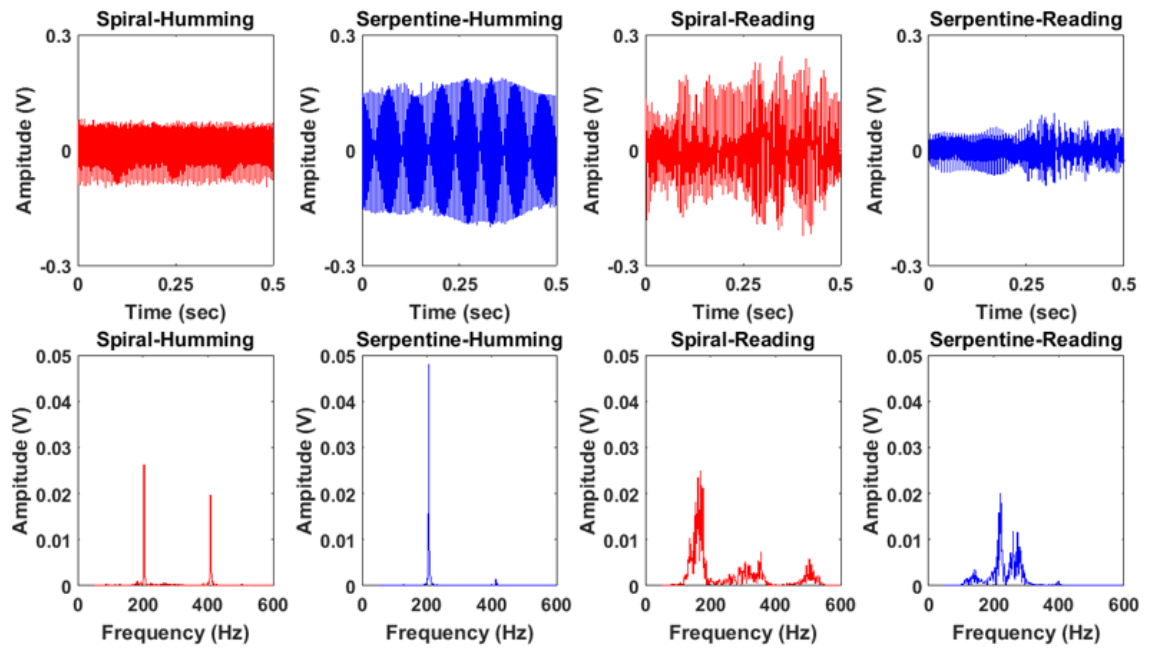


Figure 6.12: Time- and frequency-domain transient output signal from the spiral beam ($n = 6$, $a = 1.5$ mm) while humming and reading.

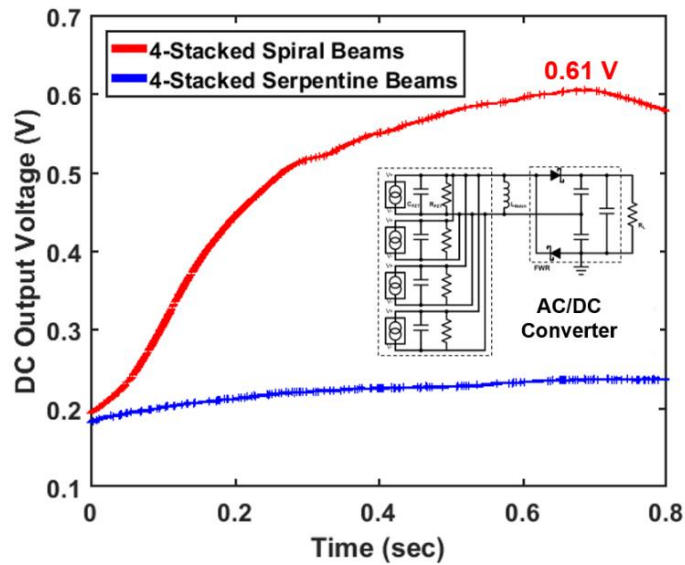


Figure 6.13: DC output voltages from the 4-stacked spiral beams and serpentine beams when the participant read a book. The voltage double rectifier was used to convert AC to DC signal.

6.3 Energy Harvesting from the Top of the Human Head

The top of the head serves up to 20% of energy compared to the 100% energy from the larynx. This area is a promising energy source for implantable devices near the brain or the parietal bone such as deep brain stimulation (Kuncel and Grill, 2004), bone-anchored hearing devices (Tjellström et al., 1995), and retinal implants (Zrenner, 2002). In case of deep brain stimulation, the battery is placed inside the chest to avoid the periodic open head surgery, but it still needs the additional surgery to replace the battery. In addition, the long electrical wiring from the battery to the electrode causes a reliability issue because it may break when people move. If the energy harvesting source can be implanted underneath the scalp, it could be a good option to enable self-powered implantable devices around the brain.

A real head model was purchased from SynDaver Labs and used to compare the vibrations distribution on the scalp and underneath the scalp (Figure 6.3a). This human torso model includes a realistic oral cavity with a hard and soft palate, tongue, uvula, epiglottis and vocal cords. The acceleration on both human participant and real head model were measured first, then acceleration on the skull was also measured to compare the location on the scalp and underneath the scalp.

The air tube was connected to the airway of the head model through the fast switching solenoid valve. The valve (Festo's MHE4-MS1H-3/2G-1/4) was powered by a DC power supply (Mastech's HY3005F-3) and controlled by a programmed microcontroller board (Arduino Uno) to allow the air flow to come out at a frequency of 100 Hz (Figure 6.3b). The frequency modulated air flow generated mechanical vibrations throughout the head by flowing through the artificial airway, vocal folds, oral cavity, and brain.

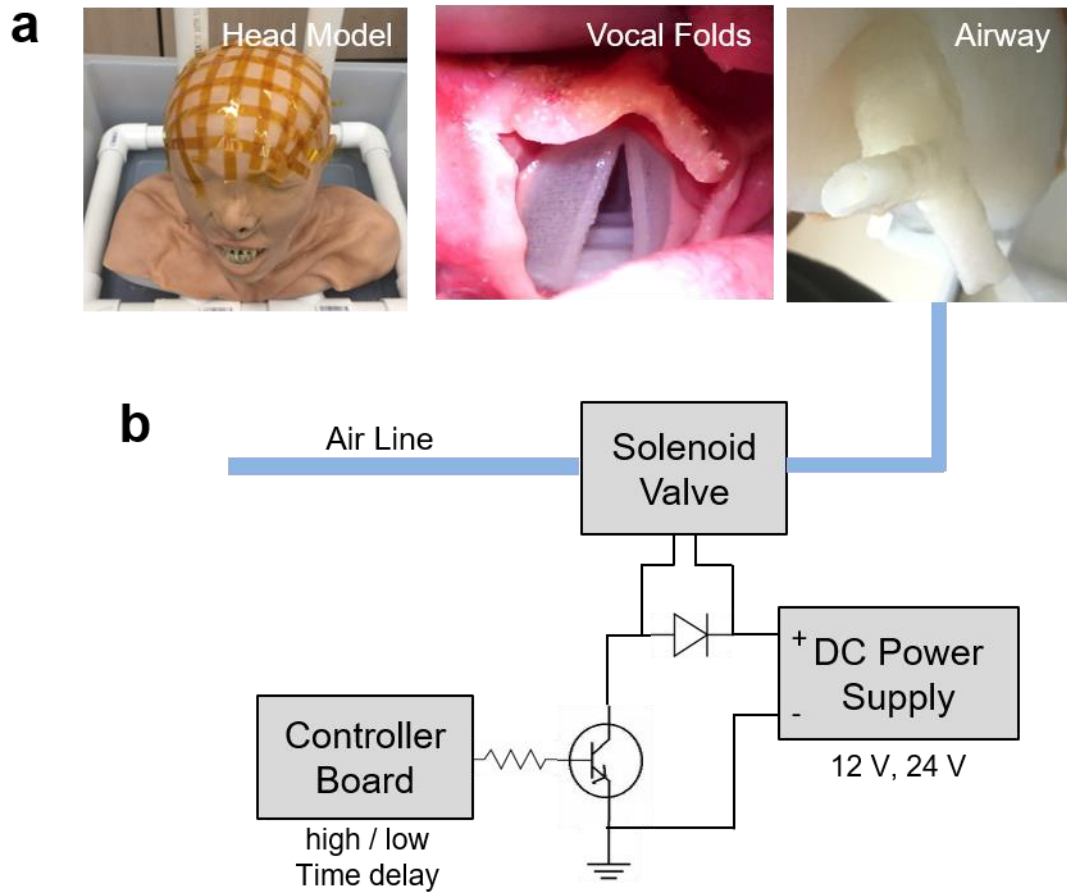


Figure 6.14: Human head model for measurement of artificial vocal vibrations. (a) The human head model includes vocal folds and airways to allow air flow throughout the head. (b) Frequency modulated air flow was produced using the fast switching solenoid valve and the controller board.

The acceleration measurement results and their hotspots color mapping using 3D MEMS accelerometer are shown in Figure 6.4. The hotspots were mapped out three times on the human head, scalp and skull of the head model. The scalp of the head model was peeled off after the measurement on the scalp. Color mapping data was normalized to the strongest point of each measurement. From all three cases, vibration distribution seems similar. The location around the center of the head has the strongest vibration. The vibration becomes weaker as the point moves away from the center of the head.

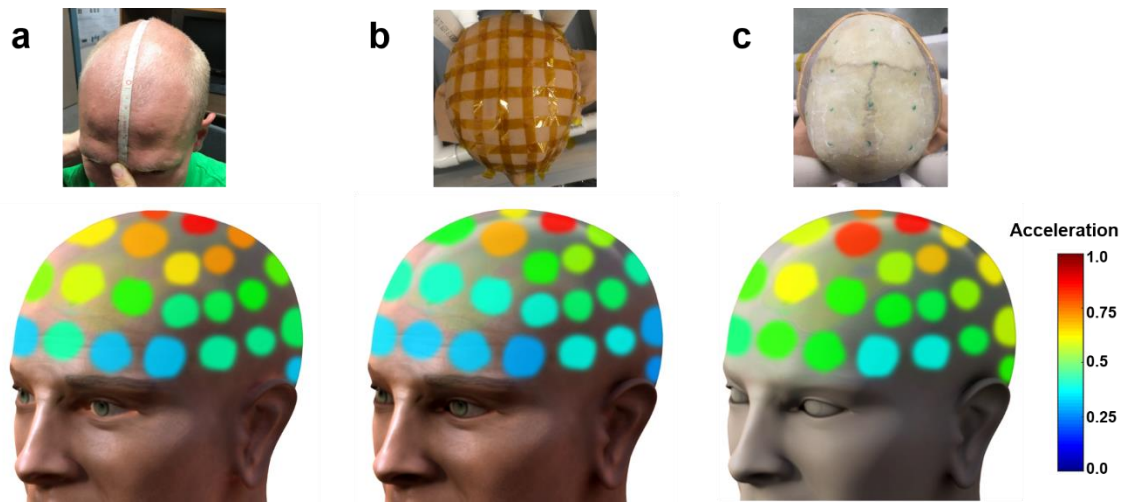


Figure 6.15: Vibration mapping from real human head (a), scalp of the head model (b), and skull of the head model (c).

At the center point, the acceleration from the skull (0.136 m/s^2) was increased by 46% than that from the scalp (0.093 m/s^2). The approximate calculation of the vibration hotspot area at the top of the head is shown in Table 6.1. The hotspot area on the skull which has more energy than 75% or 50% of vibration energy from the center point was more than twice the area on the scalp of the head model.

Table 6.3: Area of vibration hotspot ($> 75\%$, $> 50\%$ of the center point) at the location of the top of the head.

Location	Scalp		Skull
	Human Head	Head Model	Head Model
$> 75\%$	27 cm^2	20 cm^2	36 cm^2
$> 50\%$	68 cm^2	57 cm^2	117 cm^2

From these results from a realistic human model, it was shown that the top of the head location provides large a vibration hotspot area. In addition, existence of stronger and larger vibration hotspots underneath the scalp could provide a promising energy harvesting source for implantable devices around the brain such as deep brain stimulation.

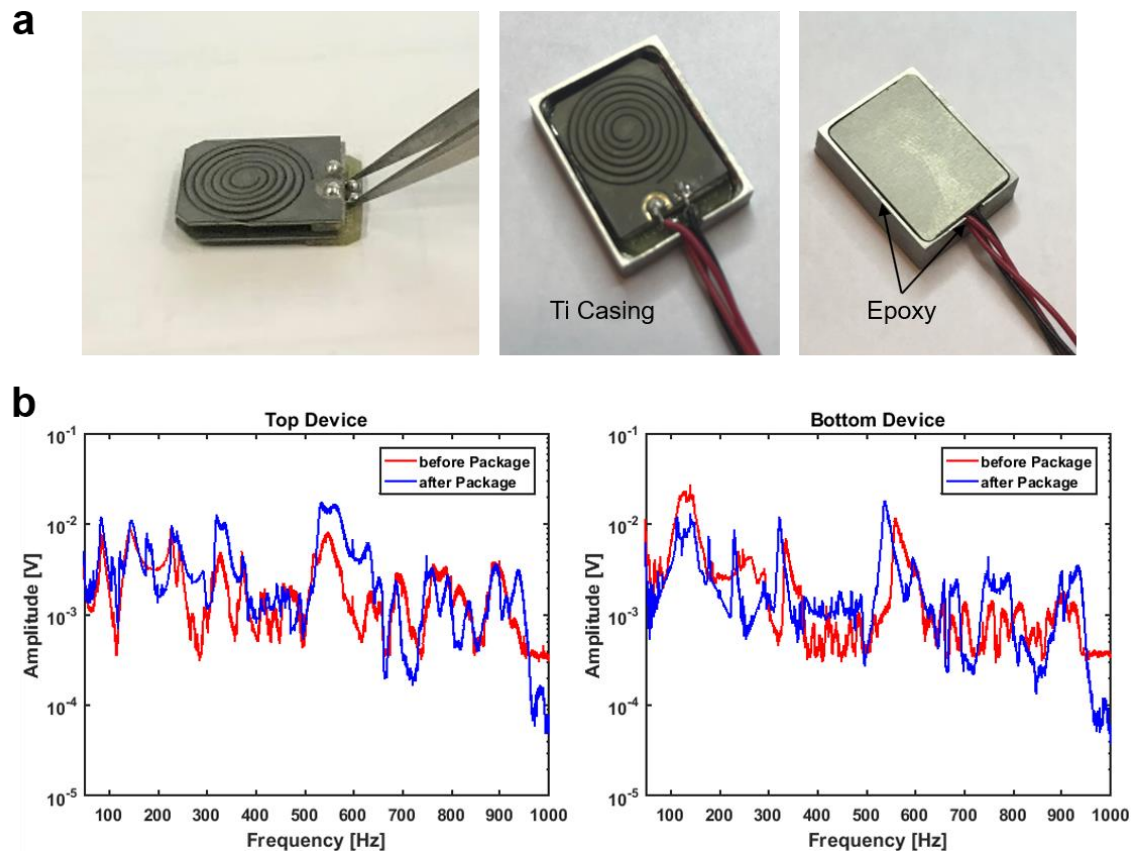


Figure 6.16: Titanium (Ti) casing to firmly stack two spiral beams. (a) Photo images of the stacked spiral beams and Ti casing. (b) Frequency analyses of the top and bottom device before and after packaging.

To generate power at the top of the head using vocal vibrations, we made metal packaging for two spiral beams to be stacked inside. The two-stacked spiral beams and the metal casing to package the beams are shown in Figure 6.16a. Titanium (Ti) was chosen as metal casing material, since Ti is a biocompatible material and it is already used in neurosurgery. Ti sheet (thickness: 4.75 mm) was milled using milling machine (Bantam Tools' Othermill) to make the Ti casing. The stacked beams were firmly attached to the bottom of the casing,

and the Al cover and the hole through which the electrical lines pass were sealed with epoxy. The frequency responses from the top and bottom devices were analyzed twice before and after the Ti casing (Figure 6.16b). The change in the first and higher modes is not significant. The reliability of this package was confirmed by measuring the weight for 30 days. The package was kept in water for 30 days and only dried when weighed. The increase of the weight was only 1.1 mg for 30 days of test period (initial weight: 2.6410 g).

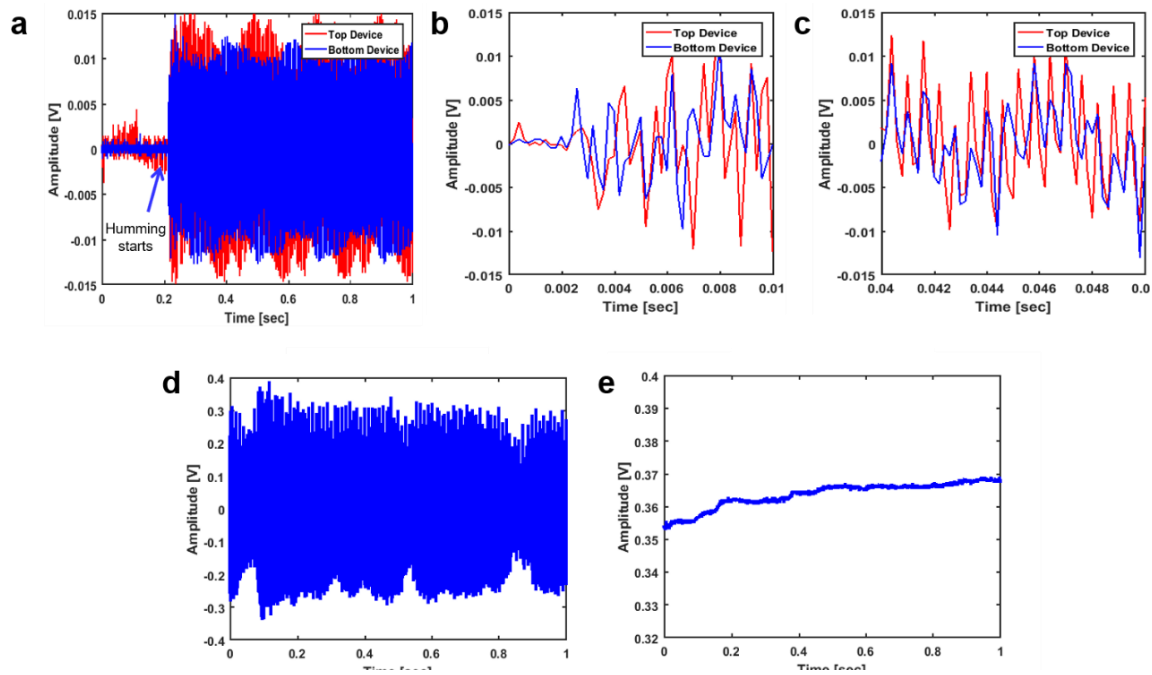


Figure 6.17: Power generation at the top of the head using the two-stacked spiral beams. (a) Synchronization of two-stacked energy harvesters. Transient signals when humming starts (b) and 50 msec after humming starts (c). (d) AC transient output signal from 2-stacked energy harvesting package using spiral beams. (e) AC transient output signal after LC resonant full wave rectifier.

Synchronization between the two devices was observed in Figure 6.17a-c. When humming began, the time phase difference was large (Figure 6.17b), but the difference got smaller and the two beams vibrated in phase within 50 msec (Figure 6.17c). Then, the output power of this package was evaluated at the top of the head with 75-dB of humming. As shown in

Figure 6.17e, the DC voltage output was $0.37 V_{DC}$ using AC/DC converter (LC resonant full wave rectifier) and $10 \mu F$ as a load. This amount of DC voltage is enough for the cold start of boost charger.

6.4 Conclusion

For real-time energy harvesting to utilize vocal vibrations not only from humming but also from reading and speaking, the broadband applicable energy harvesting using a spiral structure was designed and characterized. By changing the dimensional parameters of the spiral structure, the frequency gap between resonance modes was able to be closer. This closer resonance frequency gap led to higher voltage amplitudes generated over broadband. Using 4-stacked spiral beams and an AC/DC converter, $0.61 V_{DC}$ was successfully obtained.

In addition, the hotspot location at the top of the head was tested for practical applications near the brain such as deep brain stimulation. Using a realistic head model, the available areas for the energy harvester to generate power were expected ($57\text{-}68 \text{ cm}^2$ on scalp; $\sim 117 \text{ cm}^2$ on skull). The conceptual flexible energy harvesting package as the example shown in Figure 6.18 can be implanted underneath the scalp (above the skull) to harvest energy for the brain implants in a close distance.

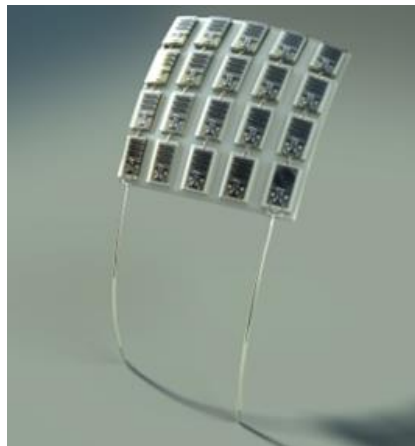


Figure 6.18: Concept image of energy harvesting package to be implanted on the skull of human head.

References

- Lee, S.; Bae, S. -H.; Lin, L.; Yang, Y.; Park, C.; Kim, S. W.; Cha, S. N.; Kim, K.; Park, Y. J.; Wang, Z. L. Super-flexible nanogenerator for energy harvesting from gentle wind and as an active deformation sensor. *Adv. Func. Mat.* 2012, 23, 19, 2445-2449.
- Wang, Z. L. Triboelectric nanogenerators as new energy technology and self-powered sensors – Principles, problems and perspectives. *Faraday Discuss.* 2014, 176, 447-458.
- Li, H.; Tian, C.; Deng, Z. D. Energy harvesting from low frequency applications using piezoelectric materials. *Appl. Phys. Rev.* 2014, 041301.
- Kulah, H.; Najafi, K. An electromagnetic micro power generator for low-frequency environmental vibrations. 17th IEEE International Conference on Micro Electro Mechanical Systems. Maastricht MEMS 2004 Technical Digest, 8032457 (2004).
- Liu, H.; Lee, C.; Kobayashi, T.; Tay, C. J.; Quan, C. A new S-shaped MEMS PZT cantilever for energy harvesting from low frequency vibrations below 30 Hz. *Microsyst. Technol.* 2012, 18, 497.
- Kim, H. W.; Batra, A.; Priya, S.; Uchino, K.; Markley, D.; Newnham, R. E.; Hofmann, H. F. Energy harvesting using a piezoelectric "cymbal" transducer in dynamic environment, *Jpn. J. Appl. Phys.* 2004, 43, 1, Number 9A.
- Hu, Y.; Yang, J.; Jing, Q.; Niu, S.; Wu, W.; Wang, Z. L. Triboelectric nanogenerator built on suspended 3D spiral structure as vibration and positioning sensor and wave energy harvester. *ACS Nano* 2013, 7(11), 10424-10432.
- Tao, K.; Liu, S.; Lye, S. W.; Miao, J.; Hu, X. A three-dimensional electret-based micro power generator for low-level ambient vibrational energy harvesting. *J. Micromech. Microeng.* 2014, 24, 6.
- Perry, M. D.; Stuart, B. C.; Banks, P. S.; Feit, M. D.; Yanovsky, V.; Rubenchik, A. M. Ultrashort-pulse laser machining of dielectric materials, *J. Appl. Phys.* 1999, 85, 6803.
- Emmelmanna, C.; Petersen, M.; Goeke, A.; Canisius, M., Analysis of laser ablation of CFRP by ultra-short laser pulses with short wavelength. *Phys. Procedia.* 2011, 12, Part A, 565-571.
- Kowarsch, R.; Janzen, J.; Rembe, C.; Cho, H.; Choo H. Scanning confocal vibrometer microscope for vibration analysis of energy-harvesting MEMS in wearables. *tm-Tech. Mess.* 2017, 84 (s1).
- Kuncel, A. M.; Grill, W. M. Selection of stimulus parameters for deep brain stimulation. *Clin. Neurophysiol.* 2004, Volume 115, Issue 11, Pages 2431-2441.
- Tjellström, A.; Håkansson, B. The bone-anchored hearing aid. Design principles, indications, and long-term clinical results. *Otolaryng. Clin. N. Am.* 1995, 28(1), 53-72.
- Zrenner, E., Will Retinal Implants Restore Vision? *Science* 2002, 295, 5557, 1022-1025.